



저작자표시-비영리-변경금지 2.0 대한민국

이용자는 아래의 조건을 따르는 경우에 한하여 자유롭게

- 이 저작물을 복제, 배포, 전송, 전시, 공연 및 방송할 수 있습니다.

다음과 같은 조건을 따라야 합니다:



저작자표시. 귀하는 원저작자를 표시하여야 합니다.



비영리. 귀하는 이 저작물을 영리 목적으로 이용할 수 없습니다.



변경금지. 귀하는 이 저작물을 개작, 변형 또는 가공할 수 없습니다.

- 귀하는, 이 저작물의 재이용이나 배포의 경우, 이 저작물에 적용된 이용허락조건을 명확하게 나타내어야 합니다.
- 저작권자로부터 별도의 허가를 받으면 이러한 조건들은 적용되지 않습니다.

저작권법에 따른 이용자의 권리는 위의 내용에 의하여 영향을 받지 않습니다.

이것은 [이용허락규약\(Legal Code\)](#)을 이해하기 쉽게 요약한 것입니다.

[Disclaimer](#)

Ph.D. DISSERTATION

**Structures and properties of various phases of
zinc tin oxide by *ab-initio* calculations**

by

Joohwi Lee

February 2013

**Department of Materials Science and Engineering
College of Engineering
Seoul National University**

Structures and properties of various phases of zinc tin oxide by *ab-initio* calculations

Advisor : Prof. Cheol Seong Hwang

**By
Joohwi Lee**

**A thesis submitted to the Graduate Faculty of Seoul National
University in partial fulfillment of the requirements for the
Degree of Doctor of Philosophy
Department of Materials Science and Engineering**

February 2013

**Approved
by**

Chairman of Advisory Committee : Hyeong Joon Kim

Vice-chairman of Advisory Committee : Cheol Seong Hwang

Advisory Committee : Seungwu Han

Advisory Committee : Jung-Hae Choi

Advisory Committee : Jae Kyeong Jeong

Abstract

Zinc tin oxide (ZTO) is one of the transparent conducting oxides which can be used as a channel layer of thin film transistor (TFT), solar cell, gas sensor due to the high transmittivity, high mobility, excellent chemical selectivity. For these applications, amorphous structures or nanoclusters are mainly used. However, the fundamental properties even on crystalline ZTO phases have not been thoroughly investigated. In this dissertation, the understanding on the bulk properties of crystalline phases, point defects in crystal phase, and amorphous phase of ZTO was investigated by using *ab-initio* calculations, which are powerful simulation tools to figure out the fundamental properties from the interactions between atoms and electrons.

Various crystalline phases of ZTO have been reported to form depending on the synthesis methods and conditions. Zn_2SnO_4 and $ZnSnO_3$ are the representative compositions. For Zn_2SnO_4 , it was reported that the inverse spinel is stable and that the cation disordering at the octahedral sites by zinc and tin changes the symmetry of the structure in the unit cell scale. For $ZnSnO_3$, lithium niobate and ilmenite phases exist which are corundum-base structures with the different occupancy at the octahedral sites by zinc, tin and vacancy.

Thermodynamic stabilities of various zinc tin oxides were investigated based on the Gibbs energy obtained from density functional

theory calculations with the phonon vibrational and configurational terms. The pressure-temperature (p-T) phase diagram was determined; at zero external pressure, the coexistence of ZnO and SnO₂ was the most stable at low temperature, and Zn₂SnO₄ became stable over approximately 1000~1300 K. Pressurization mainly affected the Zn-O bonds and changed the thermodynamic stability via the following sequences: from the coexistence of ZnO and SnO₂ to the coexistence of Zn₂SnO₄ and SnO₂, then to ZnSnO₃ in the lithium niobate structure. ZnSnO₃ in the ilmenite structure was found to be unstable due to the relatively high energy and the negative phonon frequency. The effects of the space group of the unit cell scale for Zn₂SnO₄ and the exchange-correlation functionals were also investigated. The different space groups of Zn₂SnO₄ in the unit cell scale affected the thermodynamic conditions of Zn₂SnO₄. The calculated results showed good agreement with the experimental phase stability and were able to explain the experimental observation of the mixed state of Zn₂SnO₄, ZnO and SnO₂ in the temperature and pressure midranges.

The point defects of oxygen vacancy and hydrogen interstitial in the inverse spinel Zn₂SnO₄ phase were investigated, where Zn₂SnO₄ phase is the most stable phase in ternary system. The calculations were performed using hybrid density functional proposed by Heyd-Scuseria-Ernzerhof (HSE) in order to adjust the bandgap to the experimental value. The defect formation energies showed the neutral oxygen vacancy is stable when the Fermi level

is located at the n-type region. The transition level $\epsilon(2+/0)$ was about 1 eV below the conduction band minimum. The oxygen vacancy can be ionized by the photon energy of 2 eV and perform as the photocurrent source. On the other hand, the hydrogen interstitial was found to exist as a singly charged state and can be act as an electron source.

The amorphous phases of Zn_2SnO_4 and $ZnSnO_3$ were obtained by melt-quenching method based on the *ab-initio* molecular dynamics. The radial distribution function results showed the coordination number of Zn-O bonds in amorphous phase decreased close to 4 as that of binary oxide, ZnO. The bond length of Zn-O becomes similar as that of ZnO. Meanwhile, the coordination number and bond length of Sn-O bonds are all similar with each other in both binary oxide and ternary oxides.

Keywords : *ab-initio*, zinc tin Oxide (ZTO), transparent conducting oxide (TCO), p-T phase diagram, point defect, amorphous

Student ID : 2007-20739

Joohwi Lee

Table of Contents

Abstract	i
Table of Contents	iv
List of Figures	viii
List of Tables	xiii
1. Introduction	1
1.1. Transparent conducting oxides (TCOs).....	1
1.2. Issues.....	7
1.3 <i>Ab-initio</i> (First principles) calculations.....	11
1.3.1. Approximations for reducing the variables.....	11
1.3.2. Hartree-Fock (HF) theory.....	12
1.3.3. Density functional theory (DFT).....	13
1.3.4. Underestimation of bandgap and the error of structural parameters.....	14
1.3.5. On-site correction of DFT+U.....	14
1.3.6. Hybrid density functional theory.....	15
1.4. Object of this study.....	18
2. Fundamental properties of zinc tin oxides	20
2.1. Review of zinc tin oxides.....	20

2.1.1. Various synthesis methods of zinc tin oxides.....	20
2.1.2. Structural details.....	22
2.2. Computational methods.....	26
2.3. Optimized structures.....	28
2.4. Electronic structures.....	32
2.5. Density of states (DOS).....	36
3. Thermodynamic stability of various phases of zinc tin oxides.....	43
3.1. Overview.....	43
3.2. Thermodynamic variables.....	44
3.3. Computational methods.....	50
3.4. Results and discussions.....	54
3.4.1. Thermodynamic stability by enthalpy.....	54
3.4.2. Phonon density of states.....	59
3.4.3. Thermodynamic stability by Gibbs free energy.....	61
3.4.4. P-T phase diagram.....	63
3.4.5. DFT+U method.....	69
3.4.6. Cation disordering.....	70
3.4.7. Zn-O bond changes by pressurization.....	73
3.5. Summary.....	75

4. Point defects in inverse spinel Zn₂SnO₄	77
4.1. Overview.....	77
4.2. Formation energy calculations of point defects.....	79
4.2.1. The definition of formation energy.....	79
4.2.2. The correction of underestimated bandgaps.....	80
4.2.3. The correction of image charge interactions.....	81
4.3. Computational Methods.....	82
4.4. Formation of oxygen vacancy.....	84
4.4.1. Image correction result using GGA+U scheme.....	84
4.4.2. Formation energy of oxygen vacancy.....	87
4.4.3. Electronic structures.....	89
4.4.4. Optical ionization energy.....	93
4.5. Formation of hydrogen interstitials.....	96
4.5.1. Various sites hydrogen incorporated.....	96
4.5.2. Formation energy of hydrogen interstitials.....	98
4.5.3. Electronic structures.....	100
4.6. Summary.....	102
5. Local atomic structure of amorphous phases of zinc tin oxides	104
5.1. Overview.....	104
5.2. Theoretical background.....	105

5.2.1. Molecular dynamics (MD).....	105
5.2.2. Melt-quenching method.....	106
5.2.3. Radial distribution function (RDF).....	107
5.3. Computational Methods.....	109
5.4. Results and discussions.....	111
5.4.1. Total energy.....	111
5.4.2. RDF results of amorphous phases.....	115
5.4.3. Coordination number (CN).....	119
5.4.4. DOS analyses.....	122
5.5. Summary.....	126
6. Conclusions.....	127
Appendix A. X-ray diffraction (XRD) simulations.....	131
References.....	133
Curriculum Vitae.....	141
List of publications.....	143
Abstract (in Korean).....	151
Acknowledgement.....	153

List of Figures

- Figure 1.1** Composition space for conventional TCO materials.[1]
- Figure 1.2** A photograph of flexible and transparent TFT. [5]
- Figure 1.3** Schematic orbital drawings of TCOs for conduction paths. Large spheres and small pinwheel denote metal s-orbitals and oxygen 2p-orbitals, respectively. (a) Crystalline (b) Amorphous. [5]
- Figure 1.4** Practical TCOs for thin-film. [3]
- Figure 1.5** Negative bias illumination stress stability (NBIS) of zinc tin oxide TFT. [38]
- Figure 1.6** The bandgaps of various materials are compared between experiment and theory. (a) From ref. [60]. (b) From ref. [61].
- Figure 2.1** Subsolidus ternary phase diagrams of (a) ZnO-GaO_{1.5}-SnO₂ at 1250 °C [71] (b) ZnO-InO_{1.5}-SnO₂ at 1275 °C. [72] Note that Zn₂SnO₄ forms as one phase.
- Figure 2.2** Unitcells of inverse spinel *ZTO214*. u , v , and w are the lattice vectors of the conventional unitcell. Dashed vectors of a_1 , a_2 , and a_3 indicate the unit vectors of the primitive cell for (a) *tetra-ZTO214* (P4₁22), (b) *ortho-ZTO214* (Imma) and (c) *mono-ZTO214* (P1).
- Figure 2.3** Hexagonal unitcells of *ZTO113*. u , v , and w are the lattice vectors of the conventional unitcell. Dashed vectors of a_1 , a_2 , and a_3 indicate the unit vectors of the primitive cell for (a) *LN-ZTO113* (R3c), (b) *IL-ZTO113* (R-3). (c) The relations between the lattice vector of hexagonal unitcells and the primitive cells on the basal plane of hexagonal unitcells.

Figure 2.4 Electronic structures of *ZTO214*. (a) *tetra-ZTO214* (P4₁22). (b) *ortho-ZTO214* (Imma). (c) *mono-ZTO214* (P1).

Figure 2.5 Electronic structures of *ZTO113*. (a) *LN-ZTO11.3* (b) *IL-ZTO113*.

Figure 2.6 PDOS of *tetra-ZTO214*. (a) From O at site O-I. (b) From O at site O-II. (c) From Sn. (d) From Zn at tetrahedral site. (e) From Zn at octahedral site.

Figure 2.7 PDOS of *ortho-ZTO214*. (a) From O at site O-I. (b) From O at site O-II. (c) From Sn. (d) From Zn at tetrahedral site. (e) From Zn at octahedral site.

Figure 2.8 PDOS of *mono-ZTO214*. The intensities of PDOS peaks are divided into the number of each atom. (a) From O. (b) From Sn. (c) From Zn.

Figure 2.9 PDOS of *LN-ZTO113*. (a) From O. (b) From Sn. (c) From Zn.

Figure 2.10 PDOS of *IL-ZTO113*. (a) From O. (b) From Sn. (c) From Zn.

Figure 3.1 Schematic diagram of the E-V curve and the phase transition by pressurization. E, p and H mean the total energy of electronic structure obtained from *ab-initio* calculation, pressure, and enthalpy, respectively. The subscripts A and B indicate two different phases. The superscripts 0 and Tr denote the optimized structure and the transformation by pressure.

Figure 3.2 Schematics illustrations to obtain the Gibbs energy as a function of the cell volume. The energy can be extracted using (a) E+pV to consider the pressure effect (T=0) and (b) E+F_{vib} to consider the temperature effect (p=0).

Figure 3.3 (a) Schematic illustration to draw the E-V curve. The volume at the step 1 is maintained at the step 2. (b) The summation of energy

and volume were performed under the same hydrostatic pressure. The Positive and negative values means the hydrostatic compressive and tensile stress, respectively.

Figure 3.4 E-V curve obtained by the (a) LDA and (b) GGA calculations.

The negative common tangent means the transition pressure. The arrow in (b) means that the curve becomes meaningless for *IL-ZTO113* under the external pressure over -10 GPa.

Figure 3.5 Phonon DOSs of (a) ZnO (b) SnO₂ (c) *tetra-ZTO214* (d) *ortho-ZTO214* (e) *LN-ZTO113* and (f) *IL-ZTO113* at -14, 0 and 14 GPa.

The arrow indicates the negative phonon frequency in *IL-ZTO113* at -14 GPa.

Figure 3.6 Gibbs free energy of various phases as a function of temperature at the *ZTO113* composition by (a) LDA at p = 0. (b) GGA at p = 0. (c) LDA at p = 4 GPa. (d) LDA at p = 8 GPa.

Figure 3.7 P-T phase diagram at the (a) *ZTO113* composition using LDA (b) *ZTO113* composition using GGA (c) *ZTO113* composition using LDA by considering only *ortho-ZTO214* instead of *tetra-ZTO214* and (d) *ZTO214* composition using LDA functionals.

Figure 3.8 Comparison of ordered inverse spinel *ZTO214* and disordered inverse spinel *ZTO214*. (a) Energy of electronic structure at 0K. (b) Helmholtz free energy F(V,T) at p=0.

Figure 3.9 P-T phase diagrams for the (a) *ZTO113* composition. (b) *ZTO214* composition using disordered inverse spinel *ZTO214* (*DIS-ZTO214*).

Figure 4.1 Image corrections for charged vacancy. (a) V_O⁺ using GGA+U. (b) V_O²⁺ using GGA+U.

Figure 4.2 Oxygen vacancy formation energies using opt-HSE06 with LZ correction.

Figure 4.3 Electronic structures of *ZTO214* with oxygen vacancy at O-I site using opt-HSE06. (a) no vacancy. (b) V_O^0 . (c) up-spin of V_O^+ . (d) down-spin of V_O^+ . (e) V_O^{2+} .

Figure 4.4 Eigenvalues generated by oxygen vacancies between the bandgap in *ZTO214*. The states were defined at the Γ -point and averaged at 2^3 MP points using opt-HSE06, respectively. (a) From O-I site. (b) From O-II site.

Figure 4.5 Ionization energy of oxygen vacancy by visible light. From (a) O-I site. (b) O-II site.

Figure 4.6 Hydrogen interstitial formation energy using opt-HSE06.

Figure 4.7 The atomic view of incorporated hydrogen interstitial as the state of H^+ and bond with oxygen.

Figure 4.8 Electronic structure of *ZTO214* with the hydrogen interstitial. Solid line and dashed line indicate the occupied and unoccupied bands. (a) Pure *ZTO214*. (b) With H_i^0 . (c) With H_i^+ .

Figure 5.1 Space discretization for the evaluation of the radial distribution function. [108]

Figure 5.2 Melt-quenching calculation profiles in order to get the amorphous cells using AI-MD

Figure 5.3 Energy-volume diagram of the crystalline and amorphous phases. (a) For *ZTO214* composition. (b) For *ZTO113* composition.

Figure 5.4 Supercells for *ZTO214* composition. (a) Crystalline *ZTO214*. (b) Amorphous *ZTO214*.

Figure 5.5 RDF results of oxygen related bonds for amorphous zinc tin oxides. (a) *a-ZTO214* (b) *a-ZTO113*. RDF of around the first peak of (c) *a-ZTO214*. (d) *a-ZTO113*. Vertical lines indicate the bond lengths of crystalline phases.

Figure 5.6 RDF results of distances between cations for amorphous zinc tin oxides. (a) *a-ZTO214*. (b) *a-ZTO113*.

Figure 5.7 PDOSs of *ZTO214* phases in whole range of energy (left) and around bandgap (right). From (a) Crystalline *ZTO214* (P4₁22). (b) Amorphous *ZTO214*. (c) Amorphous *ZTO214* with O-O bond.

Figure 5.8 PDOSs of various *ZTO113* phases in whole range of energy (left) and around bandgap (right). From (a) Crystalline *ZTO113* (R3c). (b) Amorphous *ZTO113*.

Figure 5.9 Inverse participation ratio (IPR) of crystalline and amorphous ZTOs. From (a) *c-ZTO214*. (b) *c-ZTO113*. (c) *a-ZTO214*. (d) *a-ZTO113*.

Figure A.1. X-ray diffraction (XRD) simulation of various zinc tin oxides with the optimized structure using opt-HSE06. (a) ZnO. (b) SnO₂. (c) *ZTO113* (LN). (d) *ZTO113* (IL). (e) *ZTO214* (P4₁22).

List of tables

- Table 1.1** TCO materials for various applications. [6]
- Table 2.1** Calculation conditions for the various phases of zinc tin oxide.
- Table 2.2** Unitcell volumes of zinc tin oxides.
- Table 2.3** Bulk moduli of zinc tin oxides.
- Table 2.4** The bandgap of *ZTO214* and *ZTO113* from various xc-functionals
- Table 3.1** Transition pressure and temperature at the *ZTO113 composition* by Gibbs energy or enthalpy.
- Table 3.2** Bond length and coordination number of cations in oxide phases.
- Table 4.1** Static dielectric constants from various xc-correlations.
- Table 4.2** Neutral vacancy formation energy of *ZTO214* according to various xc-functionals.
- Table 4.3** The optimized volume of tetrahedron including the oxygen vacancy surrounded by cations.
- Table 4.4** The initial position of incorporated hydrogen interstitial and formation energy calculated by GGA+U scheme.
- Table 5.1** The coordination numbers (CN) from the ionic bonds between cations and oxygens for *ZTO214 composition*.
- Table 5.2** The coordination numbers (CN) from the ionic bonds between cations and oxygens for *ZTO113 composition*.

Chapter 1. Introduction

1.1. Transparent conducting oxides (TCOs)

Transparent conducting oxides (TCOs) are used for the applications for the electronic devices such as displays, solar cells, photocatalysts, gas sensors due to good transparency and low resistivity, high chemical selectivity and unique physical properties. [1-8] Additional researches of the properties of work function, morphology, cheaper cost, lower cost and elemental abundance/ green materials have been investigated. The needs of usage of these materials also have been emerged over last 5 years so the researches of TCOs are also stimulated drastically to lead new materials and processes.

TCOs are transparent due to large bandgap over 3.1 eV which is the boundary of visible lights and ultraviolet rays. In addition, they have the n-type conductivity with the carrier (electrons) concentrations over $10^{16} \sim 10^{20}$ /cm³. According to the resistivity, conductivity and carrier concentration, TCOs are classified to conductor and semiconductor. In₂O₃ and ZnO are typical conductor and semiconductor, respectively. However, the boundary of conductor and semiconductor is not obvious. [2-4]

In fundamental, these oxide semiconductors form ionic bonds. After ionic bonds formed, cations donate the valence electrons to oxygens. Cations

have only fully occupied d-orbitals and oxygens which have fully occupied p-orbitals with satisfying the Octet's rule. In periodic table, Zn, Ga, In, Sn and Cd satisfy this condition. So they have the good and similar properties each other. For research and development, many investigations have been tried to improve the material properties by compose the binary oxides such as ZnO, Ga₂O₃, In₂O₃, SnO₂ and CdO. [1] Figure 1.1 shows the composition space for conventional TCO materials.

Hosono *et al.*, fabricated the amorphous film of InGaZnO at the room temperature. [5] This film shows good electronic properties with good transparency and hall mobility of 8 which is about 10 times higher than the film of amorphous Si. Figure 1.2 shows the fabricated transparent thin film transistor (TTFT). Room temperature deposition makes film deposited on the flexible polymer substrate such as polyethylene terephthalate (PET). Figure 1.3 shows the conduction path of the amorphous oxide film. The large s-orbital of metal oxides have isotropic transport to the radial direction, so the degradation of the mobility in amorphous oxide semiconductors such as zinc tin oxide deposited at low temperature is much less severe than that in silicon [5, 21-22].

Zinc tin oxide is one of good candidate of TCO due to good transparency, low resistivity and chemical selectivity and so on. [9-17,21-22] This material is mainly semiconductor. The applications are mainly for the channel layer of display devices and solar cell similarly to other transparent

semiconducting oxides. The amorphous phases are usually beneficial in avoiding the grain boundary problems so it can be applied to TFT without transparency such as 3D-stack memory devices. [18-19] In addition, the degradation of the mobility in amorphous oxide semiconductors such as zinc tin oxide deposited at low temperature is much less severe than that in silicon. On the other hand, for the applications for photocatalysts and gas sensors, this material is used due to good chemical selectivity and unique physical property. [11-15] It is used mainly as the nanostructures in order to maximize the surface area.

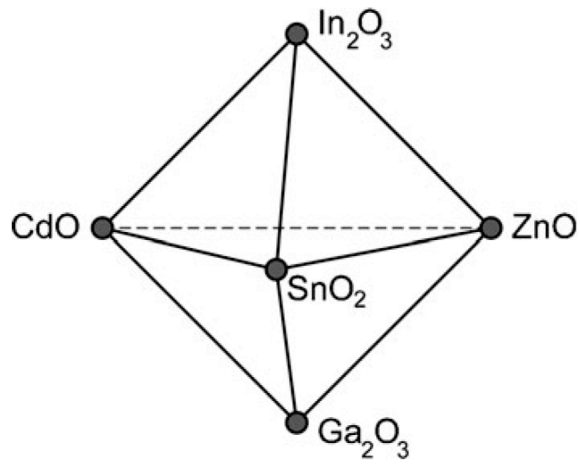


Figure 1.1 Composition space for conventional TCO materials [1]

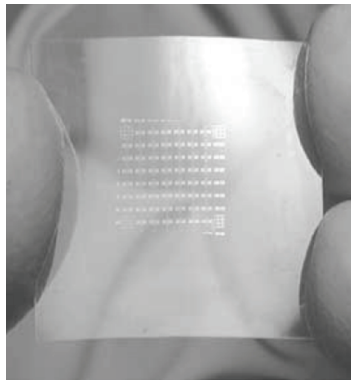


Figure 1.2 A photograph of flexible and transparent TFT. [5]

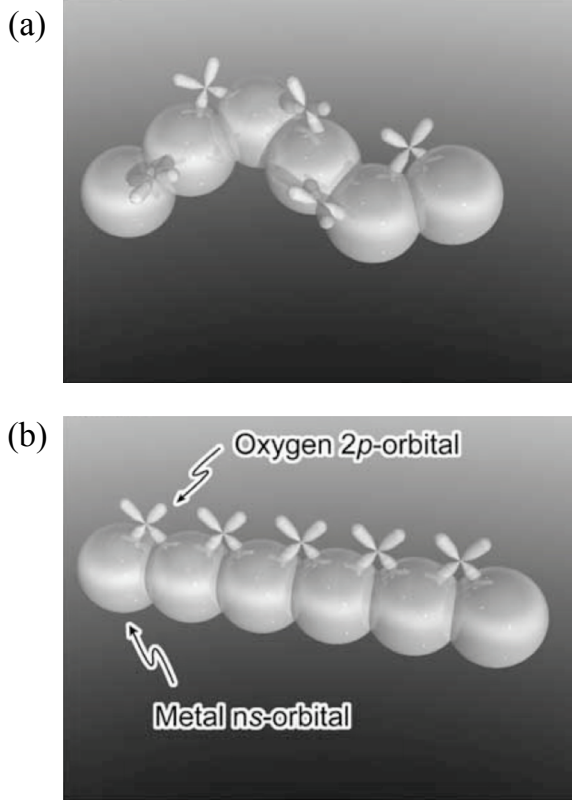


Figure 1.3 Schematic orbital drawings of TCOs for conduction paths.

Large spheres and small pinwheel denote metal s-orbitals and oxygen 2p-orbitals, respectively. (a) Crystalline (b) Amorphous.

[5]

Table 1.1 TCO materials for various applications. [6]

Property application	Material		
	Simple	Binary	Ternary
Highest transparency	ZnO:F	Cd ₂ SnO ₄	
Highest conductivity	In ₂ O ₃ :Sn		
Highest plasma frequency	In ₂ O ₃ :Sn		
Highest work function	SnO ₂ :F	ZnSnO ₃	Zn _{0.45} In _{0.88} Sn _{0.66} O ₃
Lowest work function	ZnO:F		
Best thermal stability	SnO ₂ :F	Cd ₂ SnO ₄	
Best mechanical durability	SnO ₂ :F		
Best chemical durability	SnO ₂ :F		
Easiest to etch	ZnO:F		
Best resistance to H plasmas	ZnO:F		
Lowest deposition temperature	In ₂ O ₃ :Sn ZnO:B a-InZnO		
Least toxic	ZnO:F, SnO ₂ :F		
Lowest cost	SnO ₂ :F		
TFT channel layer	ZnO	a-InZnO, a-ZnSnO	InGaO ₃ (ZnO) ₅ , a-InGaZnO
Highest mobility	CdO, In ₂ O ₃ :Ti In ₂ O ₃ :Mo		
Resistance to water	SnO ₂ :F		

1.2. Issues

In many TCOs, the most widely-investigated compound oxides have been InGaZnO. After Hosono *et al.*, reported the high mobility of IGZO on room temperature deposition in 2004, the research have been drastically increased. [5] However, the materials including indium have some issues related to cost and supply. Indium is reported the 61st abundant element in the Earth's crust, so many investigations are needed. [20] In similar period, zinc tin oxides for TFT devices were also investigated. [21,22] The devices using the channel layer of ZTO showed similarly good performances such as good transparency, high mobility compared to IGZO.

Figure 1.4 shows the widely used TCOs in transparent electronics as the thin films. The oxide including Zn and/or Sn can exist as binary oxides and ternary oxides such as Zn_2SnO_4 (*ZTO214*) and $ZnSnO_3$ (*ZTO113*). For these compositions, they are reported to have the special crystalline phases. [21-24] The researches of thin films are mainly performed as amorphous phases on the low temperature deposition method. [21,22,27,28] The properties of amorphous are difficult to define and measure, many material properties are referred to the reported crystalline at the composition. However, it is only assumed that the properties of amorphous phases follow those of the crystalline phases at the composition.

TCOs have naturally n-type conductivity. The concentrations of transport carriers become different according to formation condition such as oxygen partial pressure, temperature, post-process and so on. Because most of oxide semiconductors are oxygen deficient film, the oxygen vacancies have been thought as the n-type dopants. However, first-principles calculations recently confirmed that intrinsic defects such as oxygen vacancies do not generate any electrons in ZnO. [29-31] The materials used for electrodes such as In_2O_3 and SnO_2 have also similar issue. The behaviors of oxygen vacancy of In_2O_3 and SnO_2 and the compound oxide of IGZO have been discussed that they are deep state or shallow electron donors. [32-35,67,68]

Figure 1.5 shows the negative bias illumination stability (NBIS) of TFT devices. [38] NBIS means the shift of threshold voltage or the change of subthreshold slope value of TFT devices due to the negative bias and illumination. [38-40] Red lights does not activate NBIS problem but green lights which are over about 2.1 eV activate that in ZTO devices [41] In other devices such as InGaZnO have the similar problems. [42] Many mechanisms were proposed such as gate insulator hole trap, surface reduction, oxygen vacancy, peroxide and so on. [43-46] In those, first principles calculations proposed some defects related oxygens in InGaZnO can be the deep state. Ryu *et al.*, proposed the oxygen vacancy which can be ionized by the visible lights. [45] Nahm *et al.*, proposed peroxides can be a hole trap which occurs

NBIS problem. [37]

The melt-quenching method based on *ab-initio* molecular dynamics is an easy way to get the amorphous phase in simulations. Although the structure of amorphous is difficult to define, the ring structure is conserved with the ionic bonding of metal and oxygen. Noh *et al.*, and Kamiya *et al.*, reported the results related to the amorphous phase of InGaZnO₄ obtained by melt-quenching method. [33,46-47] They proposed that oxygen vacancies neighbored to Ga have higher vacancy formation energy. It means the Ga stabilizes the structure of amorphous phases. However, the investigations of amorphous phase of zinc tin oxides are not reported yet.

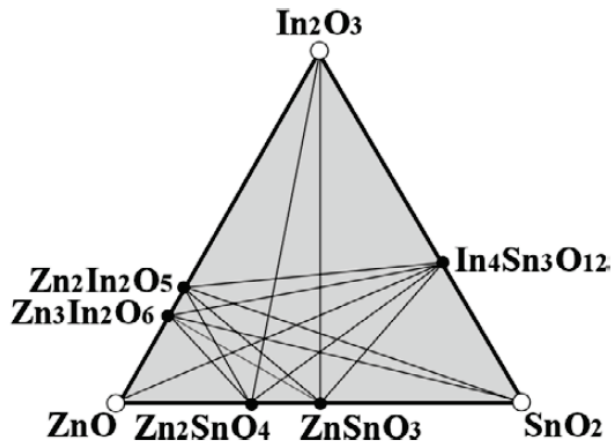


Figure 1.4 Practical TCOs for thin-film. [3]

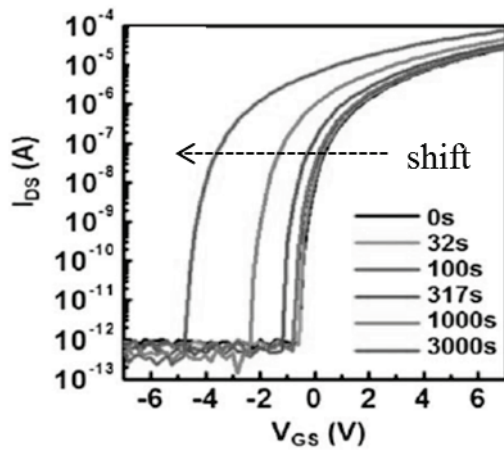


Figure 1.5 Negative bias illumination stress stability (NBIS) of zinc tin oxide TFT. [38]

1.3. *Ab-initio* (First principles) calculations

First principles calculation also known as *ab-initio* calculations is a successful tool in condensed matter for finding the ground state electronic structure of the materials. [48-49] Materials can be described as a system of the collections of atoms and electrons which have the interactions each other. As the computational integration increases, many investigations using the first principles calculations have been tried.

1.3.1. Approximations for reducing the variables

Quantum theory of materials is the Hamiltonian of the many ions and many electron system described by Schrödinger equation. However, solving the exact Schrodinger equation for many body systems are impossible, various approximations and methodologies were investigated.

Hamiltonian of Schrödinger equations are consist of the potential and kinetic energies of ions and electrons. The movement of atomic nuclei and electrons can be divided to independent variables by Born-Oppenhemier approximations. Equation 1.1 describes an effective Hamiltonian which is applied to the ionic system with an effect potential composed of the direct ion-ion interaction and electronic total energy. [50]

$$H_{ion} = \sum_{I=1}^N \left[-\frac{\hbar}{2M} \frac{\partial^2}{\partial R_I^2} \right] + \frac{1}{2} \sum_{\substack{I,J=1 \\ I \neq J}}^N V_{ion-ion}(|R_I - R_J|) + E_{tot}(R_I) \quad (1.1)$$

The many electrons systems including the kinetic energy of many electrons can be described as the external potential of ions and the interactions of the electrons with each other. The effective Hamiltonian can be described as equation 1.2.

$$H_{elec} = \sum_{i=1}^N \left[-\frac{\hbar}{2m} \frac{\partial^2}{\partial R_i^2} + \sum_{I=1}^N V_{e-i}(r_i, R_I) \right] + \frac{1}{2} \sum_i^n \sum_{j \neq i}^N \frac{e^2}{|r_i - r_j|} \quad (1.2)$$

For more approximations and methodologies to reduce the variables have been investigated and used to make an effective one electron form. Hartree-Fock (HF) theory and density functional theory will be introduced next.

1.3.2 Hartree-Fock (HF) theory

Many electron wavefunctions by an anti-symmetrized product of one electron wavefunctions is the main point of HF theory. [51] The one-electron schrödinger equation can be described as equation 1.3.

$$\left[-\frac{\hbar}{2m} \frac{\partial^2}{\partial r^2} + V_{e-i} + e^2 \sum_j \frac{|\varphi_j(r')|^2}{|r-r'|^2} \right] \varphi_i(r) - \sum_j \delta_{s_i s_j} \int \frac{|\varphi_j^*(r') \varphi_j(r')|^2}{|r-r'|^2} dr' \varphi_i(r) = \varepsilon_i \varphi_i(r) \quad (1.3)$$

The pair-wise electron electron repulsion is replaced by the interaction of the electron i with the average electrostatic field generated by the distribution of the charge of all other electrons and exchange term which keeps electrons of

the same spin way for Pauli's exclusions principles. Although it used the effect one electron equation, the interactions between electrons are considered as each variables.

1.3.3 Density functional theory (DFT)

Hohenberg and Kohn demonstrated that the total energy of many electron system is a unique functional of the electron density and the functional become the minimum at the ground density. Density functional theory is derived from the theory of Hohenberg and Kohn. The one-electron equation becomes as the equation also called as Kohn-sham equation. [52-53] The many variables which considered the each electrons becomes one variable of electron density $n(r)$ which is the square wavefunction of $|\varphi_i(r)|^2$

$$\left[-\frac{\hbar}{2m} \frac{\partial^2}{\partial r^2} + V_{e-i} + e^2 \sum_j \int \frac{n(r')}{|r-r'|^2} dr' + V_{xc}(r)\right] \varphi_i(r) = \varepsilon_i \varphi_i(r) \quad (1.4)$$

$$n(r) = \sum_i^n |\varphi_i(r)|^2 \quad (1.5)$$

$$V_{xc}(r) = \frac{\delta E_{xc}[n(r)]}{\delta n(r)} \quad (1.6)$$

where $V_{xc}(r)$ of equation 1.6 is the exchange-correlation functional which describes the interactions between electrons. Local density approximations (LDA) use the homogeneous electron gas. [54-56] Generalized gradient approximations use the variable of electron density $n(r)$ and addition term of

the gradient of electron density $n'(r)$. [57]

DFT method is much more efficient than HF method due to fewer number of variables. In addition, there are many conventional computational codes for parallel calculations such as Vienna *Ab-initio* Simulation Package (VASP). [58-59]

1.3.4. Underestimation of bandgap and the error of structural parameters

Due to the self-interactions from xc-functional, the bandgap of materials are underestimated. Especially for TCOs such as ZnO and SnO₂, the bandgap using GGA is under 1 eV which is smaller than the visible light rays. Figure 1.6 shows comparison of bandgaps from experimental data and the underestimated problem from DFT. [60-61] In order to overcome the problem, many various methods are tried such as the on-site correction using Coulombic interaction DFT+U method, hybrid density functional method and GW calculations based on quasi-particle theory. [62-66] However, the hybrid density functional method and GW calculations are more than 100 times slower than DFT method.

1.3.5 On-site correction of DFT+U

DFT + U method uses on-site Coulomb interaction (Hubbard-like

term) instead of averaged Coulomb energy. [62-63]

$$E_{\text{local}}^{\text{DFT}+U} = E^{\text{DFT}} + \frac{1}{2}U \sum_{i \neq j} \rho_i \rho_j - \frac{UN(N-1)}{2} \quad (1.7)$$

It treats the on-site Coulomb interaction through orbital-dependent potentials that involve empirical parameters related to on-site (U) and exchange (J) interactions. The last term in equation 1.7 is related to eliminate the double counting of Coulomb interaction. U is defined as

$$U = [E(d^{n+1}) + E(d^{n-1})] - 2E(d^n) \quad (1.8)$$

$E(d^n)$ means the energy of occupied level. J is related to the exchange interaction of spins. Dudarev's method is an efficient method because it use the effective Coulomb potential of U-J. [63]

DFT+U method is very efficient method in order to overcome the bandgap problem because the time cost of DFT+U method is similar to that of DFT. However, the parameter of U and J should be referred to the previous data such as experiments. In addition, the underestimation problem is remained in TCOs such as ZnO and SnO₂. [67-68]

1.3.6 Hybrid density functional theory

Hybrid density functional theory for *ab-initio* calculations is based on the admixture of Fock exchange from HF theory and that from DFT. The improved bandgap can be obtained because the self-interaction error can be

canceled by partially incorporated HF theory.

Perdew *et al.* explained that the optimum mixing coefficient α can be supported by a perturbation theory.[64] They use the value 0.25 for exact exchange α , and this formalism is called PBE0 formulated as follows:

$$E_{xc}^{\text{PBE0}} = \alpha E_x^{\text{HF}} + (1 - \alpha) E_x^{\text{PBE}} + E_c^{\text{PBE}} \quad (1.9)$$

In PBE0, the electron correlation part is identical with the correlation part of the PBE density functional.

Heyd *et al.*, proposed the screened hybrid density functional by using Fock exchange at only short-range from PBE0. [65] The equation 1.10 shows the HSE functional.

$$E_{xc}^{\text{HSE}} = \alpha E_x^{\text{HF,SR}}(\mu) + (1 - \alpha) E_x^{\text{PBE,SR}}(\mu) + E_x^{\text{PBE,LR}}(\mu) + E_c^{\text{PBE}} \quad (1.10)$$

where the screening parameter is μ . HSE03 used the value of 0.3 \AA^{-1} , however, it was revised as 0.2 \AA^{-1} with being called as HSE06. Fock exchange was divided into the short-range (SR) and the long-range (LR) parts with error functions.

$$\frac{1}{r} = S_\mu(r) + L_\mu(r) = \frac{\text{erfc}(\mu r)}{r} + \frac{\text{erf}(\mu r)}{r} \quad (1.11)$$

However, the mixing ratio α of HF of 25 % underestimates the bandgap of TCOs. Additional optimization of α allow the bandgap from HSE06 to those of experimental band gap. [61]

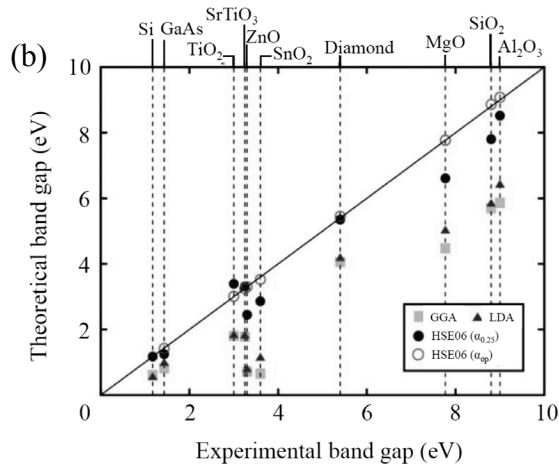
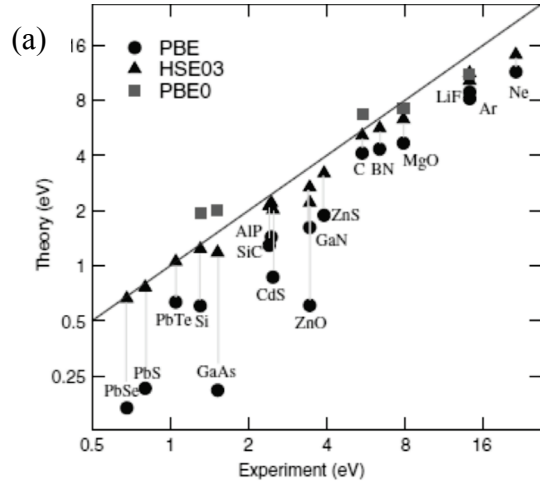


Figure 1.6 The bandgaps of various materials are compared between experiment and theory. (a) From ref. [60]. (b) From ref. [61].

1.4. Object of this study

In this dissertation, first principles calculations which are useful for describing the electronic structure and thermodynamic energy of ground state were used with the analysis of energetics, electronic structures and density-of-state (DOS) diagrams are used for description of the bonding nature, orbitals distributions and predictions of physical and electronic properties of materials. The cells for calculations were optimized with various xc-functionals based on DFT, DFT+U and hybrid functionals.

Ab-initio thermodynamic calculations were performed in order to investigate the with the phonon vibrations. Enthalpy can be used for the comparison of stability of phase using the function of pressure at 0K calculations. However, the temperature is another reasonable function which dominates the thermodynamic stability of phases. Gibbs energy was also involved to compare the thermodynamic stability between phases using pressure and temperature. Pressure-temperature phase diagram can be drawn at the same composition by representing the portion of the phase which includes the minimum Gibbs energy. The compositions were selected when the elements ratio of Zn to Sn to O is 2 : 1: 4 and 1 : 1: 3. These compositions are widely used due to the existence of the single phase and good performance. [5]

At the crystalline phases found by thermodynamic calculations, the

behavior of oxygen vacancy was investigated by using the defect formation energy and electronic structures. The theory about the behavior of oxygen vacancy is not arranged in TCO system. In addition, the investigations of zinc tin oxides are not performed yet. The defect formation energy and electronic structure including the location of defect state teach us whether the oxygen vacancy is deep localized state or shallow electron donor which can be the reason of native n-type doping. In addition, the similar methods were also applied to the hydrogen interstitials.

Finally, melt-quenching method based on the *ab-initio* molecular dynamics (AI-MD) was performed in order to get the amorphous zinc tin oxide phases. The coordination numbers (CN) of each atom of amorphous phases of Zn_2SnO_4 and $ZnSnO_3$ were compared to those of crystalline phases.

The organization of this dissertation is as follows. Chapter 2 reviews the fundamental properties of zinc tin oxides obtained by *ab-initio* calculations. Chapter 3 explains the thermodynamic stability of various phases of zinc tin oxides by considering the thermodynamic variables such as Gibbs energy and enthalpy extracted from the phonon vibrational properties. Chapter 4 presents the effects of representative defects such as oxygen vacancies and hydrogen interstitials in crystalline inverse spinel phase Zn_2SnO_4 . Chapter 5 describes the local structures of the amorphous phases of zinc tin oxide obtained by the *ab-initio* molecular dynamics. Chapter 6 provides the conclusion of the thesis.

Chapter 2. Fundamental properties of zinc tin oxides

2.1. Review of zinc tin oxides

2.1.1. Various synthesis methods of zinc tin oxides

The oxide including Zn and/or Sn can exist as binary oxides and ternary oxides such as Zn_2SnO_4 (*ZTO214*) and $ZnSnO_3$ (*ZTO113*). [5] The inverse spinel phase of *ZTO214* [23-24,69-70] was reported to exist as one solid phase at 1275 °C. [71-72]. The single crystalline *ZTO214* thin film was also reported which was deposited by sputtering method on glass substrate.[23-24] On the other hand, two rhombohedral phases of *ZTO113* were observed: lithium niobate phase (LN) and ilmenite phase (IL), respectively. *LN-ZTO113* was synthesized from the 1:1 mixture of ZnO and SnO_2 by quenching from high pressure over 7 GPa and high temperature of 1000 °C. [25] Meanwhile, *IL-ZTO113* was synthesized by the ion-exchange reaction of Li_2SnO_3 which has the same structure with *IL-ZTO113*. [26]

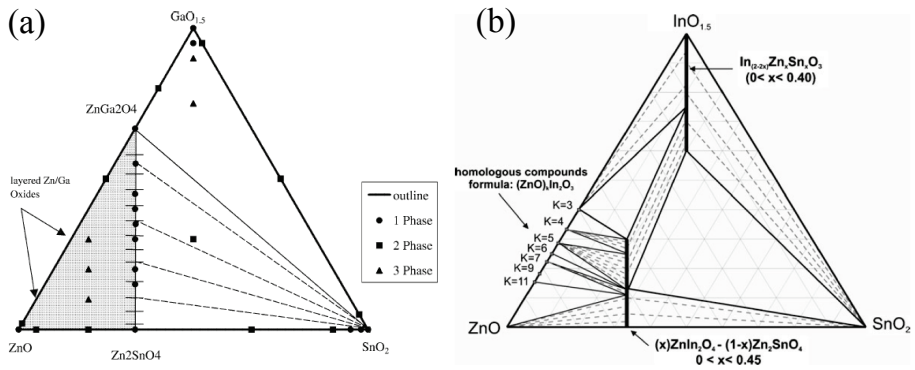


Figure 2.1 Subsolidus ternary phase diagrams of (a) ZnO-GaO_{1.5}-SnO₂ at 1250 °C [71] (b) ZnO-InO_{1.5}-SnO₂ at 1275 °C. [72] Note that Zn₂SnO₄ forms as one phase.

2.1.2. Structural details

The stable phase of the *ZTO214* is reported to be the inverse spinel [23-24,69-70] which is generally known to belong to $Fd\bar{3}m$ as the normal spinel phase. [70] However, this space group is true only when all the octahedral sites are treated as symmetrically identical. The occupancy of octahedral sites by two different elements lowers the symmetry of the structure in the atomic scale. For the *ZTO214*, five configurations were tested for Zn and Sn atoms to fill the octahedral sites and three of them were further investigated; tetragonal phase ($P4_122$, space group 91; *tetra-ZTO214*) [70], orthorhombic phase ($Imma$, space group 74; *ortho-ZTO214*) [73] and monoclinic phase ($P1$, space group 1; *mono-ZTO214*). The other unitcells belonging to the space group of $P4\bar{m}2$ and Cm were found to change into *ortho-ZTO214* by the relaxation of shape and volume of the cells. The primitive cell of each phase was defined in comparison with the conventional unit cell of the cubic spinel as shown in figure 2.2. The configurations of the Zn and Sn in the *tetra-ZTO214* (figure 2.2.a), *ortho-ZTO214* (figure 2.2.b) and *mono-ZTO214* (figure 2.2.c) are noticeably different. According to [010] direction at the viewing of (100) plane of the conventional unit cell, in the *tetra-ZTO214*, the same cations occupy two adjacent octahedral sites in an alternating way, while in the *ortho-ZTO214*, the same cations occupy all the octahedral sites. On the other hand, in the

mono-ZTO214, the cations are randomly distributed without any symmetry. In figure 2.2., primitive cell of each phase is also shown with the relationship between the conventional cubic unit cell and the primitive cell. When the shape and volume of the cells were fully relaxed, the cell angles of *ortho-ZTO214* and *mono-ZTO214* were slightly deviated from the right angle.

For the *ZTO113*, two phases were investigated; lithium niobate phase (R3c, space group 161; *LN-ZTO113*) and ilmenite phase (R-3, space group 148; *IL-ZTO113*) as shown at figure 2.3. They have the rhombohedral primitive cells [74], however, the hexagonal unitcells were adapted for the convenience in the *ab-initio* calculations. In the hexagonal cell, Zn, Sn and vacancy occupy the octahedral sites in different ways. In *IL-ZTO113*, a plane normal to $\langle 0001 \rangle$ direction is occupied by the same cations, whereas it is occupied by Zn, Sn and vacancy in *LN-ZTO113*.

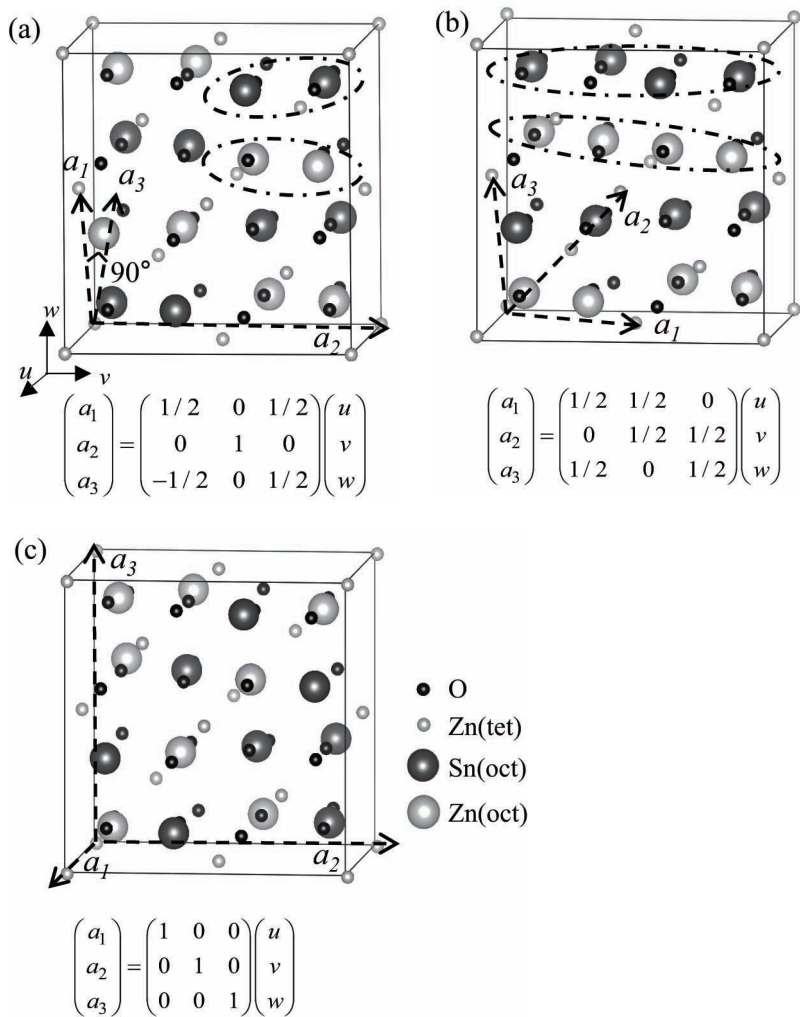


Figure 2.2 Unitcells of inverse spinel *ZTO214*. u , v , and w are the lattice vectors of the conventional unitcell. Dashed vectors of a_1 , a_2 , and a_3 indicate the unit vectors of the primitive cell for (a) *tetra-ZTO214* ($P4_122$), (b) *ortho-ZTO214* ($Imma$) and (c) *mono-ZTO214* ($P1$).

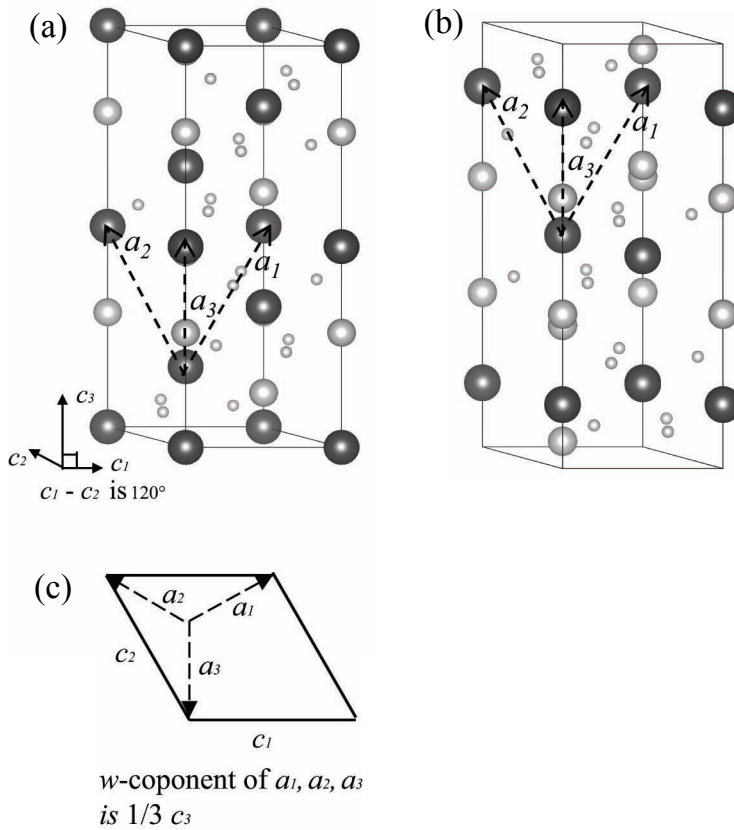


Figure 2.3 Hexagonal unitcells of ZTO113. u , v , and w are the lattice vectors of the conventional unitcell. Dashed vectors of a_1 , a_2 , and a_3 indicate the unit vectors of the primitive cell for (a) *LN-ZTO113* (R3c), (b) *IL-ZTO113* (R-3). (c) The relations between the lattice vector of hexagonal unitcells and the primitive cells on the basal plane of hexagonal unitcells.

2.2. Computational methods

Calculations were performed using Vienna ab-initio Simulation Package (VASP). [58-59] The projector augmented wave (PAW) method [75] within both the local density approximation (LDA) parameterized by Ceperley *et al.* [54] and the generalized gradient approximation (GGA) parameterized by Perdew *et al.*[57] (PBE) were used. The on-site effective Coulomb interactions as given GGA+U [63] and the screened hybrid functional method proposed by Heyd *et al.*, [65] were also used as the exchange-correlation functionals. The effective U value of 7.5 eV for Zn and 3.5 eV for Sn were selected by referring to the previous reports of binary oxides. [67-68] The 3d and 4s orbitals for Zn, 4d, 5s and 5p orbitals for Sn, 2s and 2p orbitals for O were treated as the valence electrons under the non-spin polarized calculations. The 500 eV of cutoff energy was used to guarantee the convergence of the total energy below 1 meV/f.u. Table 2.1 arranged the k -grid conditions.

Table 2.1 Calculation conditions for the various phases of zinc tin oxide.

Composition	Space group (Abbreviation)	Unitcell	# of atoms in unitcell (Zn / Sn / O)	<i>K</i> -points for unitcell
ZnO	P6 ₃ mc	Hexagonal (primitive)	2 / 0 / 2	7x7x5- Γ^a
SnO ₂	P4 ₂ /mnm	Tetragonal (primitive)	0 / 2 / 4	4x4x6-MP ^b
ZnSnO ₃	R3c (LN-)	Hexagonal	6 / 6 / 18	5x5x2- Γ
	R-3 (IL-)	Hexagonal	6 / 6 / 18	5x5x2- Γ
Zn ₂ SnO ₄	P4 ₁ 22 (tetra-)	Tetragonal (primitive)	8 / 4 / 16	4x2x4-MP
	Imma (ortho-)	FCC-like ^c (primitive)	4 / 2 / 8	5x5x5- Γ
	P1 (mono-)	Monoclinic	16 / 8 / 32	2x2x2-MP

^a Γ -centered^bMonkhorst-Pack [76]^cThis cell is deviated from the primitive cell of the normal spinel, which belongs to the space group Fd-3m.

2.3. Optimized structures

Table 2.2 and table 2.3 show the volume of the unitcell and bulk modulus of each phase by various xc-functionals in comparison with the experimental values and some previous calculation results. ZnO in the wurtzite structure and SnO₂ in the rutile structure were also calculated as references. The volume and bulk modulus were obtained from the third Birch-Murnaghan equations of state (BM-EOS) which is expressed as equation 2.1. [77]

$$E = E_0 + \frac{9}{16} V_0 B_0 \left[\left\{ \left(\frac{V_0}{V} \right)^{\frac{2}{3}} - 1 \right\}^3 B_0' + \left\{ \left(\frac{V_0}{V} \right)^{\frac{2}{3}} - 1 \right\}^2 \left\{ 6 - 4 \left(\frac{V_0}{V} \right)^{\frac{2}{3}} \right\} \right] \quad (2.1)$$

where, E_0 , V_0 , B_0 , B_0' are the system energy of the optimized structure, volume of the optimized structure, bulk modulus and its pressure derivative, respectively. The difference between the energy obtained using the relaxed volume and that obtained using the fitted volume to EOS were negligibly small below 1 meV/f.u. The calculated volumes of the optimized cells agree well with the experimental data within the error of 5 %. The volumes obtained by LDA are slightly smaller and those obtained by GGA calculations are slightly larger than the experimental values as observed in many other materials. [78] The volumes by using LDA calculations were closer to the experimental data than those by using GGA calculations.

The bulk moduli of ternary oxides of *ZTO113* have hardly been

experimentally reported as far as the authors' knowledge. The calculated bulk moduli of binary oxides, ZnO and SnO₂ were compared to the experimental data. The bulk moduli from the LDA calculations were closer to the experimental values, however, those from the GGA calculations were quite low, implying the calculated system by the GGA calculations is too soft than the real system. The bulk moduli of the three *ZTO214* phases are similar regardless of the space group, i. e., the configuration of the octahedral sites within the same exchange-correlation functionals. On the contrary, *LN-ZTO113* phase shows somewhat higher bulk modulus than *IL-ZTO113*.

Table 2.2 Unitcell volumes of zinc tin oxides.

Composition Space group (Abbreviation)		Volume ($\text{\AA}^3/\text{f.u.}$)				
		Exp.	LDA ^a	GGA ^b	GGA+U	Opt-HSE06 B3LYP
ZnO	P6 ₃ mc	This work	22.86	24.88	22.85	24.03
		References	23.80[79]	22.87 ^a [80]	24.83[80]	
SnO ₂	P4 ₂ /mnm	This work	35.78	37.80	35.79	35.94
		References	35.75[81]	34.94 ^c [82]		
ZTO113	R3c (LN-)	This work	54.99	58.72	55.11	56.07
		References	55.95[67]	58.60 ^a [84], 60.08[85]		
			54.15 ^c [86]			
	R-3 (IL-)	This work	55.50	59.68		57.08
		References	56.78[26]	56.29 ^c [86]	60.82[85]	
ZTO214	Fd-3m ^d	References	81.11 ^c [69,87]			
	P4 ₁ 22 (tetra-)	This work	78.89	84.96	79.11	81.62
	Imma (ortho-)	This work	78.91	85.02	79.16	81.54
		References				83.74[73]
P1 (mono-)	This work	79.25	85.40	79.45		

^aLDA parameterized by Ceperley *et al.*[54], ^bGGA Parameterized by Perdew *et al.*[56]

^cLDA parameterized by Vosko *et al.*[55]

^dDisordered inverse spinel

^eNo method was reported.

Table 2.3 Bulk moduli of zinc tin oxides.

Composition	Space group (Abbreviation)	Bulk modulus (GPa)				
		Exp.	LDA ^a	GGA ^b	GGA+U	B3LYP
ZnO	P6 ₃ mc	This work		161	128	134
		References	183[79]	162 ^a [80]	134[80]	114[73]
SnO ₂	P4 ₂ /mnm	This work		202	173	178
		References	205[81]	245 ^c [39]		221[83]
ZTO113	R3c (LN-)	This work		195	167	172
		References			161[85]	
	R-3 (IL-)	This work		173	137	
		References			141[85]	
ZTO214	Fd-3m ^d	References	169 ^e [88]			
	P4 ₁ 22 (tetra-)	This work		173	142	146
	Imma (ortho-)	This work		170	139	144
		References				186[73]
	P ₁ (mono-)		167	133		

^aLDA parameterized by Ceperley *et al.*[54] ^bGGA Parameterized by Perdew *et al.*[56]

^cLDA parameterized by Vosko *et al.*[55]

^dDisordered inverse spinel

^eNo method was reported.

2.4. Electronic structures

Electronic structure are used for the knowing various properties of materials. In general, the first Brillouin zone is used for seeing the band structure. However, sometimes the pseudo-band structures are used in the case of including the defects of supercell method. Table 2.4 shows the bandgaps of all the phases of zinc tin oxides.

All of *ZTO214* phases show the direct bandgap at Γ . However, the result of DFT was about 30 % of underestimation. DFT+U method was also obtained, however, the underestimation of about 70 % was remained. In order to get the same bandgap with the experimental value of 3.6 eV [21,23], the optimized HSE06 was used. The ratio of HF 29 % was fitted to the experimental value as 3.56 eV which is almost the same as the experimental value using $P4_122$ phase.

The experimental bandgaps of *ZTO113* were not reported yet. *LN-ZTO113* shows the direct bandgap at like *ZTO214* phases and binary oxides of ZnO and SnO₂. When the same xc-functionals are used, the bandgap of *LN-ZTO113* was higher than those of *ZTO214* phases. *IL-ZTO113* shows the indirect bandgap. ZnO and SnO₂ also have direct bandgap. [67-68] The higher mixing ratio of HF was needed to get the similar bandgap of experimental data.

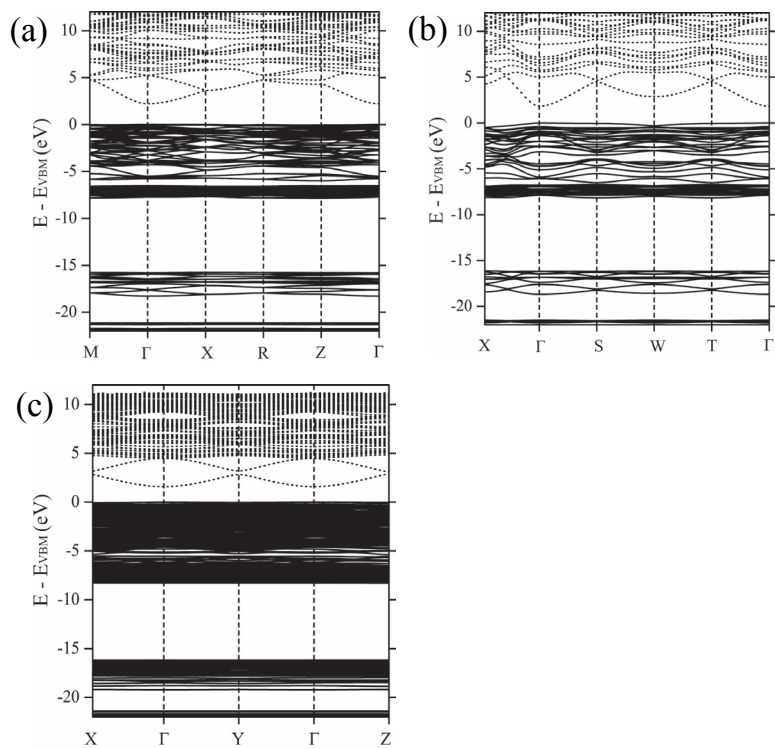


Figure 2.4 Electronic structures of *ZTO214*. (a) *tetra-ZTO214* ($P4_22$) (b) *ortho-ZTO214* ($Imma$) (c) *mono-ZTO214* ($P1$).

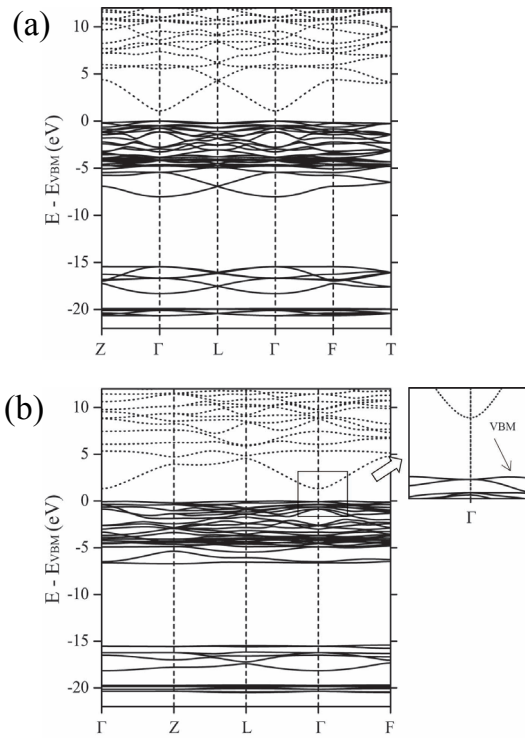


Figure 2.5 Electronic structures of ZTO113. (a) LN-ZTO113 (b) IL-ZTO113.

Table 2.4 The bandgap of *ZTO214* and *ZTO113* from various xc-functionals

xc-functionals	Bandgap (eV)						
	<i>ZTO214</i>		<i>ZTO113</i>		ZnO	SnO ₂	
Composition	<i>P4₁22</i>	<i>Imma</i>	<i>P1</i>	<i>R3c</i>	<i>R-3</i>	<i>P6₃mc</i>	<i>P4₂mnm</i>
Exp.	3.3 – 3.9		-		3.4	3.6	
PBE	1.37	0.76	0.63	1.08	1.41	0.80	0.65
PBE+U _{eff} ^a	2.20	1.83	1.58	2.11	2.40	1.80	1.38
HSE06	3.33	-	-	-	-	2.15	2.91
opt-HSE06 ^b	3.58	3.13	2.83	3.51	3.80	3.38 ^c	3.57 ^d

^aOn-site Coulombic interaction is 7.5 eV for Zn and 3.5 eV for Sn.

^bFor ternary oxides, mixing ratio (α_{mix}) was used for 29 %.

^c α_{mix} of ZnO is 37.5 %. [61,67]

^d α_{mix} of SnO₂ is 32 %. [61]

2.5. Density of states (DOS)

From figure 2.6 to figure 2.10, the density of states (DOS) analyses of ternary oxides are obtained. All the intensities of projected DOS (PDOS) were obtained from the one atom. The general tendencies of forming the DOSs from the orbitals are similar among the various phases. The deep states from -20 eV to -15 eV under the valence band maximum (VBM) are consist of the 2s-orbitals of oxygens and the 4d-orbitals of tins. The other deep states from -8 eV to -5 eV under the VBM, the localized peaks are made from the 2p-orbitals of O and the 3d-orbitals of Zn. The VBM are mainly formed by the 3d-orbitals of Zn and the 2p-orbitals of O. The conduction band minimum (CBM) is formed by the 5s-orbitals of tins. Above the CBM, the 2p-orbitals of O and the 4s-orbitals of Zn join to form the conduction bands. The DOS result agree with the previous hypothesis which the large spherical s-orbitals of cations mains form the conduction bands. [3]

Figure 2.6, 2.7 and 2.8 describe the DOSs from various unitcells of *ZTO214*. For figure 2.6 and 2.7, the O-I site indicates the site which is neighbored to three Zn atoms and one Sn atom, the O-II site indicates the site which is neighbored to two Zn atoms and two Sn atoms. The DOS peaks from different oxygen sites were almost same. On the other hands, the DOS peaks at the VBM from 3d-orbitals of two Zn sites were different each other.

The attribution to the VBM from the 3d-orbital at the octahedral site of Zn was larger than that at the tetrahedral site of Sn. The different occupancies of octahedral sites do not affected the DOS results.

Figure 2.9 and 2.10 show the DOSs from *LN-ZTO113* and *IL-ZTO113*, respectively. However, the general tendencies of forming DOSs are similar as those of *ZTO214* phases.

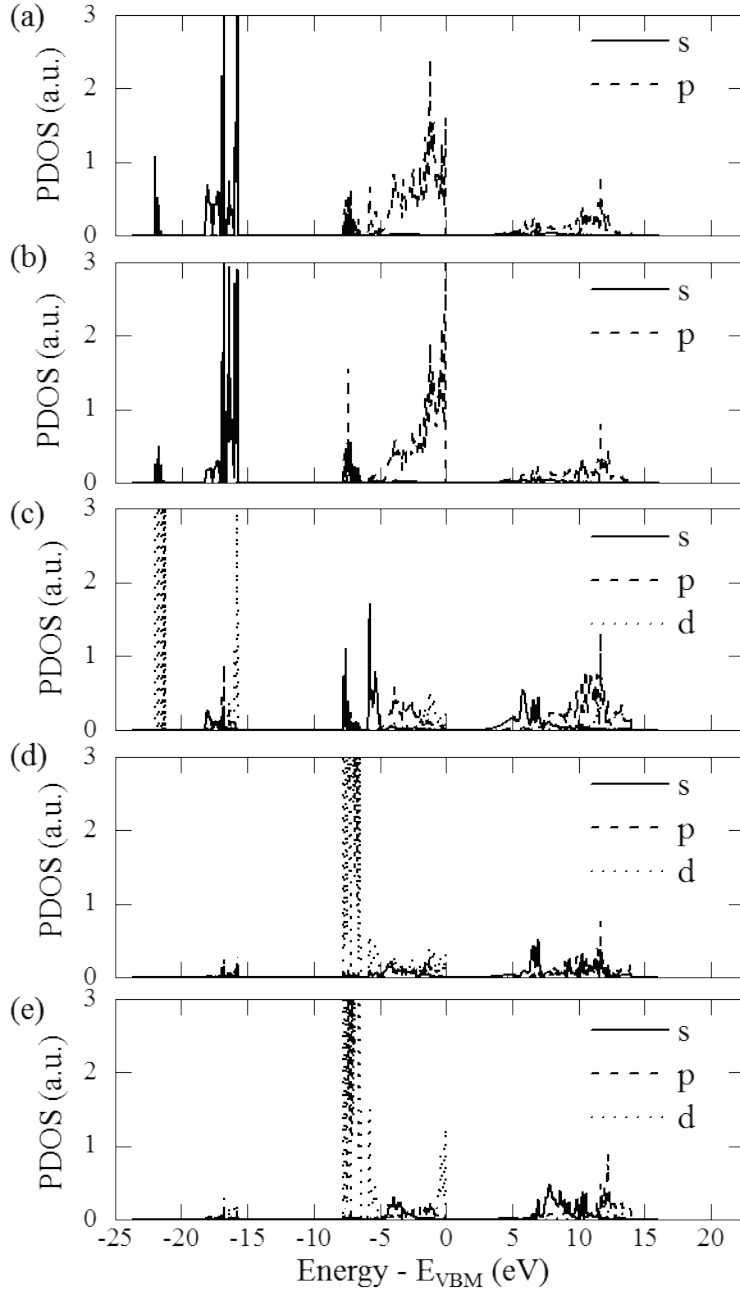


Figure 2.6 PDOS of *tetra-ZTO214*. (a) From O at site O-I. (b) From O at site O-II. (c) From Sn. (d) From Zn at tetrahedral site. (e) From Zn at octahedral site.

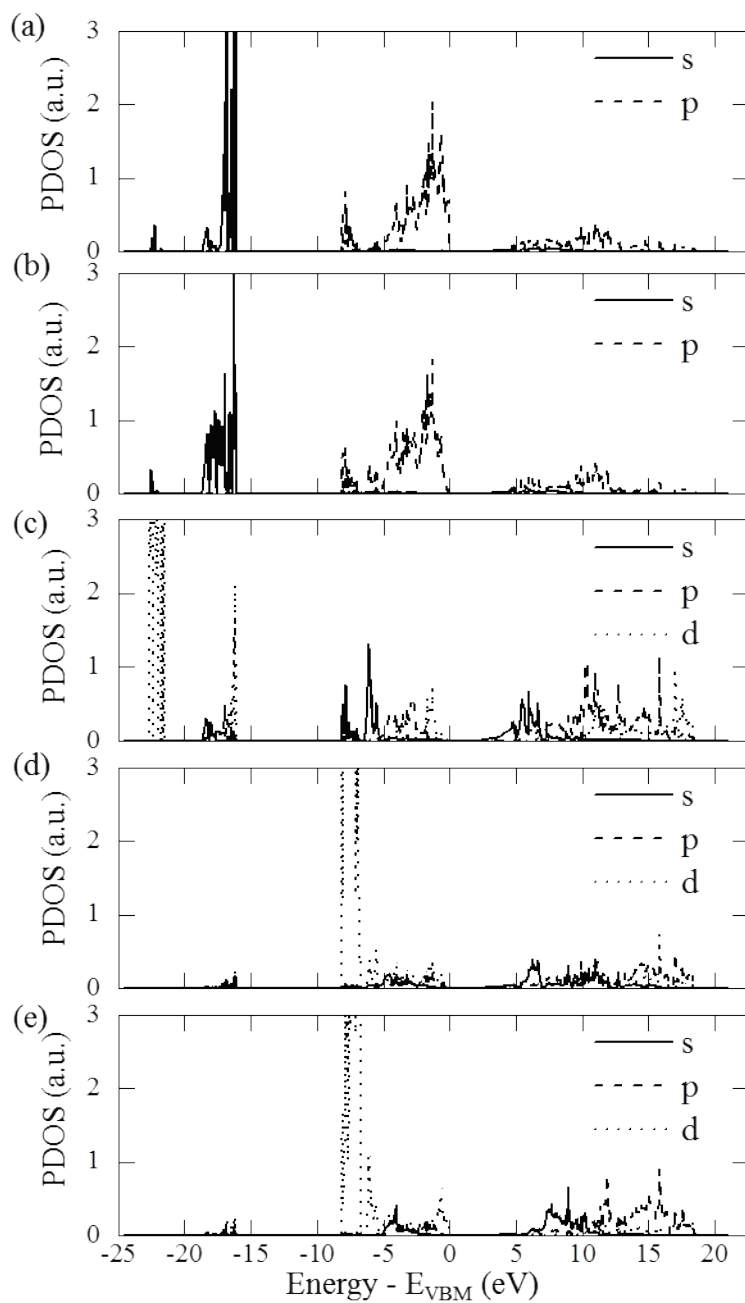


Figure 2.7 PDOS of *ortho*-ZTO214. (a) From O at site O-I. (b) From O at site O-II. (c) From Sn. (d) From Zn at tetrahedral site. (e) From Zn at octahedral site.

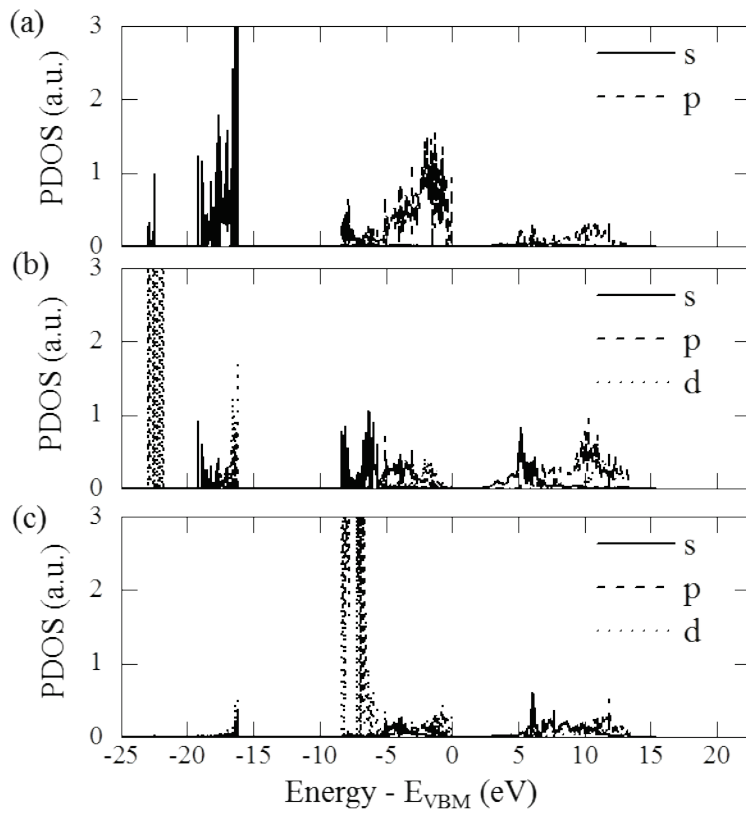


Figure 2.8 PDOS of *mono-ZTO214*. The intensities of PDOS peaks are divided into the number of each atom. (a) From O. (b) From Sn. (c) From Zn.

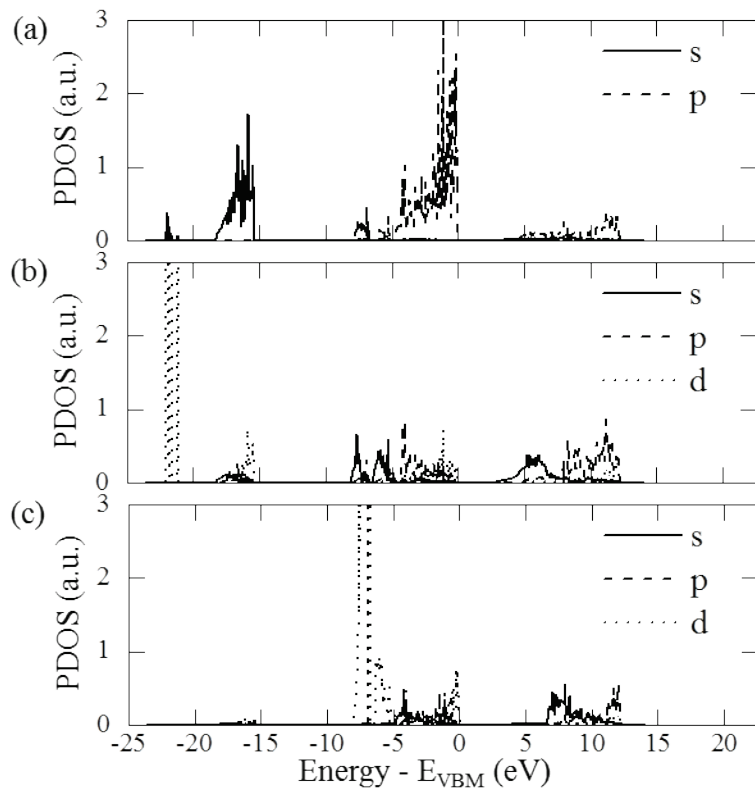


Figure 2.9 PDOS of *LN-ZTO113*. (a) From O. (b) From Sn. (c) From Zn.

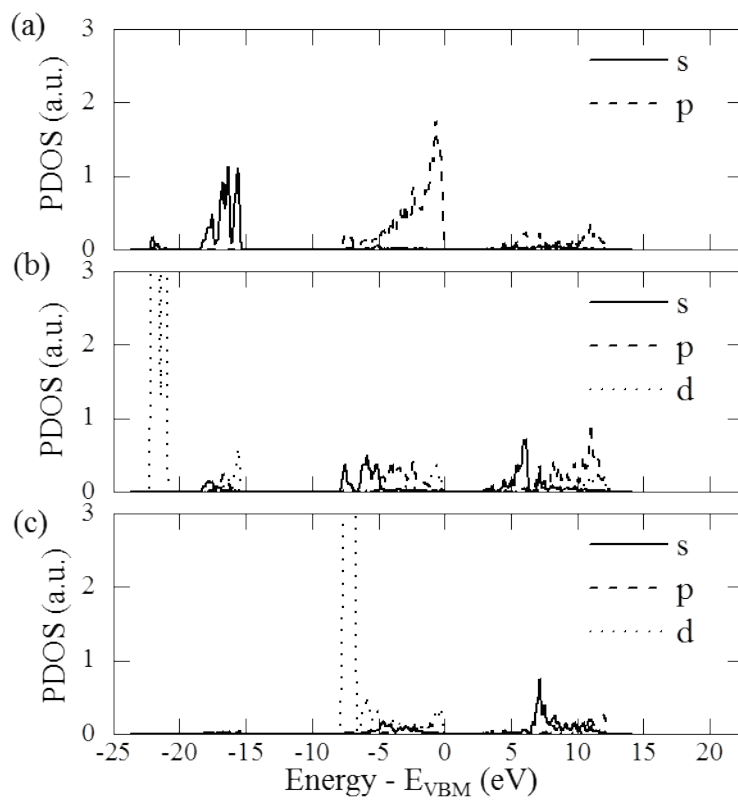


Figure 2.10 PDOS of *IL-ZTO113*. (a) From O. (b) From Sn. (c) From Zn.

Chapter 3. Thermodynamic stability of various phases of zinc tin oxides

3.1. Overview

As mentioned at chapter 2, zinc tin oxide has various phases and easy tendency to form amorphous phases. Therefore, understanding the crystalline phases and their thermodynamic stability is prerequisite to figure out the amorphous structure and even nanostructure. The *ab-initio* phonon calculations were also carried out to obtain the enthalpy and Gibbs energy, which were used to investigate the effects of both pressure and temperature on the thermodynamic stabilities of zinc tin oxide phases. The pressure-temperature phase diagram was obtained at the composition having the atomic ratio of Zn to Sn to O is 1 : 1 : 3 and compared to the previous synthesis or existence conditions of various zinc tin oxide phases. The composition of Zn to Sn to O is 2 : 1 : 4 was also considered. For this composition, several space groups of the inverse spinel structure were examined.

The previous *ab-initio* calculations reported that the pressurization changes the thermodynamic stability from the coexistence of ZnO and SnO₂ into the coexistence of *ZTO214* and SnO₂. [73,89-90] However, these calculations were based only on the enthalpy and the reported transition

pressure varies from 0 to 12 GPa. Meanwhile, the space group of the inverse spinel structure varies according to the occupancy of the octahedral site by Zn and Sn in the scale of unitcell [70] Seko *et al.* reported the most stable structure of *ZTO214* belongs to the space group of $P4_122$. [70] On the other hand, Gracia *et al.* calculated the phase stability of the *ZTO214* which belongs to the space group of $Imma$. [73] Nakayama *et al.* reported they calculated the most stable structure of *ZTO214* but did not specify the space group. [89] Different exchange-correlation functionals (xc-functionals) used in the previous calculations showed the different optimized structures and energetics, which might affect the thermodynamic stability. Moreover, temperature is also an important thermodynamic variable to determine the stability of the materials and to understand the properties at the practical synthesizing and working temperatures. However, the previous *ab-initio* calculations investigated only the pressure effect at 0 K and did not include the phonon properties, which account for the temperature effect.

3.2. Thermodynamic variables

Enthalpy describes the thermodynamic stability of the state at a certain pressure. The most stable phases at a certain pressure can be determined by comparison of enthalpies of phases. In addition, the Gibbs energy describes the thermodynamic stability of a state at a certain pressure

and temperature. The most stable phases at a certain pressure and temperature can be determined by comparison of Gibbs energies of phases.

Figure 3.1 shows the schematic diagram of the energy-volume (E-V) curve and the phase transition point of the two phases by pressurization. From the ab-initio calculation, the total energy of the electronic structure, $E(V)$ can be obtained with the change of volume at 0K for both A and B phases. The optimized volumes, V_A^0 and V_B^0 can be determined by finding the lowest total energies of the electronic structure, E_A^0 and E_B^0 , respectively, under the zero external pressure, which were expressed as solid lines. Then, $E(V)$ can be transformed to enthalpy, $H(p)$ by adding pV term, [80] which can be expressed as;

$$H(p) = E(V) + pV \quad (3.1)$$

where, $H(p)$ is the enthalpy which uses pressure, p as a variable, $E(V)$ is the total energy of the electronic structure and V is the volume, respectively. The pressure is the negative tangent of the E-V curve, where positive pressure means the external compression. When the tangent line meets the axis of the energy, the intercept becomes the enthalpy. Therefore, the common-tangent line of the two E-V curves (shown as the solid bold line) means that the enthalpies of two systems are the same as H^{Tr} and the phase transition can occur by pressurization.

In addition, this transform can be more simply described. Figure 3.2.a illustrates how to add the pV term to the total energy of the electronic

structure for a given volume at 0 K as the equation 3.1 in order to consider the external hydrostatic pressure. The solid circles indicate the E-V curve at zero external pressure at 0K, which are the total energies of the electronic structure for a given volume. On the other hand, the open circles indicate those under the external pressure. Then, the minimum thermodynamic value for a given pressure was found and linked by the dashed line, indicating the higher the external compressive pressure, the smaller the equilibrium volume is.

When the phonon calculations are involved in the *ab-initio* study, the temperature effects can be also included to determine the thermodynamic stability. For any point at the E-V curve, the phonon frequency can be obtained by the linear response method based on the density functional perturbation theory (DFPT) [91]. Then, the Helmholtz phonon vibrational energy can be calculated for a given volume and temperature by the quasi-harmonic approximation (QHA) as shown in equation 3.2,

$$F_{vib}(V, T) = \frac{1}{2} \sum_k \hbar \omega(k) + k_B T \sum_k \ln[1 - \exp(-\hbar \omega(k) / k_B T)] \quad (3.2)$$

where, ω is the phonon vibrational frequency, k_B is Boltzmann constant, T is the absolute temperature, respectively. [78, 92-93] Note that the Helmholtz phonon vibrational energy is composed of the temperature-free term and the temperature-dependent term. In addition, other thermodynamic variable which used the variable of volume such as Helmholtz vibrational entropy and the heat capacity can be expressed as equation 3.3 and 3.4.

$$S_{vib}(V, T) = -k_B \sum_k \ln[1 - \exp(-\hbar \varpi(k) / k_B T)] - \frac{1}{T} \sum_k \frac{\hbar \varpi(k)}{\exp(\hbar \varpi(k) / k_B T) - 1} \quad (3.3)$$

$$C_V(T) = \sum_k k_B \left[\frac{\hbar \varpi(k)}{k_B T} \right]^2 \frac{\exp(\hbar \varpi(k) / k_B T)}{[\exp(\hbar \varpi(k) / k_B T) - 1]^2} \quad (3.4)$$

Figure 3.2.b shows how to calculate the temperature effect as shown in the equation 3.2. The curve composed of the solid circles is identical with that in figure 3.2.a, whereas the curve composed of solid rhombi was obtained by adding the first term of the equation 3.2, to include the temperature-independent vibrational property. The other E-V curves represented by open rhombi were obtained for various temperatures and the minimum thermodynamic value for a given temperature was found and linked by the dashed line. It is noted that the magnitude of $F_{vib}(V, T)$ term becomes larger as the temperature increases and this tendency is more significant at larger volume. These behaviors result in the increase in the equilibrium volume which describes the thermal expansion.

By combining the equations 3.1 and 3.2, Gibbs energy is defined as the minimum value with respect to the volume for a given p and T as equation 3.5. [78, 92-93] The points on E-V curve were fitted to Birch-Murnaghan equation of state (BM-EOS) before the determining of minimum value. [77]

$$G(p, T) = \min_V [E(V) + pV + F_{vib}(V, T)] \quad (3.5)$$

Gibbs energy can be used to determine the phase stability and phase transition. In this chapter, the “transition” will be used to describe the onset point of changing the thermodynamic stability, which is the prerequisite for

the real occurrence of the phase transformation.

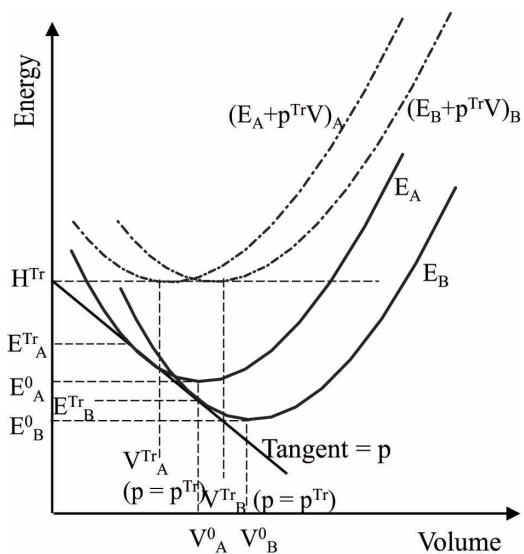


Figure 3.1 Schematic diagram of the E-V curve and the phase transition by pressurization. E, p and H mean the total energy of electronic structure obtained from *ab-initio* calculation, pressure, and enthalpy, respectively. The subscripts A and B indicate two different phases. The superscripts 0 and Tr denote the optimized structure and the transformation by pressure.

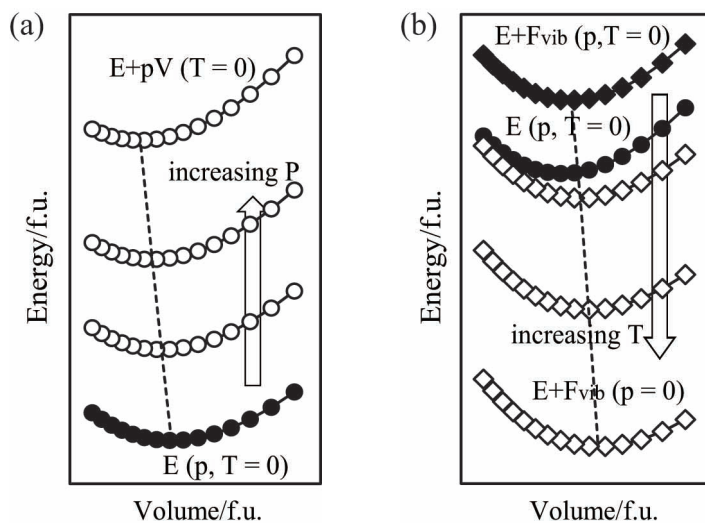


Figure 3.2 Schematics illustrations to obtain the Gibbs energy as a function of the cell volume. The energy can be extracted using (a) $E+pV$ to consider the pressure effect ($T=0$) and (b) $E+F_{vib}$ to consider the temperature effect ($p=0$).

3.3. Computational methods

Calculations were performed using Vienna *ab-initio* Simulation Package (VASP). [58-59] The projector augmented wave (PAW) method [75] within both the local density approximation (LDA) parameterized by Ceperley *et al.* [54] and the generalized gradient approximation (GGA) parameterized by Perdew *et al.* (PBE) [56] were used with the cutoff energy of 500 eV. The 3d and 4s orbitals for Zn, 4d, 5s and 5p orbitals for Sn, 2s and 2p orbitals for O were treated as the valence electrons under the non-spin polarized calculations. The cutoff energy and k-grid were set to guarantee the convergence of the total energy below 1 meV/f.u.

To obtain the E-V curve, the energies at 15 different volumes which were obtained by pressurization were calculated for all the phases considered. The calculations were performed by two steps. At the first step, the relaxation of the cell parameters and internal atomic coordinates were performed when the external pressure, p , ranging from -14 GPa to 14 GPa were applied with the interval of 2 GPa. Note that the positive pressure denotes the hydrostatic compression and vice versa. At this step, the reduced or expanded volumes of the unitcell were obtained as the open circles with x-mark in figure 3.3.a. The electronic iterations were performed until the energy differences became less than 10^{-6} eV and the atomic relaxations were performed until the maximum force between atoms became less than 10^{-3}

$\text{eV}/\text{\AA}$, respectively. Note that all the phases considered in this study show the anisotropic change of the cell parameters under the hydrostatic pressure due to their non-cubic symmetry. At the second step, the static calculations were performed without changing the volume and shape of the unitcell and atomic coordinates. Then, the total energy of the electronic structure for a given V , $E(V)$, was obtained as the solid circles in figure 3.3.a. Finally, the E-V curve with 15 points was fitted to BM-EOS [77] to calculate the optimized unitcell volume and bulk modulus of each phase at 0K.

The coexistence of two phases under the same external pressure was obtained by the sum of the E-V curves of the two phases as schematically shown in figure 3.3.b. The x- and y-axes represent the sum of the unitcell volume and the sum of the total energy of electronic structure of the two phases, respectively. The summation of the unitcell volume and the total energy was made at each external hydrostatic pressure. For example, the energy of the coexistence of the phase 1 and phase 2 at pressure p_2 is the sum of the energy of the phase A at pressure p_2 and that of the phase B at pressure p_2 .

The linear response method based on the DFPT was performed in order to calculate the force constants of the supercells. [91] The iterations of the electronic steps were performed until the energy differences become less than 10^{-8} eV. The Helmholtz vibrational energies were used to confirm the convergence of supercells and k-points, which are less than 1 meV/f.u. The

phonon vibrational frequency and phonon density of state were calculated from force constants using PHONOPY code. [92-93]

Gibbs energy was determined in the range of 0~14 GPa with the interval of 0.1 GPa and in the range of 0~1600 K with the interval of 5 K. Then, the pressure-temperature phase diagram was delineated. At each pressure, only one transition point of temperature was counted at one reaction by elevating temperature from 0K.

The effects of cation disordering for the octahedral sites in ZTO214 will be discussed at chapter 3.4.6.

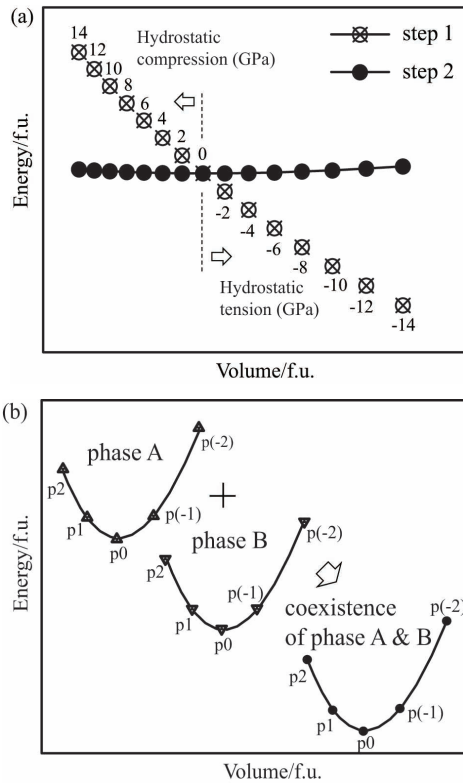


Figure 3.3 (a) Schematic illustration to draw the E-V curve. The volume at the step 1 is maintained at the step 2. (b) The summation of energy and volume were performed under the same hydrostatic pressure. The Positive and negative values means the hydrostatic compressive and tensile stress, respectively.

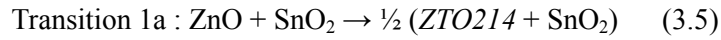
3.4. Results and discussions

3.4.1. Thermodynamic stability by enthalpy

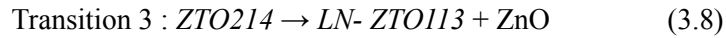
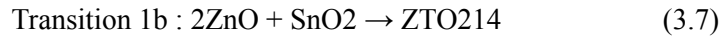
Most of the calculation results will be described at the composition having the atomic ratio of Zn to Sn to O is 1 : 1 : 3, which will be referred to as the *ZTO113 composition*. Some results will be also described at the at the composition having the atomic ratio of Zn to Sn to O is 2 : 1 : 4, which will be referred to as the *ZTO214 composition*.

Figure 3.4.a and figure 3.4.b show the calculated total energies of electronic structures with respect to the volume of various zinc tin oxides using the LDA and GGA functionals for the *ZTO113 composition*, respectively. As explained in figure 3.3.b, the coexistence condition was described by the summation of the volume and total energy under the same external pressure. The arrow in figure 3.4.b indicates thermodynamic variables of *IL-ZTO113* are not reliable showing the abnormal curve by the change of pressure or temperature. The transition pressure is the negative common tangent of the E-V curve fitted to BM-EOS because compression is defined as positive. It is pointed out that, at the transition pressure, the enthalpies of the two coexisting phases are the same and represented by the intercept of the tangent line at the axis of the energy. The general tendency of the E-V curve and the thermodynamic stability are the same for both xc-

functionals; transition from the coexistence of ZnO and SnO₂ at the zero external pressure to the coexistence of *tetra-ZTO214* and SnO₂, and then to *LN-ZTO113* as the external hydrostatic pressure increases. From now on, the transition reaction of the thermodynamic stability was defined as follows:



The transition reactions at the *ZTO214 composition* were also defined as:



The sequence of the transition 1 and the transition 2 by pressure was the same as the previous reports which only considered the enthalpy. [89-90] The transitions 1a and 1b show the minimum pressure for the *ZTO214* to be stable. The transition 2 and 3 show the minimum pressure for the *ZTO113* to be stable at the *ZTO113* and *ZTO214 composition*, respectively.

For the *ZTO113 composition*, as shown at figure 3.4, the pressure of transition 1a was calculated to be the same as 3.1 GPa by the LDA calculations and 3.2 GPa by the GGA calculations, respectively. The transition 2 was calculated to occur at 8.5 GPa by the LDA calculations and at 12.3 GPa by the GGA calculations, respectively.

Nakayama *et al.* reported the transition pressures of transition 1 and 2 are 0 and 0.8 GPa, respectively. [89] However, they pointed out the three

reasons of underestimation; the softness of GGA functional, excluding the temperature effect and the method of selecting the occupancy of Zn and Sn in the unitcell. In this chapter, these three drawbacks were returned by testing the LDA functional as well as the GGA functional, by using Gibbs energy to estimate the thermodynamic stability and by investigating several atomic configurations in both *ZTO113* and *ZTO214*.

With the assumption that the unitcell of *ZTO214* is *ortho-ZTO214*, the transition pressure was calculated to be significantly different. Similarly as the p-T phase diagram, the LDA calculations did not show the transition from the coexistence of ZnO and SnO₂ to the coexistence of the tetra-*ZTO214* and SnO₂, but predicted the direct transition from the coexistence of ZnO and SnO₂ to LN-*ZTO113* at 5.8 GPa. On the other hand, the transition 1 and 2 of the *ortho-ZTO214* occurred at 7.3 GPa and 9.7 GPa using by GGA calculations. Although the absolute values are different from the current results, the shallow range of the stable co-existence of *ZTO214* and SnO₂ is similar to result reported by Gou *et al.* [90] Therefore, it is assumed that they calculated the orthogonal Imma cell.

Table 3.1 shows the transition pressures of our calculation results and previous reports. At the *ZTO113* composition, the sequence of the transition 1 and the transition 2 by pressure was the same as the previous reports which only considered the enthalpy. [89-90] At the *ZTO214 composition*, the sequence of transition 1 by the external pressure also agrees

with the previous reports on *ZTO214*. [73] However, the transition pressure differs presumably due to the different calculation conditions such as the xc-functionals and the space groups of the unitcells.

Table 3.1 Transition pressure and temperature at the *ZTO113* composition by Gibbs energy or enthalpy.

Thermodynamic variable	Ref.	Space group of ZTO214	xc-functionals	Transition Pressure 1 ^a (GPa)	Transition Pressure 2 ^b (GPa)
G	this work	P4 ₁ 22	LDA ^c	2.3 (0K), 1.7 (1073K), 0.6 (1273K)	7.2 (0K), 5.6 (1073K), 11.7(0K),10.5 (1073K), 9.9 (1273K)
			GGA ^d	2.4(0K) , 0 (1073K)	
H	this work	P4 ₁ 22	LDA ^c	3.1 (0K)	8.5 (0K)
			GGA ^d	3.2 (0K)	12.3 (0K)
H	[89]	NA ^{e,f}	GGA	~0 (0K)	0.8 (0K)
H	[73]	Imma	B3LYP	12 ^c (0K)	
H	[90]	NA ^e	GGA	5.9(0K)	7.1 (0K)

^aequation 5 or 7

^bequation 6

^cLDA parameterized by Ceperley *et al.*[54], ^dGGA Parameterized by Perdew *et al.*[56]

^eNA ; not available

^fThe authors of this reference reported they calculated the most stable structure of *ZTO214* but did not specify the space group.

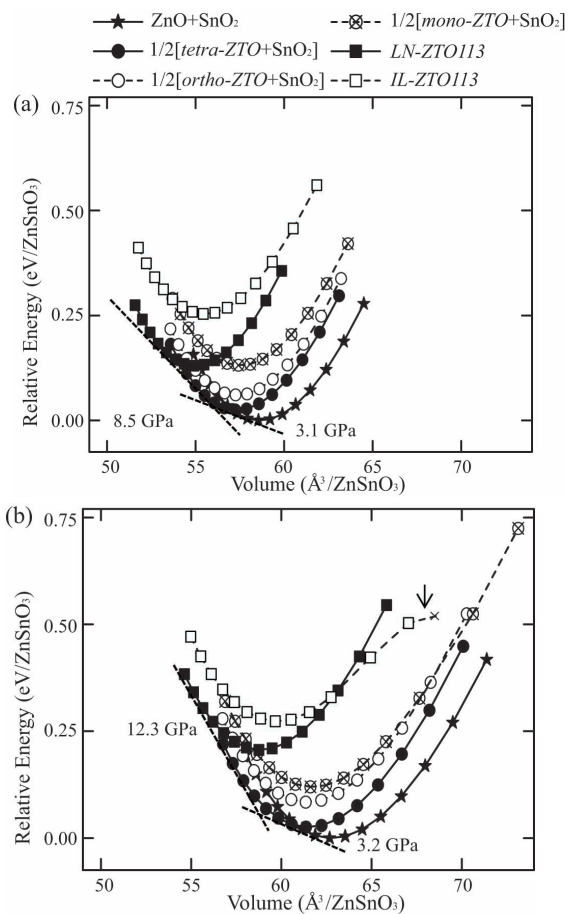


Figure 3.4 E-V curve obtained by the (a) LDA and (b) GGA calculations. The negative common tangent means the transition pressure. The arrow in (b) means that the curve becomes meaningless for *IL-ZTO113* under the external pressure over -10 GPa.

3.4.2. Phonon density of states

Figure 3.5 shows the phonon density of states obtained by the LDA calculations under the zero external pressure, -14 GPa of tensile hydrostatic pressure and 14 GPa of compressive hydrostatic pressure, respectively. The general tendency obtained by the GGA calculations is the same. (not shown) The maximum frequency of each phase under the compressive pressure is all higher than that at the zero pressure and the tensile pressure. It should be pointed out that the peaks at the region of the negative frequency indicate the instability of the material. [78] For the several oxides investigated, only *IL-ZTO113* shows the negative frequencies under the high tensile hydrostatic pressure in figure 3.5.f, indicating this phase is unstable at the tensile region and cannot exist even as metastable.

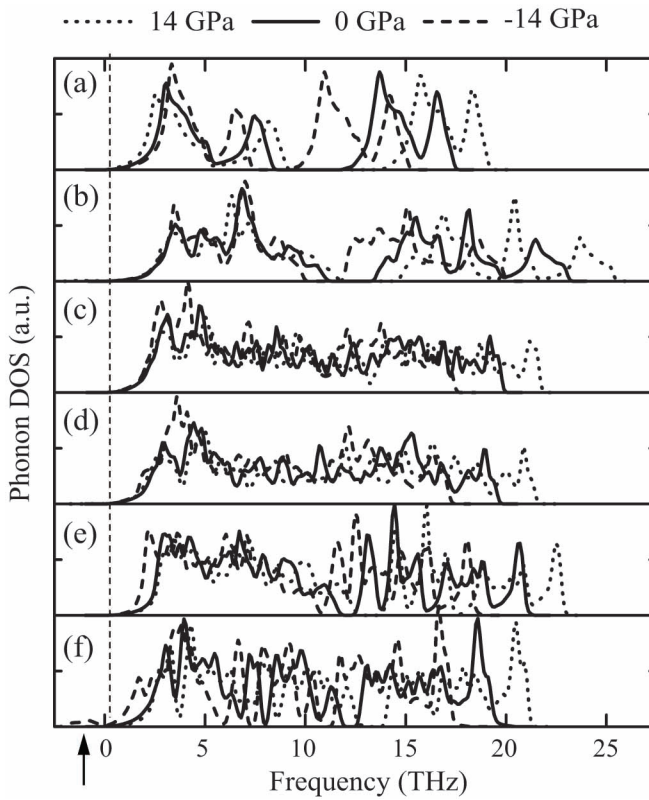


Figure 3.5 Phonon DOSs of (a) ZnO (b) SnO₂ (c) *tetra-ZTO214* (d) *ortho-ZTO214* (e) *LN-ZTO113* and (f) *IL-ZTO113* at -14, 0 and 14 GPa. The arrow indicates the negative phonon frequency in *IL-ZTO113* at -14 GPa.

3.4.3. Thermodynamic stability by Gibbs free energy

Gibbs energy was calculated for all the phases of ZnSnO *except IL-ZTO113* and *mono-ZTO214*. *IL-ZTO113* was excluded because it showed the imaginary phonon frequency under the tensile pressure as shown in figure 3.5.f. Figure 3.6 shows the Gibbs energies as a function of temperature for the various phases at the *ZTO113* composition. The temperature range from 0 K to 1600 K was selected according to the report that 1600 K is the maximum temperature for the existence of *ZTO214*. [71-72] The coexistence of ZnO and SnO₂ was used as the references of the Gibbs energy.

At zero external pressure, the LDA calculations in figure 3.6.a shows the coexistence of ZnO and SnO₂ was the most stable from 0K to 1365 K. At 1365K, the coexistence of *tetra-ZTO214* and SnO₂ reached the thermodynamic equilibrium with the coexistence of ZnO and SnO₂. (transition 1a) On the other hand, the GGA calculation at zero pressure in figure 3.6.b calculated that the transition 1a would occur at much lower temperature of 1040 K. Overall, the *ZTO214* is stable at high temperature.

Figure 3.6.c and figure 3.6.d show the pressure effects on the Gibbs energy as a function of temperature *for the ZTO113 composition* by the LDA calculations. 4 GPa in figure 3.6.c and 8 GPa in figure 3.6.d were selected to show the transition 1 and 2. Figure 3.6.c shows the coexistence of *tetra-ZTO214* and SnO₂ is the most stable at all temperature regions at 4 GPa.

However, the Gibbs energy of *LN-ZTO113* drastically decreased and became comparable to those of the other phases. As figure 3.6.d shows, *LN-ZTO113* is the most stable in all the temperature range at 8 GPa, which agrees with the experimental observation that it is the high-pressure phase. [25]

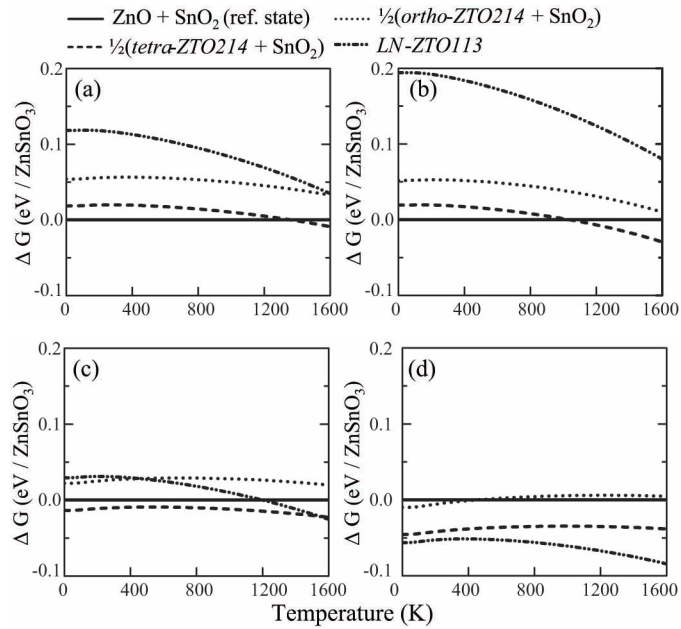


Figure 3.6 Gibbs free energy of various phases as a function of temperature at the *ZTO113* composition by (a) LDA at $p = 0$. (b) GGA at $p = 0$. (c) LDA at $p = 4$ GPa. (d) LDA at $p = 8$ GPa.

3.4.4. P-T phase diagram

Figure 3.7.a and figure 3.7.b show the phase diagrams of pressure and temperature obtained by the LDA and GGA calculations at *the ZTO113 composition*. The thermodynamic stable regions of the coexistence of ZnO and SnO₂, the coexistence of *tetra-ZTO214* and SnO₂, and *LN-ZTO113* phases were represented, respectively. Phase boundaries of the transition 1 and the transition 2 are drawn by solid line and dashed line, respectively. The region of the coexistence of *tetra-ZTO214* and SnO₂ is larger by the GGA calculations than the LDA calculations. At 0 K, the transition 1a occurs at 2.3 GPa by the LDA calculation and at 2.4 GPa by the GGA calculation, respectively. The transition pressure was about 0.8 GPa lower than calculated from enthalpy. This difference comes from the temperature-free term, $1/2kw(k)$, expressed as the first term in equation 3.1. The p-T phase diagram shows the transition pressure of the transition 1 decreased as the temperature increases.

At 0K, the transition 2 was calculated to occur at 7.3 GPa by LDA and at 11.7 GPa by GGA calculations, respectively. Like the transition 1a, the transition pressure evaluated from enthalpy was a little higher than that from Gibbs energy. The transition pressure also decreases as the temperature increases. The synthesis condition of *LN-ZTO113* [25] was represented as a triangle in Fig. 3.7 The LDA results in Figure 3.7.a agree with this

experimental observation that LN-ZTO113 was synthesized at 7 GPa and 1273 K and was not synthesized at lower pressure of 5 GPa [25]. However, the GGA results in figure 3.7.b overestimated the transition pressure and temperature and disagreed with the experimental observations.

Figure 3.7.c shows the p-T phase diagram of *ZTO113 composition* when the *ortho-ZTO214* is considered with ignoring the existence of *tetra-ZTO214*. As fig. 6 shows, the Gibbs energy of *ortho-ZTO214* was about 0.05 eV/f.u. higher than that of *tetra-ZTO214*. As a result, the coexistence region of ZTO214 and SnO₂ does not appear and the phase boundary between the coexistence of ZnO and SnO₂ and the *LN-ZTO113* phase is shown in the p-T phase diagram. In the GGA calculations, the coexistence of ZTO214 and SnO₂ was represented as very narrow region at about 8 GPa.

Figure 3.7.d shows the p-T phase diagram of the *ZTO214 composition* using the LDA functional. The thermodynamic stable regions of the coexistence of ZnO and SnO₂, *tetra-ZTO214*, and *LN-ZTO113* phases were represented, respectively. From the transition 1b, we already discussed the thermodynamic stability of *ZTO214*, which turns out to be the high temperature or high pressure phase. The single phase of *ZTO214* reported by phase diagrams [71-72] is shown as an inverted triangle in figure 3.7.d and it agreed with this p-T phase diagram. The transition 3 can predict the thermodynamic stability of *LN-ZTO113* at the *ZTO214 composition*. *LN-ZTO113* can exist at higher pressure at the *ZTO214 composition* than at

ZTO113 composition, suggesting the synthesis pressure should be increased at the *ZTO214* condition. The GGA calculations were not investigated at the *ZTO214 composition* because the transition 1b is identical as the transition 1a at the *ZTO113 composition* and the region of *LN-ZTO113* and ZnO did not appear for the examined pressure and temperature range.

The reverse transition at the same pressure was ignored because the differences were too small to have the value under 10^{-5} eV/f.u. It's because the heat capacity at constant pressure, C_p ($=dG/dT$) of the coexistence of ZnO and SnO₂ was larger than the coexistence of *ZTO214* and SnO₂ up to about 100~150 K. So, at 0K the half of *ZTO214* and SnO₂ is the most stable phase, and when the temperature increases, the coexistence of ZnO and SnO₂ becomes the most stable phase reversely. The sudden steep decreases of transition temperature to 0K were shown on the p-T phase diagram. However, it is not meaningful because the solid-solid phase transition lines do not guarantee the real occurrence of phase transformation. In addition, the solid-solid phase transition line can be changed according to the space group of unitcell of inverse spinel *ZTO214*.

In general, this thermodynamic transition agrees with the experimental data. Considering the transition 1, 2 and 3, *tetra-ZTO214* can form at the same pressure and temperature for both the *ZTO113 composition* and the *ZTO214 composition*. The ZnO-SnO₂ amorphous film is found under the crystallization temperature that is reported as about 900 K. [23,26,28] At

zero-pressure and low temperature, our calculations describe the real system well that the most stable phase is coexistent of ZnO and SnO₂. Due to amorphous system, the local atomic structure is also randomized. Over the crystallization temperature, the amorphous system becomes the crystalline system. When *ZTO214* is treated as *tetra-ZTO214*, the transition temperature is a little higher than the crystallization temperature. Over the transition temperature, the coexistence of *ZTO214* and SnO₂ become more stable than coexistent of ZnO and SnO₂.

For the *ZTO113* composition, Inaguma *et al.* reported that *LN-ZTO113* turns into the coexistence of *ZTO214* and SnO₂ over 1073 K. [25] Because *LN-ZTO113* is stable at higher pressure, it can be guessed to occur the phase transformation to a more stable phase at zero pressure. In addition, the previous experimental study reported that metastable *IL-ZTO113* film is decomposed into the coexistence of *ZTO214* and SnO₂ over about 873 K. [94] The metastable bulk *IL-ZTO113* is also decomposed into the coexistence of *ZTO214* and SnO₂ over about 1273 K by the paper which reported the ion-exchange synthesis method. [18] In addition, for the *ZTO214* composition, Wang *et al.* reported the coexistence of ZnO and SnO₂ gradually changes into *ZTO214* at about 1000 K and finally it disappears at 1200 K as the temperature increases. [49, 50] The difference between calculated and the experimental transition temperatures can be attributed to several factors. One is that the thermodynamic calculations by *ab-initio*

method cannot guarantee the occurrence of transformation due to the activation barrier for the kinetics to take place. Another factor is that the experimental data were almost obtained from thin films, whose structures were amorphous in most cases. During crystallization, they are under the biaxial compressive or tensile stress depending on the mismatch of both the lattice parameter and the thermal expansion with the substrates.

However, the thermodynamic stability region can change according to the composition. Even in real materials, the distribution of Zn and Sn at octahedral sites is randomized with treating as the same site and *ZTO214* is called as disordered inverse spinel. [70] Considering figure 3.7.a and figure 3.7.c, *ZTO214* can be concluded as the stable phase or not depending on the distribution of Zn and Sn. In fact, Hoel reported the coexistence of polycrystalline film composed of *ZTO214*, ZnO and SnO₂ when zinc tin oxide film formed at high temperature. [95] It seems to be plausible that the local atomic structure of the *ZTO214* in the film varies, such as the inverse spinel phases belonging to the space group P4₁22, Imma, P1, due to the numerous degree of freedom to occupy the octahedral sites by Zn and Sn .

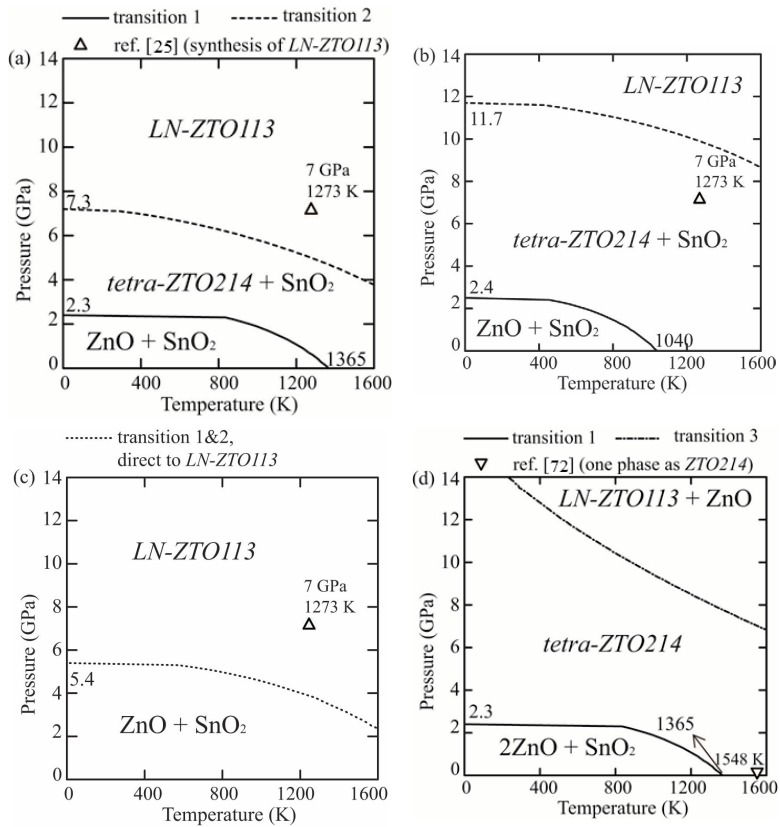


Figure 3.7 P-T phase diagrams for the (a) ZTO113 composition using LDA (b) ZTO113 composition using GGA (c) ZTO113 composition using LDA by considering only *ortho*-ZTO214 instead of *tetra*-ZTO214 and (d) ZTO214 composition using LDA functionals.

3.4.5. DFT+U method

The xc-functional of the DFT+U method [63] was also tested. However, it was not helpful for the thermodynamic calculation of zinc tin oxide systems. When LDA+U scheme was used, all the volume of zinc tin oxide phases slightly decreased. It means the differences of the bond lengths and the cell volume between the calculated and experimental values get larger. Because the bond lengths are related to the phonon vibrations, LDA+U scheme was not performed. When the GGA+U scheme was used, on the contrary, the volume gets closer to the experimental value. However, at zero pressure, the transition 1 of temperature was 1340 K which is about 300 K higher than that from GGA scheme. The failure in describing the tensile region of *IL-ZTO113* was still remained as the GGA calculation. In addition, the pressure of transition 1 was about 6 GPa which is much higher than GGA calculation. The transition 2 did not occur in the range of 0 to 14 GPa and failed to describe the synthesis condition of *LN-ZTO113*.

3.4.6. Cation diordering

Inverse spinels are reported to have the cation disordering for octahedral sites in high temperatures. Seko *et al.*, reported that Mg_2TiO_4 and Zn_2TiO_4 exhibit cation ordering with the space group of $P4_122$. [70] However, no informations about *ZTO214* are reported. Disordered inverse spinel *ZTO214* (*DIS-ZTO214*) include the cation disordering. The space group is $Fd-3m$ in macro scale. In this case, considering the Gibbs energy, the configurational energy is added to the Gibbs energy. So the equation 3.5 becomes equation 3.6.

$$G(p,T) = \min_V [E(V) + pV + F_{vib}(V,T) + F_{conf}(V,T)] \quad (3.6)$$

Confugrational energy can be defined as

$$F_{conf} = -k_B T [x \ln x + (1-x) \ln(1-x) + x \ln \frac{x}{2} + (2-x) \ln(1 - \frac{x}{2})] \quad (3.7)$$

where x is the inversion ratio. The x changes in the range between zero and one. When the value is zero and one, it means the normal spinel and inverse spinel, respectively.

Describing the cation disordering in atomic scale is difficult. In this chapter, the six calculations were performed with generating the random number for occupancies of Zn and Sn for the octahedral sites. They all showed different *mono-ZTO214s*. The energies, volumes, vibrational properties of *tetra-ZTO214* and *ortho-ZTO214* were added and averaged to represent *DIS-ZTO214* among eight results.

Figure 3.8.a show the comparison of the system energy of electronic energy at 0K. Ordered inverse spinel *ZTO214* (*OIS-ZTO214*) was selected as *tetra-ZTO214* which showed the minimum energy among various cells of *ZTO214*. By averaging including several different cells of *mono-ZTO214*, the system energy becomes higher. Figure 3.8.b shows the differences of Helmholtz free energy between *OIS-ZTO214* and *DIS-ZTO214*. The configurational energy F_{conf} is only involved for *DIS-ZTO214*. At low temperature, the differences of free energy between *OIS-ZTO214* and *DIS-ZTO214* are ignorable. However, at high temperature, the differences of free energy become larger. At 1000K, the energy about 0.1 eV/f.u. is gained by cation diordering.

Figure 3.9.a and 3.9.b show the p-T phase diagram for *ZTO113* composition and *ZTO214* composition using *DIS-ZTO214* and LDA-CA for *ZTO214* cell and xc-functional. At zero temperature, the phase transition occurred from the coexistence of ZnO and SnO₂ to *LN-ZTO113* directly by pressurization. At zero pressure, the phase transition temperature from the coexistence of ZnO and SnO₂ to *DIS-ZTO214* decreased as the value of about 1000 K. These changes are meaningful considering the results of figure 3.8.a and 3.8.b. However, the conclusion that the high pressure phase and high temperature phases are *LN-ZTO113* and *ZTO214* is not changed by cation disordering.

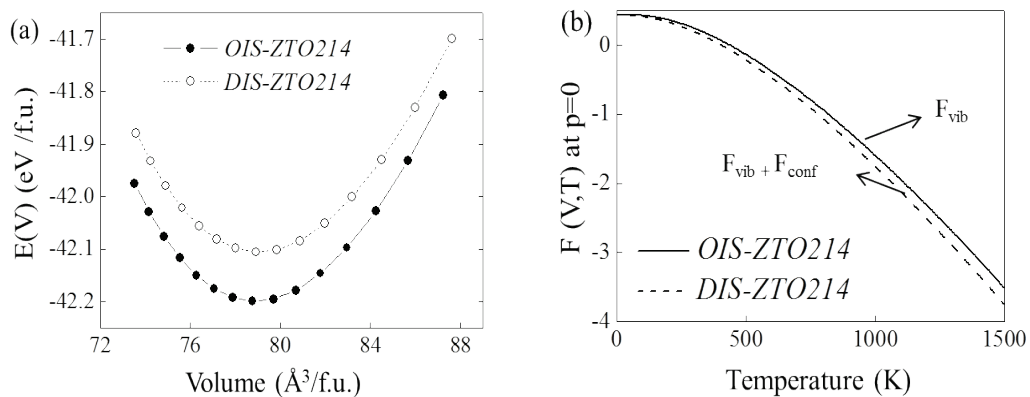


Figure 3.8 Comparison of ordered inverse spinel *ZTO214* and disordered inverse spinel *ZTO214*. (a) Energy of electronic structure at 0K. (b) Helmholtz free energy $F(V, T)$ at $p=0$.

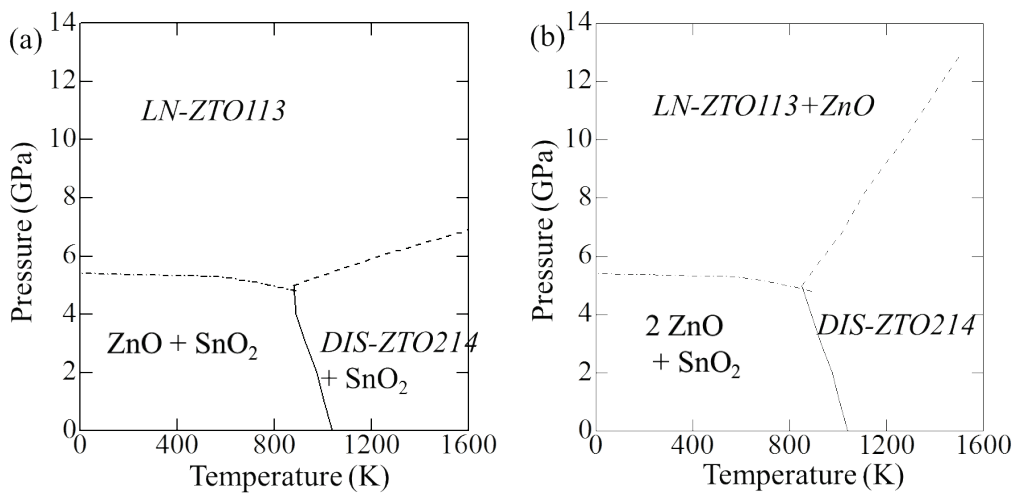


Figure 3.9 P-T phase diagrams for the (a) *ZTO113* composition. (b) *ZTO214* composition using disordered inverse spinel *ZTO214* (DIS-ZTO214).

3.4.7. Zn-O bond changes by pressurization

According to Pauling's rules, the ratio of radii of cations and anions dominates the preference of the coordination of cations. [97] Sn^{4+} is large enough to fill the octahedral sites surrounded by oxygen atoms to make SnO_6 unit in rutile phase of SnO_2 . Zn^{2+} is also large enough to fill the octahedral sites around oxygen atoms to make ZnO_6 unit, however, due to its partial sp^3 covalent bonding nature, Zn prefer to occupy the tetrahedral sites. [36] As the hydrostatic compression increases, the coordination number (CN) of Zn in ZnO increases sequentially from four to six then to eight with the changes of the stable phase from wurtzite to rocksalt and then to cesium chloride phase. [80]

Similarly, in zinc tin oxide phases, the increasing tendency of the CN of the cations as the pressure is the same as the binary oxides. In *ZTO214*, an half of Zn atoms occupy the tetrahedral sites and the other half of them occupies the octahedral sites. In the higher pressure phase, *LN-ZTO113*, on the other hand, the whole Zn atoms occupy the octahedral sites. Table 3.2 shows the bond length and the CN of each phase. The bond length of Sn-O in the various phases is almost similar with each other and the CN is kept as six. However, the bond length of Zn-O increases with the increase of CN by pressurization. It means the external pressure mainly affects Zn-O

bonds more than Sn-O bonds. This can be inferred from the higher bulk modulus of SnO₂ is than ZnO in table 2.3. [79, 81]

Table 3.2 Bond length and coordination number of cations in oxide phases.

Composition	Space group	xc-functionals	Bonding length of Zn-O (Å)	CN of Zn	Bonding length of Sn-O (Å)	CN of Sn
ZnO	P6 ₃ mc	LDA ^a	4×1.951 (±0.003)	4	-	-
		GGA ^b	4×2.008 (±0.004)			
SnO ₂	P4 ₂ /mnm	LDA	-	-	6×2.052 (±0.006)	6
		GGA	-		6×2.093 (±0.001)	
ZnSnO ₃	R3c (LN-)	LDA	3×1.97, 3×2.29	6	3×2.03, 3× 2.09	6
		GGA	3×2.03, 3×2.35		3×2.07, 3× 2.13	
Zn ₂ SnO ₄	P4 ₁ 22 (tetra-)	LDA	2×1.95, 2× 1.99	4	2×2.03, 2× 2.07, 2×2.10	6
			2×2.03, 2× 2.08, 2×2.19	6		
		GGA	2×2.01, 2× 2.05	4	2×2.06 2× 2.11, 2×2.14	6
			2×2.08, 2× 2.15, 2×2.25	6		

^aLDA parameterized by Ceperley *et al.*[54], ^bGGA Parameterized by Perdew *et al.*[56],

3.5. Summary

The thermodynamic stability of various phases of zinc tin oxides by *ab-initio* calculations including the phonon properties was investigated. In the result, at zero pressure and temperature, the coexistence of ZnO and SnO₂ was the most stable phase. The coexistence state was obtained by the summation of energy and volume at the same applied external pressure. The LDA and GGA of exchange-correlation functionals were used and LDA describes the result better by considering the bulk modulus and optimized volume, the transition pressure and temperature result compared to the real experimental reports. Considering the phonon properties, at zero-pressure over about 1300 K of temperature, *ZTO214* and SnO₂ got more stable than the ground state with reflecting the previous experimental reports. Pressure-temperature phase diagram for the *ZTO113* composition was obtained and the transition of pressure and temperature was obtained well compared to the synthesis pressure and temperature of *LN-ZTO113* and the existence conditions of *ZTO214*. For the *ZTO214* composition, *LN-ZTO113* can be obtained by high pressure, which is much higher than *ZTO113* composition.

Pressurization considering only enthalpy was also considered to compare with the previous reports. It changed the thermodynamic stability like the following sequence : the coexistence of ZnO and SnO₂ to the half of *ZTO214* and SnO₂, to *LN-ZTO113*. *IL-ZTO113* was unstable phase

considering the energetics and phonon frequency. The different of space group selection of *ZTO214* and exchange-correlation functionals were the reasons the previous reports are different each other. Hydrostatic compression affected Zn-O bonds more than Sn-O bonds.

Chapter 4. Point defects in inverse spinel Zn_2SnO_4

4.1. Overview

Without any doping, transparent oxide semiconductors such as ZnO have the natural n-type conductivity, so oxygen vacancy has been treated as carrier generators. Because most of oxide semiconductors are thought as O-deficient, n-type doping nature is from the doubly charged vacancy of oxygen. However, first-principles calculations confirmed that intrinsic defects such as oxygen vacancies do not generate any electrons in ZnO. [29-31]

Transparent conducting oxides which are mainly used as the electrode with higher electronic concentration, such as In_2O_3 and SnO_2 have also similar issue. The behaviors of oxygen vacancy of In_2O_3 and SnO_2 and the compound oxide of IGZO have been discussed that they are deep state or shallow electron donors, [29-35,67-68]

If the oxygen vacancy makes the deep state, it can be one of the candidates of source of photocurrent. [31, 45] MOSFETS with the channel layer of Zn-based oxides semiconductors have the problem the instability with illuminations of visible lights. [39-41] When the visible lights come into the devices, the devices are turned on at the negative bias. The threshold voltage shifts to negative bias. It means the electrons occupied at the deep

oxygen state can be excited to the conduction band with the ionization of oxygen vacancy. However, if the oxygen vacancies make the shallow state, they can generate the carrier sources with forming n-type (semi-)conductor.

One of another candidate of the electron source is hydrogen. Hydrogens are ubiquitous as the gas state of H_2O and difficult to control. The detection of hydrogen by the experiments is also difficult. Van de Walle reported hydrogen can be donor as H^+ state and acceptor as H^- state. [115] In GaN, H^+ is stable at the p-type region with generating the electron and H^- is stable at the n-type region with generating the hole. Meanwhile, in ZnO, H^+ is stable in whole bandgap region. [114-115]

The role of point defects using the first-principles calculations were not performed yet to ZTO system. In addition, those properties are related to the bandgap. In this chapter, the behavior of oxygen vacancies and hydrogen interstitials were investigated in *ZTO214* phase which was the most stable phase in ternary system with the calculations of formation energy with corrections and electronic structures using the hybrid density functional such as HSE06. [65]

4.2. Formation energy calculations of point defects

4.2.1. The definition of formation energy

The concentration of defect can be defined as

$$c = N_{sites} \exp\left(-\frac{E^f}{k_B T}\right) \quad (4.1)$$

where N_{sites} is the number of sites in the unitcell, total energy of supercell with oxygen vacancy, [98] N_{sites} is pre-exponential factor, so the formation of defect dominates the concentration of defects. Low formation energy of defect means the higher concentration of defects. Temperature is defined as the forming condition of the materials.

The formation energy of defect can be defined as by equation 4.2 expressed as,

$$E^f(D^q; \mu_x, E_F) = E_{tot}(D^q) - E(bulk) - \sum_x \Delta n_x \mu_x + q(E_{VBM} + E_F + \Delta E_{PA}) + \Delta E_{corr} \quad (4.2)$$

where $E_{tot}(D^q)$ is the total energy of supercell with oxygen vacancy, $E_{tot}(Zn_2SnO_4)$ is the total energy of the pure bulk, Δn_x is the change the number of atom by defect, μ_x is the chemical potential, E_F is the Fermi level referenced to the valence band maximum, E_{VBM} and ΔE_{PA} is the alignment of the electrostatic potentials between the farthest region in the

supercell with defect and the perfect supercell.as, ΔE_{corr} is the correction of image charge induced by small size of supercell.

$$E^f(V_O) = E_{tot}(Zn_2SnO_4 + V_O) - E_{tot}(Zn_2SnO_4) + \mu_O + q(E_F + E_{VBM} + \Delta E_{PE}) + \Delta E_{corr} \quad (4.3)$$

where $E_{tot}(Zn_2SnO_4 + V_O)$ is the total energy of supercells with oxygen vacancy, $E_{tot}(Zn_2SnO_4)$ is the total energy of the pure *ZTO214*, μ_O is the chemical potential which is defined as the half energy of O_2 because O-rich condition was used. When the potential defect is involved in the reservoir, the electrostatic potentials shift to opposite value in order to the compensation of defects. So the potential align should be performed to erase the effects of electrostatic shifts.

4.2.2. The correction of underestimated bandgaps

As mentioned at chapter 1, the conventional DFT of LDA and GGA induce the underestimation of bandgap. As table 2.4 shows, optimized HSE06 based on hybrid density functional can induce the same bandgap (3.6 eV) of experimental value.

4.2.3. The correction of image charge interactions

The distances between the supercells are not large enough to erase the Coulombic interactions between the charge defects. Leslei *et al.*, proposed the Madelung energy which is the first term of equation 4.4. It means the interactions the monopoles. Makov and Payne proposed additional interactions related quadrupole term. [99-100]

$$E_{corr} = \frac{q^2 \alpha}{2\epsilon L} - \frac{2\pi q Q}{3\epsilon L^3} \quad (4.4)$$

Lany and Zunger pointed out that Makov's correction overestimates the formation energy of charged defects. They proposed that effective prefactor of 0.65 should be multiply by Makov's E_{corr} and the alignment of electrostatic potentials. [101-102]

4.3. Computational methods

Calculations were performed with a plane-wave code, VASP code based on the *ab-initio* calculations with an energy cutoff of 500 eV. [58-59] All the calculations were performed based on the generalized gradient approximation (GGA) proposed by Perdew-Burke-Ernzerhof (PBE). [57] 3d and 4d orbitals in Zn and Sn were also treated as the source of valence electrons. For band-gap correction, the on-site effective Coulomb interactions as given GGA+U and the screened hybrid functional method proposed by Heyd-Scuseria-Ernzerhof were used as the exchange-correlation functionals with the mixing ratio of 29 %. [65] It showed the bandgap of 3.6 eV which is the same as the experimental bandgap. U_{eff} value was used 7.5 eV for Zn and 3.5 eV for Sn from the previous reports of binary oxides. [67-68] The lattice parameters and interatomic coordinates were determined as the primitive cell of *ZTO214* with the space group of $P4_122$ which show the minimum energy among various *ZTO214* cells. [70] For the correction for the charged vacancy which generates cell-cell Coulombic interactions, the first term of Makov-Payne (MP) correction [100] and Lany-Zunger (LZ) [101-102] corrections were also obtained. For the calculation of a vacancy, the supercells with 28, 56, 112, 224 and 448 atoms for GGA+U were used. After the correction of cell-cell Coulombic interactions, they were fitted for the variable of L^{-1} and L^{-3} . 112 atoms for optimized HSE06

(opt-HSE06) were used after finding the image correction result. Odd charged vacancy was calculated with spin-polarized method. Static dielectric constants were obtained as the value of 10.0 from DFPT using opt-HSE. This value is similar as that of other xc-functional, which is shown as the table 4.1.

According to various exchange-correlations functionals, the direct bandgaps at Γ is obtained in table 2.4. Due to the underestimation of 30 % of bandgap and the result of transition state $\epsilon(2+/0)$ over CVB, it is concluded that the basis of GGA calculations can falsely describe the result. For the correction of underestimation of bandgap, optimized HSE06 (opt-HSE06) [65] was obtained.

Table 4.1 Static dielectric constants from various xc-functionals

xc-functional	28 atoms	56 atoms	112 atoms
LDA	-	-	10.84
PBE	11.50	12.07	11.99
PBE+U	10.59	10.90	10.87
Opt-HSE06	9.69	9.69	-

4.4. Formation of oxygen vacancy

4.4.1. Image correction result using GGA+U scheme

For site of oxygen vacancy, O-I, which is neighbored to 3 Zn and Sn, and O-II, which is neighbored to 2 Zn and 2 Sn were chosen. Table 4.2 shows the neutral vacancy formation energy according to various xc-functionals at O-rich condition by equation 4.2.

Figure 4.1 shows the formation energy of charged vacancies using GGA+U with corrections of image charge interactions between the supercells. NA, PA, MP, MPPA and LZ indicates the result without any correction, potential align, ΔV_{PE} , Makov-Payne [99-100], Makov-Payne with potential align and Lany-Zunger correction [101-102], respectively. After the correction of five methods in each supercells, the formation energies were fitted to the function of $L^{-1} + L^{-3}$. Zero value of L^{-1} means the infinite supercell. In the result, the deviations of fitted values were in the range of 0.1 eV. In those, the fitted value after LZ correction was the middle value.

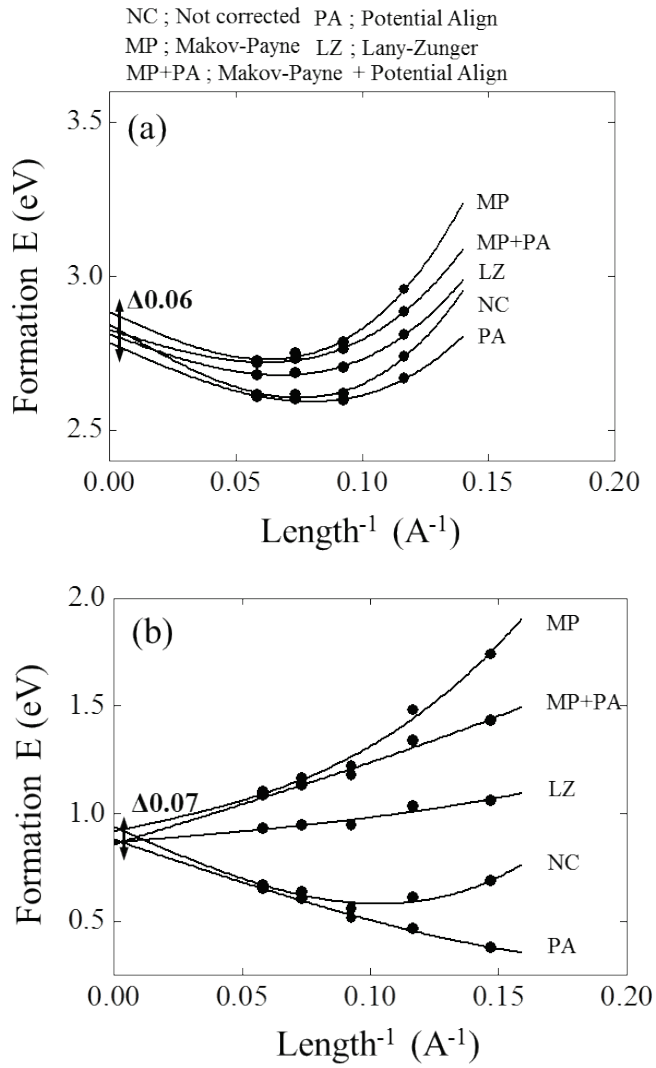


Figure 4.1 Image corrections for charged vacancy. (a) V_O^+ using GGA+U. (b) V_O^{2+} using GGA+U.

Table 4.2 Neutral vacancy formation energy of *ZTO214* according to various xc-functionals

xc-functional	supercell	O-I	O-II
		(3 Zn, 1 Sn)	(2 Zn, 2 Sn)
PBE	448 atoms	3.61	3.87
PBE+U	448 atoms	4.35	4.55
Opt-HSE06	112 atoms	4.18	4.50

4.4.2. Formation energy of oxygen vacancy

The LZ correction was also obtained to the result from opt-HSE06. Figure 4.2 shows the formation energy of oxygen vacancy as the variable of Fermi level, E_F . The formation energies of oxygen at O-I site and O-II site are drawn. As table 4.2 mentions, the formation energy of oxygen at O-I site is lower than that from O-II site. Oxygen vacancy in *ZTO214* also show the negative U like ZnO, the transition state, $\epsilon(+2/0)$ were from the valence band maximum, respectively. The location of transition states, $\epsilon(+2/0)$ from O-I and O-II sites were almost the same. Because *ZTO214* has the n-type conductivity, the Fermi level will be near the conduction band minimum (CBM). At this region, oxygen vacancy is neutral. Similarly as ZnO, the thermodynamic stable state is neutral state without generating two electrons. [29] It means oxygen vacancy does not have the role of the source of electrons.

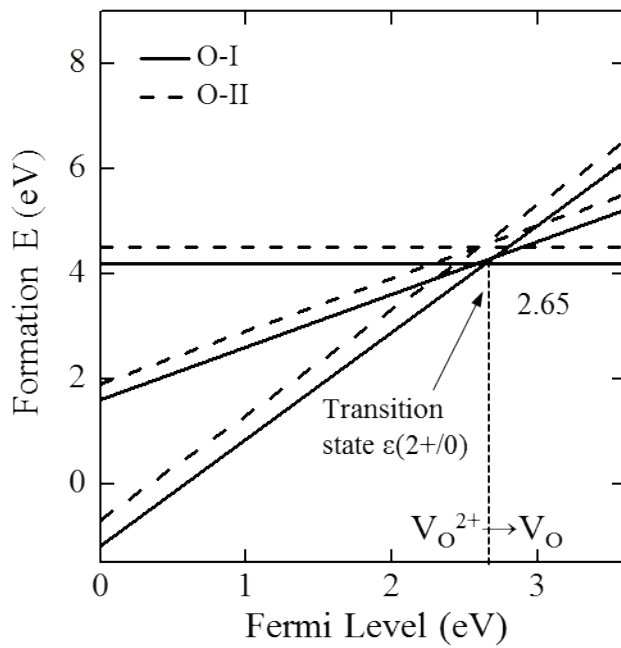


Figure 4.2 Oxygen vacancy formation energies using opt-HSE06 with LZ correction.

4.4.3. Electronic structures

Figure 4.3 shows the electronic structure of *ZTO214* with oxygen vacancy using opt-HSE06. Figure 4.3.a shows the electronic structure of pure *ZTO214* for the reference state. Oxygen at the O-I site was selected.

When the neutral oxygen vacancy forms, very deep state occurs at the middle location in the bandgap shown as figure 4.3.b. The deviation according to the change of k-space is small as under 0.1 eV. It means the neutral oxygen vacancy forms the deep localized state. Two electrons are occupied at the state.

Figure 4.3.c and figure 4.3.d show the electronic structures of *ZTO214* with the singly charged vacancy. When the singly charged vacancy forms (figure 4.3.c), the band is splitted to up-spin and down-spin state. In up-spin band diagram, one electron is occupied at the deep state in the bandgap like neutral oxygen vacancy. Meanwhile, the unoccupied conduction-band like state occurs in down-spin band diagram (figure 4.3.d),

Figure 4.5.e shows the electronic structures of *ZTO214* with the doubly charged vacancy. Similarly the down-spin band diagram from the singly charged vacancy, the unoccupied conduction-band like state occurs.

The single particle energies which are generated states by oxygen vacancies from optimized HSE06 with the relaxed and unrelaxed positions were obtained at figure 4.4. The states were counted at the Γ -point.

According to Lany *et al.*, as the sizes of supercell become larger and the interactions between the defect states decreases, the Brillouin zone averaged values tend to be converged to the value at the gamma point. [101] When the structures are not relaxed, the states generated by oxygen vacancies are at the middle points in the band gap.

After the relaxation of structure, the locations of states changed according to the optimum configurations. Neutral oxygen vacancy at O-I site is conserved as the deep state after the relaxations of the structure. The state is located at 1.52 eV over VBM. Vacancy at the O-II site has also similar positions as the value of 1.66 eV over VBM. The generated state by single charged oxygen vacancy have higher defect with splitting to occupied and unoccupied states. However, this charged vacancy was unstable at whole bandgap. The doubly charged vacancies have the states near CBM with showing the shallow state. When they are counted at the Γ -point, the locations are below about 0.5 eV below the CBM. However, the locations are over about 0.2 ~ 0.3 eV over the CBM when it is averaged at the 2^3 MP points. They form shallow or resonance states with the de-localizations with generating two electrons to the conduction band. This V_O^{2+} state is stable when the Fermi level is at the range near VBM to middle point. So the behavior of p-type dopant killer can be suggested it can be suggested when the materials is doped with p-type dopants and Fermi level go under the transition state ($e2+/0$). [103]

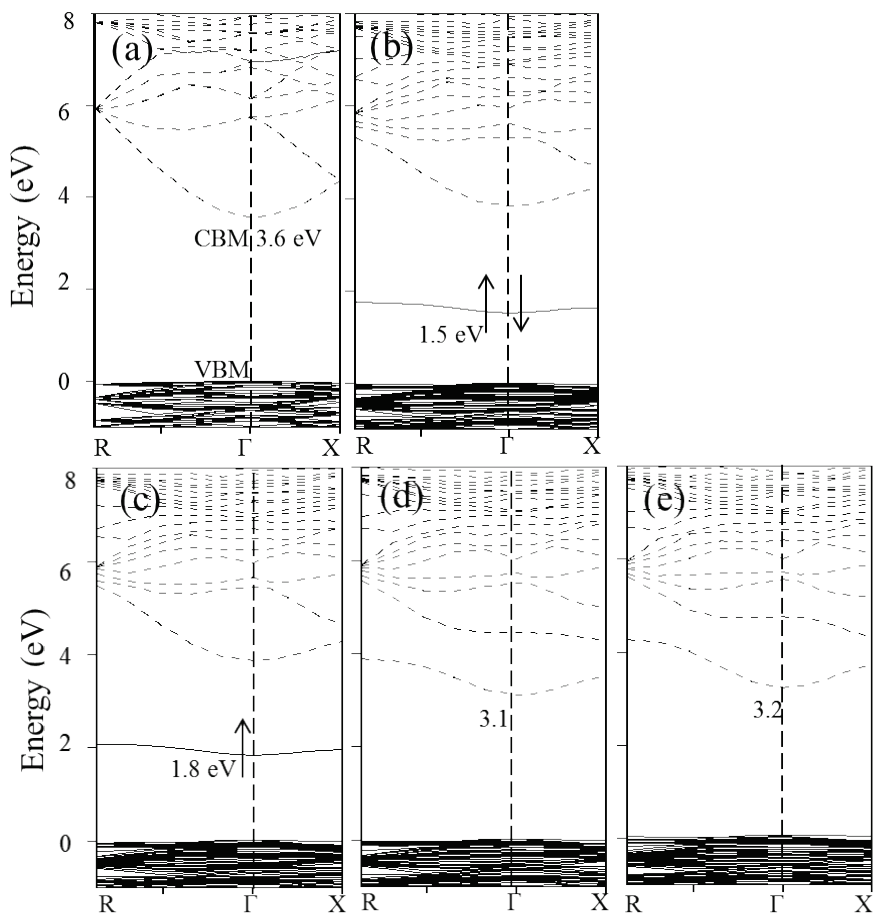


Figure 4.3 Electronic structures of *ZTO214* with oxygen vacancy at O-I site using opt-HSE06. (a) no vacancy. (b) V_{O}^0 . (c) up-spin of V_{O}^+ . (d) down-spin of V_{O}^+ . (e) V_{O}^{2+} .

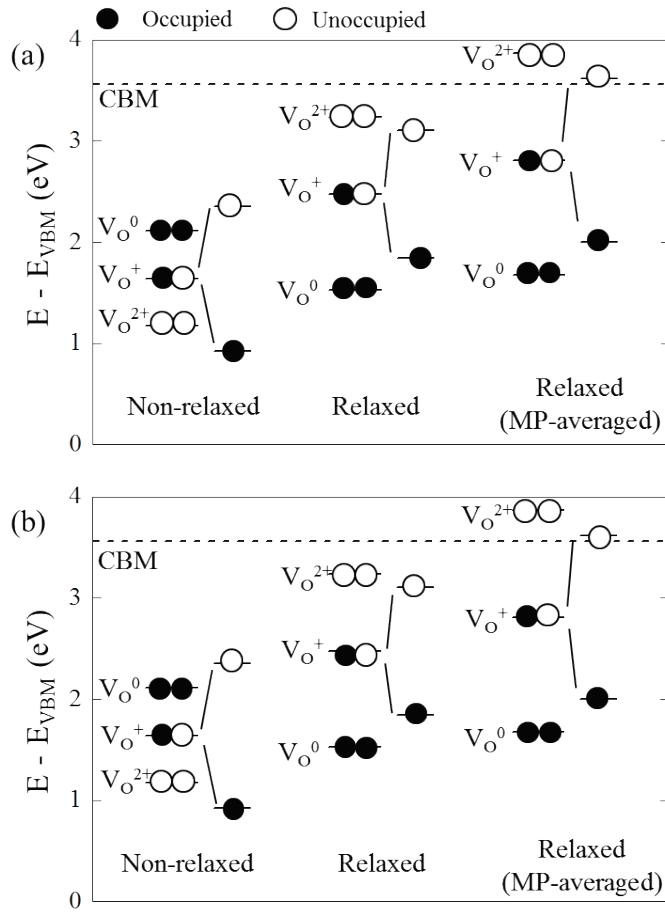


Figure 4.4 Eigenvalues generated by oxygen vacancies between the bandgap in *ZTO214*. The states were defined at the Γ -point and averaged at 2^3 MP points using opt-HSE06, respectively. (a) From O-I site. (b) From O-II site.

4.4.4. Optical ionization energy

When the charges of oxygen vacancy change, the volumes of tetrahedrons formed by four cations are also changed due to the repulsion between the cations. Table 4.3 shows the optimized volume of tetrahedron including the oxygen vacancy surrounded by cations. When the vacancy is neutral, two electrons are occupied with pulling the cations of neighbors. The volume of tetrahedron is conserved or decreased when compared to the pure state. However, the vacancy is singly or doubly charged, the electrons are unoccupied so the volume of tetrahedron increases.

In order to calculate the optical ionization energy by the light, the formation energy according to the structure relaxations was obtained for oxygen vacancy at O-I site by optimized HSE06. Figure 4.5 assumes the condition when the Fermi level is at the conduction band minimum. The y-axis of figure 4.7 means the relative system energy and x-axis means the configuration coordinate which is described as the volume of tetrahedron made by cations. The ionization energy, from V_O to V_O^+ , were obtained as about 1.8 ~ 2.0 eV is in the range of visible lights (1.5 ~ 3.1 eV). After the relaxation of atomic coordination, V_O^+ can be relaxed back to V_O with the emission of light. In ZnO case, this is called as green emission measured by photoluminescence (PL) apparatus. [29,31] The singly charged vacancy can ionized again into V_O^{2+} by the visible light. These values are also about 1.9

eV. It means the thermodynamically stable neutral oxygen vacancies can be ionized with the emitting the electrons and play a role as the defect center of increasing photocurrent.

Table 4.3 The optimized volume of tetrahedron including the oxygen vacancy surrounded by cations.

Volume (\AA^3)				
Xc-functional	GGA+U		HSE	
Site of O	O-I	O-II	O-I	O-II
Unrelaxed	3.93	4.30	4.08	4.41
V_O^0	3.85	4.37	3.91	4.37
V_O^+	4.99	5.27	5.10	5.39
V_O^{2+}	6.05	6.27	6.16	6.42

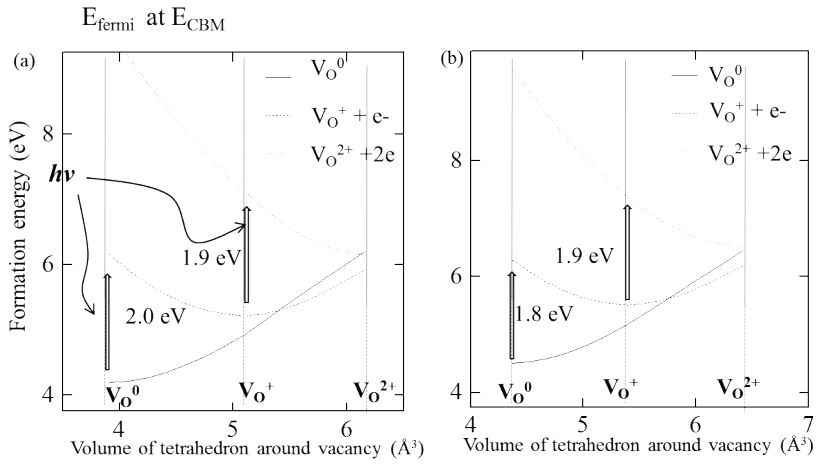


Figure 4.5 Ionization energy of oxygen vacancy by visible light.

From (a) O-I site. (b) O-II site.

4.5. Formation of hydrogen interstitials

4.5.1. Various sites hydrogen incorporated

The radius of hydrogen is smaller than cations and oxygens, so it can be incorporated into various sites such as interstitials. It can be incorporated even at the bond center of oxygen and cations. [114]

The GGA+U scheme was used to find out the most stable sites the hydrogens can be incorporated. Table 4.4 arranges the formation energies according to the initial location that hydrogen atom was inserted. In the result, the middle point of the zinc at octahedral site and the zinc at the tetrahedral site was the most stable initial point. After the relaxation, the hydrogen moves close to the oxygen and attached with forming O-H bonds shown as figure 4.7.

Table 4.4 The initial position of incorporated hydrogen interstitial and formation energy calculated by GGA+U scheme.

	Initial position of H _i	Formation energy (eV)
Bond centers	O-Zn(tet)	1.87, 1.68
	O-Zn(oct)	1.69, 1.53
	O-Sn	1.66, 1.73, 2.10
Between cations	Zn(oct)-Sn	1.85
	Zn(oct)-Zn(tet)	1.37, 1.40, 1.53
	Sn-Sn	3.46
	Zn(oct)-Zn(oct)	2.63
Between oxygens	O-O	2.11, 3.56

4.5.2. Formation energy of hydrogen interstitials

Figure 4.6 shows the formation energy according to the Fermi level and the charge of hydrogen interstitials. In the whole bandgap region, the hydrogen interstitial was positively charged and no transition state $\epsilon(+/0)$ was found. It means that hydrogen interstitial can be an unintended electron source as the state of $H^+ + e^-$ like ZnO. [114-115]

The formation energy at the p-type region is negative value, so the hydrogen is incorporated spontaneously. In addition, it means that when the p-type dopants were doped, the hydrogen can have a role of p-type dopant killer. [103]

Figure 4.7 shows when the positively charged hydrogen interstitial is incorporated and attached to the oxygen with forming -OH bonds. The bond length is about 1.0 Å and similar to that of the typical O-H bond. Three cations are conserved as the state of forming bonds with the oxygen and the other one is drifted apart from the oxygen.

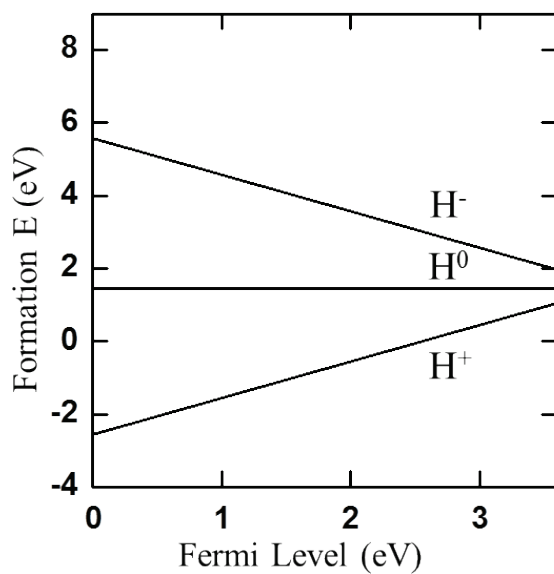


Figure 4.6 Hydrogen interstitial formation energy using opt-HSE06.

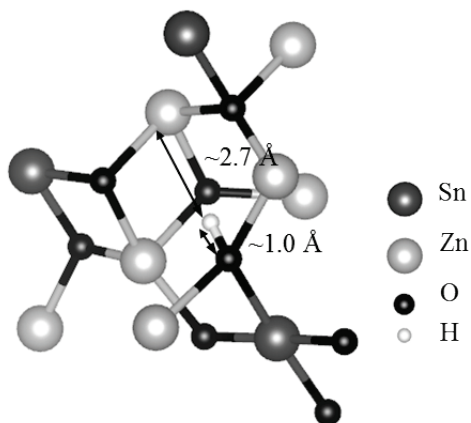


Figure 4.7 The atomic view of incorporated hydrogen interstitial as the state of H^+ and bond with oxygen.

4.5.3. Electronic structures

Figure 4.8 shows the electronic structure of *ZTO214* with the hydrogen interstitials. Figure 4.8.a shows the electronic structure of pure *ZTO214* used as the reference. Figure 4.8.b and 4.8.c show the electronic structure of *ZTO214* with the neutral and positively charged hydrogen interstitial, respectively.

One electron is occupied at the shallow state which is conduction-band like when the hydrogen forms the neutral interstitial. Meanwhile, when the hydrogen interstitial is the positively charged, no occupied states were found in the bandgap. Considering the formation energy calculation result, the electron at the shallow state is extracted to the conduction band with the charging from the neutral state to the positively charged state. It agrees that the hydrogen annealing increases the electron concentration in other TCO such as IGZO and it can be guessed that the hydrogen annealing can also increase the carrier concentration in ZTO system. [47, 112-113].

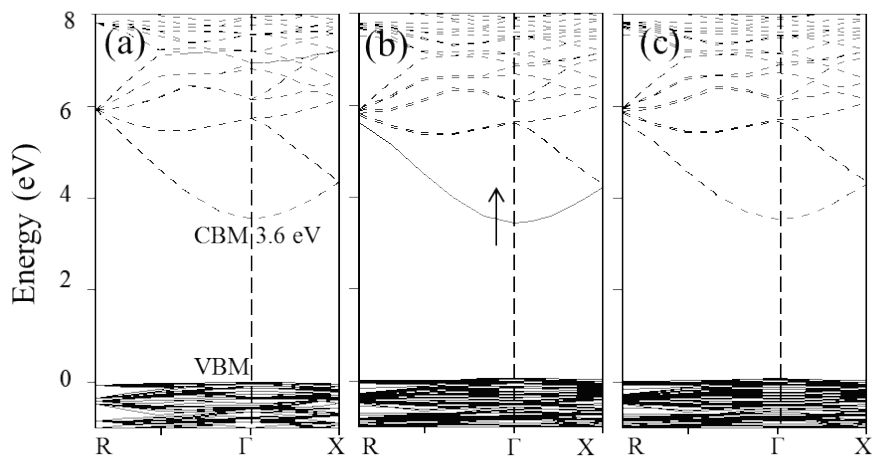


Figure 4.8 Electronic structure of *ZTO214* with the hydrogen interstitial. Solid line and dashed line indicate the occupied and unoccupied bands. (a) Pure *ZTO214*. (b) With H_i^0 . (c) With H_i^+ .

4.6. Summary

The role of point defects such as oxygen vacancy and hydrogen in ZTO system were investigated. The formation energy and electronic structures were analyzed for the stability of defects and locations of state. For the accurate description of bandgap, hybrid density functional theory was used. The exchange ratio of Hartree-Fock of 29 % shows the bandgap of 3.6 eV which is the same bandgap with experimental data. For the additional correction of minimizing the interactions of charged defects across the supercells, several models were tested using GGA+U scheme and Lany-Zunger correction was involved for main calculations.

The formation energy result showed the oxygen vacancy form doubly charged state when the Fermi level is at p-type region, and neutral state when the Fermi level is at n-type region. The transition state $\epsilon(2+/0)$ was about 1 eV below the conduction band and it can be classified to the deep state. The electronic structure showed that deep localized state which is occupied by two electrons are built about 1.5 eV over the VBM when the oxygen vacancy is neutral. When the Fermi level is at the CBM, the ionization energies from V_O^0 to V_O^+ and V_O^+ to V_O^{2+} were calculated about 2 eV with the changing the atomic coordinate. It agrees the experimental reports that about the green lights can generate the photocurrents. [41]

When the hydrogen is incorporated, it always exists as single

charged state. One electron is emitted from the shallow state as the charge of hydrogen changes from neutral state to singly charged state from the electronic structure analysis. Electrons can be generated when the hydrogen is incorporated and hydrogen annealing can be guessed for increasing the carrier concentration.

Chapter 5. Local atomic structure of amorphous phases of zinc tin oxides

5.1. Overview

Amorphous phase films are mainly used for the applications of TFT of display due to low temperature deposition on the glass or polymer substrate. [5] These materials can be used only for the electronic devices such as 3d-memory devices which is not for transparent devices due to higher conductivity than amorphous silicon. [18-19] For the mass-production without the deviations of properties such as mobility between devices, the amorphous state is beneficial in avoiding the ground boundary.

As mentioned at chapter 3, the thermodynamic calculations were performed to compare the thermodynamic stability of phases. However, the the calculations are confined to the crystal phases. In experiments, these materials are mainly used as the amorphous phase, so the investigations of amorphous phases are beneficial.

Melt-quenching method based on *ab-initio* molecular dynamics (*AI*- MD) is useful method to get the amorphous phases. Like GeSbTe (GST) which included the local covalent bondings, various methods are needed to local coordinations can be changed according to the various methods. [105-106] However, due to the ionic bonding nature of TCOs, the ring structures

made by the metal-oxygen are remained. The MQ method based on *ab-initio* calculations was used for getting the amorphous phases. [107] In this chapter, the atomic structures of amorphous phases of widely used compositions, which are *ZTO113* and *ZTO214 compositions*, were investigated. [3]

5.2. Theoretical background

5.2.1. Molecular dynamics (MD)

Molecular dynamics (MD) is a computer simulation method showing the physical movements of atoms and molecules over times governed by Newton's equations. [94,96] The trajectories of atoms and molecules can be defined according to the time scale. If the initial positions and velocities of every atoms and the interatomic potentials are defined, the atoms are under the force derived by the potentials and they moves with the accelerations derived by forces. Then, the velocities and positions of atoms or molecules are changed by accelerations and the interatomic potentials are also changed according to the positions of atoms.

During and after equilibration, various raw data can be stored for each timesteps which include atomic positions and momenta, energies, and forces. From the raw data, many material properties can be obtained such as the basic energetics, structural and mechanical properties, thermal expansion

coefficient, melting point, phase diagram in terms of pressure and volume, defects structure and diffusion, grain boundary, heat capacity and so on.

Interatomic potentials are important because the forces generate atoms to accelerations and velocities, so applying the suitable interatomic potentials is important in order to describe the realistic atomic movements. AI-MD or first-principles molecular dynamics (FP-MD) [111] have an advantage to getting the interatomic potentials from the *ab-initio* calculations including the interactions of electrons. Reversely, the expensive time consumptions and small calculation cells are disadvantages compared to conventional MD.

5.2.2. Melt-quenching method

Amorphous phase is difficult to define, because the word "amorphous" means shapeless state. For this reason, the lattice point of amorphous phase is difficult to define. Melt-quenching method is useful for obtaining the amorphous cell from the initial state of crystalline state.

At melt step, the crystalline memory can be erased because the bonds at the condensed matter are broken due to high temperature. In general, the melting temperatures of TCOs are over about 1800 °C [109, 110], the temperature 2500 °C is enough to break the bonds.

At quenching step, the bonds at the condensed matter can be

regenerated. If the quenching speed is too fast, the unexpected bonds can be generated. [107] However, when the quenching speed is too slow, the efficiency of calculation becomes poor.

5.2.3. Radial distribution function (RDF)

Figure 5.1 shows the schematics of the radial distribution function (RDF). RDF or pair correlation function $g(r)$ is a spherically averaged distribution of interatomic vectors,

$$g_{\alpha\beta}(r) = \frac{1}{\rho^2} \left\langle \sum_i \sum_{i \neq j} \delta(r_i) \delta(r_j - r) \right\rangle \quad (5.1)$$

where ρ is the density. [97,104] Partial radial distribution functions $g_{ab}(r)$ can be calculated by restricting the analysis to the elements a and b. The local structure can also be characterized by the average coordination numbers, which are found by integrating $g_{\alpha\beta}(r)$ to the first minima R_{\min} .

$$n_{\alpha\beta} = \int_0^{R_{\min}} dr 4\pi r^2 \rho_{\alpha\beta}(r) g_{\alpha\beta}(r) \quad (5.2)$$

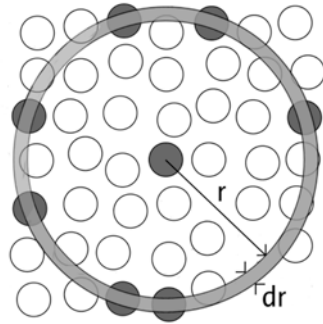


Figure 5.1 Space discretization for the evaluation of the radial distribution function [108]

5.3. Computational Methods

MD simulations were performed based on the density functional theory with VASP code. [58-59] For the MQ steps, the calculation efficiency was considered with pseudo-potential of oxygen with lower cutoff energy of and Γ -only Brillouin zone sampling. For the xc-energies between electrons, the GGA based on the Perdew–Burke–Ernzerhof (PBE) functional [57] is employed. For *ZTO214 composition*, mainly 16-Zn₂SnO₄ was used and the volume and energy per f.u. were almost the same as those of 32-Zn₂SnO₄. For *ZTO113 composition*, 24-ZnSnO₃ was used. The cubic supercell with the volume of 105.26 % (density of 95 %) of crystalline supercells was used.

Figure 5.2 shows the profile of MQ method. During MD simulation, each iteration steps were remained as 2 fs. At the first step of melting, at very high temperature over 5000 K, the bonds of crystalline phase was erased. The erase of bonds were checked by the radial distribution function (RDF). When the crystalline phases are not cubic system, the calculations were performed until the calculation cell becomes cubic with the change of shape and fixed volume step by step. At the second step, at 2500 K which is a little higher temperature over melting temperature, the structure is melted for 10 ps. At third step, the quenching is performed at the speed of 25~100 K/psec. At this step the atomic bonding are formed again. For more efficient

calculations, lower cutoff 300 eV and pseudo-potential of oxygen with lower cutoff of was used with Γ -only Brillouin zone sampling.

At last step, the calculations at zero temperature are performed. The atomic positions, volume and shapes of supercells are relaxed until the Hellmann–Feynman force on each atom is reduced to within 0.03 eV/Å and the external pressure become almost zero. DFT+U method was performed based on the Perdew–Burke–Ernzerhof (PBE) functional to lease the underestimation of bandgap. [57,62-63] For more accurate calculations, higher cutoff 500 eV and pseudo-potential of oxygen with maximum cutoff of was used with 2x2x2 Γ -centered Brillouin zone sampling.

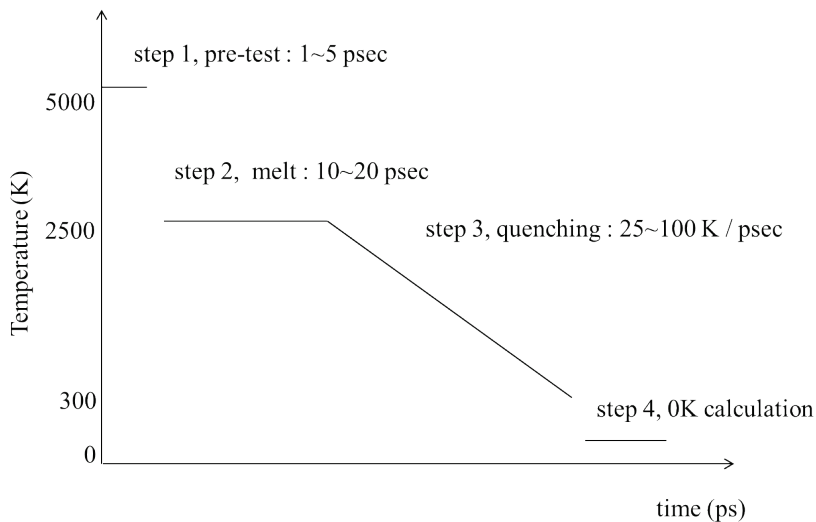


Figure 5.2 Melt-quenching calculation profiles in order to get the amorphous cells using AI-MD.

5.4. Results and discussions

5.4.1. Total energy

For *ZTO214* composition, the crystalline phases of *tetra-ZTO214* and the coexistence of $2 \text{ ZnO} + \text{ SnO}_2$ were used as the references. *ZTO214* which was the most stable ternary oxide and the coexistence of binary oxides were selected as the ground state. For *ZTO113* composition, the crystalline phase of *LN-ZTO113* and the coexistence of $\text{ ZnO} + \text{ SnO}_2$ were used.

Figure 5.3.a and Figure 5.3.b show the energy-volume diagram for *ZTO214* and *ZTO113* compositions, respectively. Among the amorphous phases, the deviation of volume and energy affect by the quenching speed of $25 \sim 100 \text{ K/ps}$ and cell size with the number of $56 \sim 224$ atoms were difficult to find out. However, some samples showed the peroxide bonds (O-O). Walsh *et al.*, reported the fast quenching over 200 K/ps sometimes show the peroxide bonds. [107] According to Cho *et al.*, MD calculations at Baldereschi point can be effective for avoiding forming O-O bonds. [118] This is one of the Frenkel defects, which can be expressed as $(\text{O}_2)_\text{O} + \text{ V}_\text{O}$. Nahm *et al.*, suggested that the peroxide bonds can be one of the candidate of the reason for NBIS. [37] The zero temperature calculations were performed again in order to dissociate the peroxide bonds. When the initial

bond lengths are over about 2.5 Å which is near to the average, the bonds become stable as the dissociated state.

Figure 5.4 shows the polyhedron views of the structure of crystal and amorphous phase for *ZTO214 composition*. The polyhedrons made by cations and oxygens are arranged well. However, the polyhedrons are randomly arranged for amorphous phase. The distortions of local atomic structures of amorphous phase will be discussed using the structural analyses such as RDF.

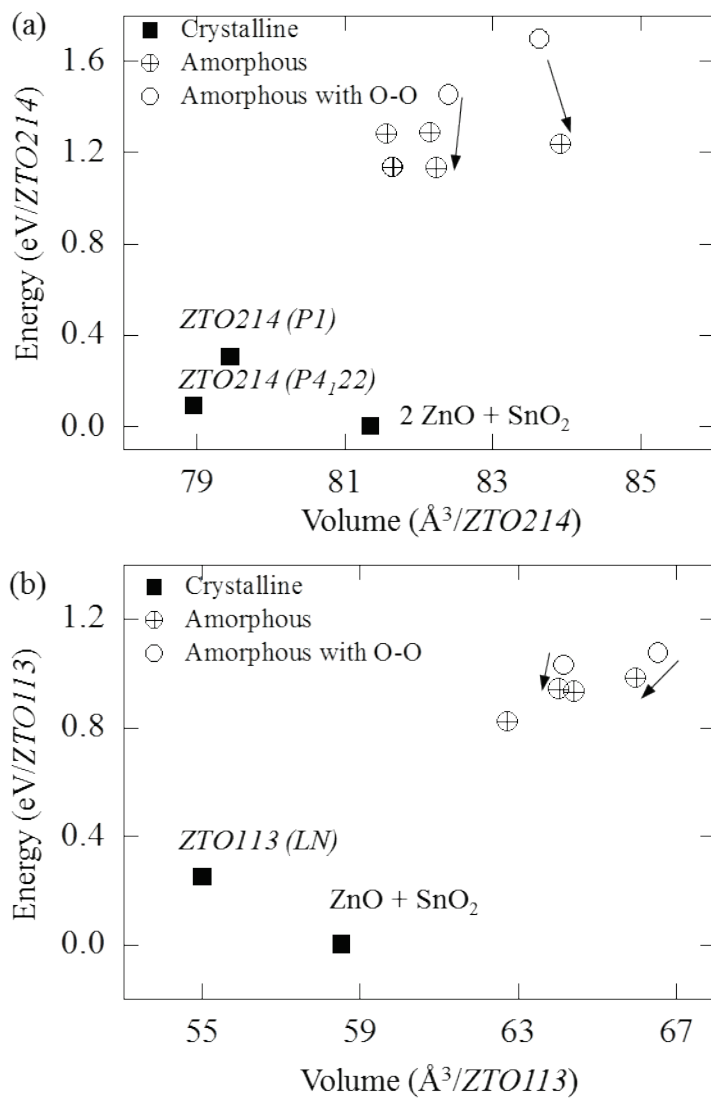


Figure 5.3 Energy-volume diagram of the crystalline and amorphous phases. (a) For *ZTO214* composition. (b) For *ZTO113* composition.

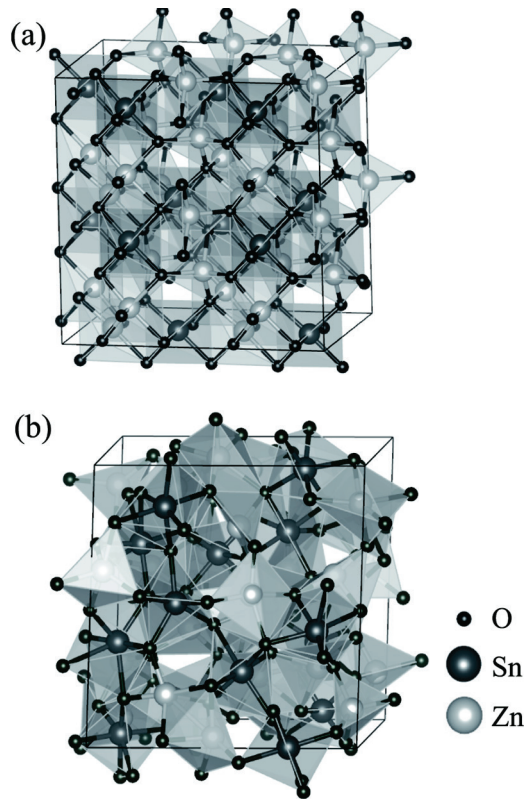


Figure 5.4 Supercells for *ZTO214* composition. (a) Crystalline *ZTO214* (b) Amorphous *ZTO214*.

5.4.2. RDF results of amorphous phases

RDF results show the variations in atom density, the periodicity of locations of atoms, the average bonds lengths and so on. Figure 5.5 shows the RDF result of oxygen related bonds of amorphous phases. For the references, RDF results of the crystalline phases of ZnO, SnO₂ and *ZTO214* (P4₁22) were obtained as the vertical lines. The first peaks of O-Zn and O-Sn mean the ionic bonds between cations and oxygens. The length of O-Sn bond of ternary oxide and binary oxide is almost the same. However, the length of O-Zn of ternary oxide is longer than that of binary oxide.

Figure 5.5.a shows the RDF result of amorphous phase for *ZTO214 composition*. The ionic bonds which can be represented as the first peak of O-Zn and O-Sn can be found at figure 5.5.c. It means the short range orders of amorphous phase exist. However, the other peaks behind the first peaks are disappeared. The long range orders of amorphous are not conserved. Note that the length of the first peak of O-Sn is similar to crystalline ternary and binary oxides. However, the bond length of O-Zn becomes closer to that of binary oxide.

Figure 5.5.b shows the RDF results of oxygen-related bonds for *ZTO113 composition*. The crystalline *LN-ZTO113* phase was used as the reference of ternary oxide. Similarly to the results of *ZTO214 composition*, the bond length of O-Sn of amorphous phase is similar to those of binary and

ternary oxides. However, the bond length of O-Zn of amorphous phase shortened closer to that of ZnO.

Because the O-O bonds were forcibly broken at 0K calculations with the lower system energy, the distance of the first peak of O-O can be found over 3 Å. However, when the amorphous cells include any O-O bond, it can be found with small first peak with the lengths of about 1.5 Å.

Figure 5.6.a and 5.6.b show the RDF results of distances between among cations for *ZTO214* and *ZTO113 compositions*. Note that first peaks are found over the distance of 3 Å. Compared to the bond lengths between oxygen and cations are around 1.9 ~ 2.3 Å, the cations form the second nearest neighbors among themselves in amorphous phases. The distances between Zn-Zn, Sn-Sn and Zn-Sn are similar in amorphous phase. It means Zn and Sn are spread out with making the bonds with oxygen in the whole space.

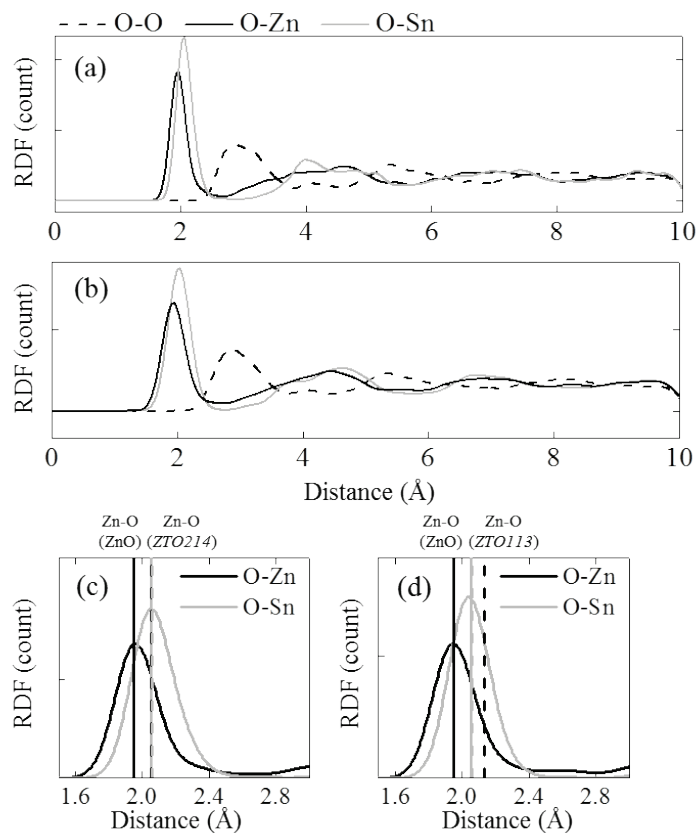


Figure 5.5 RDF results of oxygen related bonds for amorphous zinc tin oxides. (a) *a*-ZTO214 (b) *a*-ZTO113. RDF of around the first peak of (c) *a*-ZTO214. (d) *a*-ZTO113. Vertical lines indicate the bond lengths of crystalline phases.

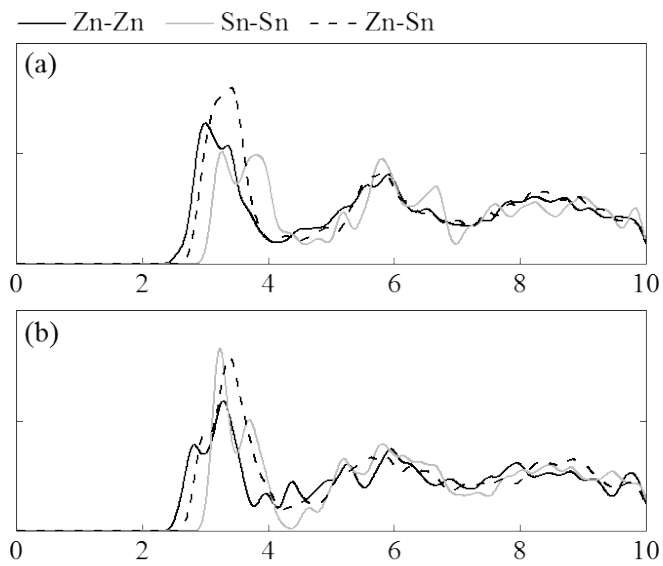


Figure 5.6 RDF results of distances between cations for amorphous zinc tin oxides. (a) *a-ZTO214*. (b) *a-ZTO113*.

5.4.3. Coordination number (CN)

When the RDF is integrated from zero to the cutoff which is selected from the first minimum behind the first peak, the coordination number (CN) can be counted because the first peak means the ionic bonds. The coordination number The cutoff is selected as the first minimum behind the first peak from RDF result. The cutoffs O-Sn and O-Zn were selected as 2.72 and 2.65 Å.

Table 5.1 shows the CNs from the ionic bonds for *ZTO214* compositions. The CNs of crystalline phases are integers or integers divided into two. However, the CNs of amorphous phases are rational numbers because the CNs have deviations.

The CN of Sn of amorphous phase was close to six which is the same with that of binary and ternary oxide. Meanwhile, the CN of Zn of amorphous phases decreased closer to four which is the same with that of binary oxide. Considering the RDF and CN, the Sn-O bonds have smaller deviations with the phase transformations which include various crystalline and amorphous phases. The Zn-O bonds have the tendency to become that of binary oxide.

Table 5.2 shows the CNs from the ionic bonds for *ZTO113* composition. Note that the CN of Zn-O of the crystalline ternary oxide is different from that of binary oxide and the tendency is similar to that for

ZTO214 composition. Although the compositions were different, the tendency of changes of Zn and Sn was similar to that from *ZTO214 composition*.

The different CN of Zn can be one of the reason of increasing the crystallization temperature of ternary oxide. Hoel *et al.*, reported the tetrahedral zinc in amorphous phase causes the higher crystallization temperature in $\text{In}_{2-x}\text{Zn}_x\text{Sn}_x\text{O}_4$ (IZTO). [119] In crystalline IZTO, the CN of Zn is six. However, according to the extended X-ray absorption fine structure (EXAFS) results, the CN of Zn is about four. Similarly to this report, the crystallization temperature of ZTO is over 600 °C which is higher than those of binary oxides. [24]

Table 5.1 The coordination numbers (CN) from the ionic bonds between cations and oxygens for *ZTO214* composition.

CN from Bonds	c- <i>ZTO214</i> (P4 ₁ 22)	c-ZnO	c-SnO ₂	a- <i>ZTO214</i>
O-Zn	2.50	4.00	NA ^a	2.28 ± 0.03
O-Sn	1.50	NA	3.00	1.48 ± 0.03
Zn-O	5.00	4.00	NA	4.55 ± 0.07
Sn-O	6.00	NA	6.00	5.90 ± 0.12

^aNA : Not available

Table 5.2 The coordination numbers (CN) from the ionic bonds between cations and oxygens for *ZTO113* composition.

CN from Bonds	c- <i>ZTO113</i> (LN-type)	c-ZnO	c-SnO ₂	a- <i>ZTO113</i>
O-Zn	2.00	4.00	NA ^a	1.43 ± 0.06
O-Sn	2.00	NA	3.00	1.91 ± 0.01
Zn-O	6.00	4.00	NA	4.30 ± 0.18
Sn-O	6.00	NA	6.00	5.73 ± 0.02

^aNA : Not available

5.4.4. DOS analyses

Figure 5.7 show the DOS of crystalline and amorphous phases *ZTO214*. The GGA+U scheme with tetrahedron method was performed. DOS of crystalline *ZTO214* were extracted from the spinel phase of *ZTO214* with the space group of $P4_122$. The intensities of PDOS were divided into number of each element. The zero energy was selected to the Fermi level which means highest occupied state in the calculations.

As mentioned at chapter 2.6, the VBM of *ZTO214* is mainly formed by the 2p-orbitals of oxygens and 3d-orbitals of zinc. As figure 5.7a and 5.7.b show, the PDOS peaks of the oxygen in VBM region increase compared to those in crystalline phases. Nahm *et al.*, reported that the interaction of oxygen form the tailing states of valence bands. [37]

The CBMs of both crystalline and amorphous *ZTO214* are mainly formed by tin. The intensity of PDOS of tin is larger than those of zinc at the CBM. Reversely, the intensity of PDOS of zinc becomes larger than those of tin over about 3~5 eV of CBM.

Figure 5.7.c show the PDOS of amorphous phase when the O-O bonds form. Because the total number of oxygen is 64, the ratio of O-O is extremely high. As mentioned at chapter 5.4.1, the Frenkel pair is formed as $(O-O)_O + V_O$ state. The highest occupied level increase over the conduction band. For this reason, it should be checked that the amorphous cell made by

the melt-quenching method include O-O bonds in order to avoid getting the different electronic structure.

Figure 5.8 shows the DOS of crystalline and amorphous phases of *ZTO113*. The intensity of PDOS of oxygen increases at the VBM similarly with the results for *ZTO214*.

Figure 5.9 show the inverse population ratio (IPR) of crystalline and amorphous phases of *ZTO214* and *ZTO113*. IPR can be defined as the

$$IPR = \frac{\sum_i |a_i|^4}{\left(\sum_i |a_i|^2\right)^2} \quad (5.3)$$

where $|a_i|^2$ indicates the partial weight on the *i*th atom [105]. If the wavefunction is uniformly distributed over *N* atoms, the value becomes $1/N$. However, when the wavefunction is localized, the value increases. Near the valence band maximum, the value of IPR drastically increases. It means the oxygen interactions form the valence band tails in the range of about 1 eV.

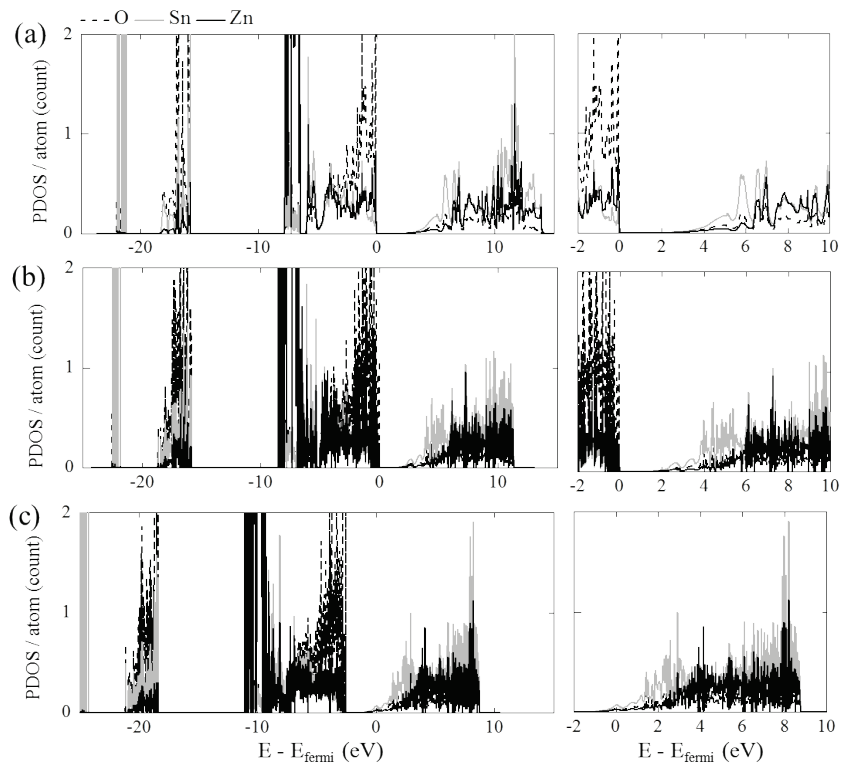


Figure 5.7 PDOSs of *ZTO214* phases in whole range of energy (left) and around bandgap (right). From (a) Crystalline *ZTO214* ($P4_122$). (b) Amorphous *ZTO214*. (c) Amorphous *ZTO214* with O-O bond.

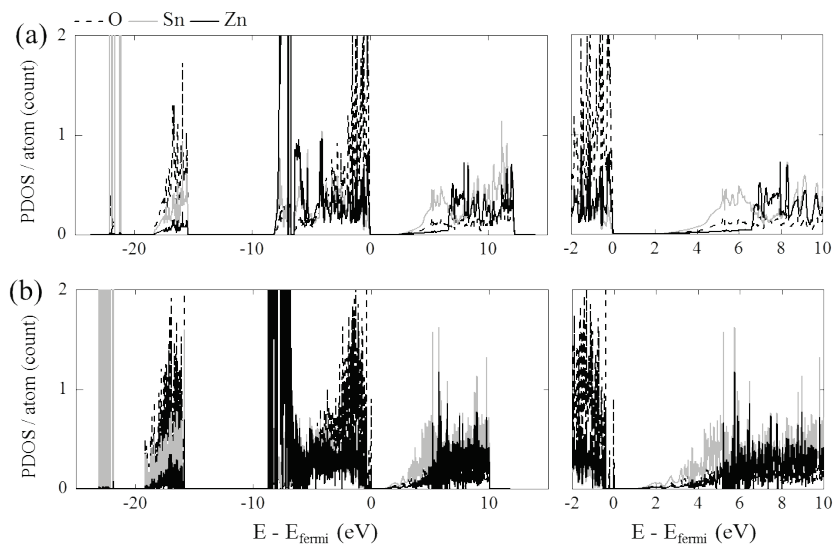


Figure 5.8 PDOSs of various *ZTO113* phases in whole range of energy (left) and around bandgap (right). From (a) Crystalline *ZTO113* (R3c). (b) Amorphous *ZTO113*.

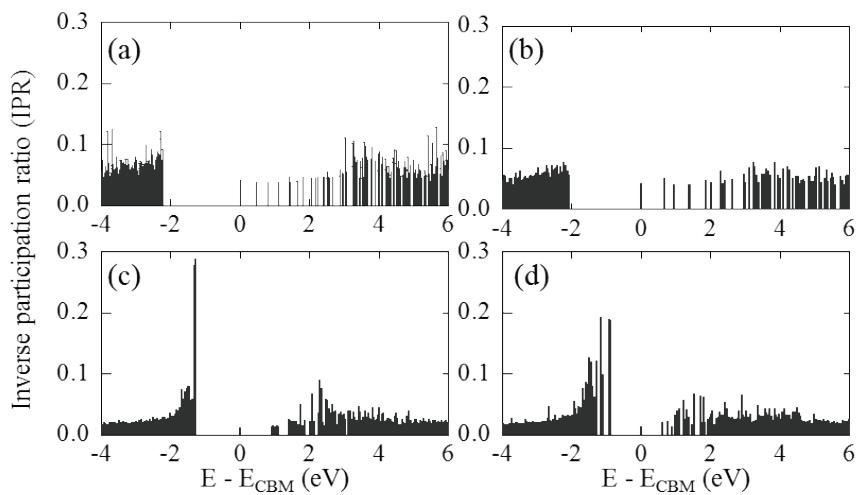


Figure 5.9 Inverse participation ratio (IPR) of crystalline and amorphous ZTOs. From (a) *c-ZTO214*. (b) *c-ZTO113*. (c) *a-ZTO214*. (d) *a-ZTO113*.

5.5. Summary

Melt-quenching based on the AI-MD was performed to get the amorphous phase for *ZTO214* and *ZTO113* composition ratio. The structure analyses such as CN, RDF were obtained to investigate the local atomic structures of amorphous phases. The results showed that Zn and Sn cations are attached to oxygens with forming the ionic bonds. In addition, Sn-O bonds of crystalline ternary, binary and amorphous oxides are similar to each other. Meanwhile, the Zn-O bonds of amorphous phases were similar to those of binary oxides and different from those of crystalline ternary oxides. The clusters of Zn-O and Sn-O are uniformly distributed with the CNs of binary oxides. The local atomic structures of amorphous *ZTO113* and *ZTO214* were the mixture state of *ZTO214* and binary oxides regardless of the compositions. The band tails around the VBM were found and their states were localized.

Chapter 6. Conclusions

Zinc tin oxide is one of the promising transparent conducting oxides due to high performance and low cost. First principle calculations were performed to understand fundamentals of various phases of zinc tin oxides system. Advanced and skillful methods including phonon vibrations, hybrid density functional theory, molecular dynamics based on first principles were performed at the various phases from crystalline bulk system to amorphous phase.

Various crystal phases of zinc tin oxide can form according to different synthesis. The stable phase of Zn_2SnO_4 (*ZTO214*) is reported to be the inverse spinel. The occupancy of octahedral sites by zinc and tin lowers the symmetry of the structure in the atomic scale. $ZnSnO_3$ (*ZTO113*) can form the lithium niobate and ilmenite phases which are alumina based phases with the different occupancy at octahedral sites by zinc, tin and vacancy.

Gibbs energy using first principles calculations including the phonon vibrations was used as the standard of the thermodynamic stability of various phases of zinc tin oxides. The pressure-temperature phase diagram was obtained, and the transition pressures and temperatures were determined and compared to previous synthesis and/or existence conditions for the *ZTO113* and *ZTO214* compositions. At zero pressure, the coexistence of ZnO

and SnO₂ was the most stable phase, and *ZTO214* became more stable above approximately 1300 K. As the external pressure increased, the thermodynamic stability changed in the following sequence: from the coexistence of ZnO and SnO₂ to the coexistence of *ZTO214* and SnO₂ and then to *LN-ZTO113*. The transition pressure to *LN-ZTO113* was much higher for the *ZTO214 composition* than for the *ZTO113 composition*, and the pressurization mainly affected Zn-O bonding compared with Sn-O bonding. The space group of *ZTO214* in the unit cell scale affected the thermodynamic stability of *LN-ZTO113* as well as of *ZTO214*. The LDA functional was found to describe the experimental observations better than the GGA functional by considering the atomic structure, bulk modulus and transition pressure and temperature. The discrepancies between the experimental observations of the various phases of zinc tin oxide and the coexistence of multi-phases can be attributed to the local configurations of the octahedral sites with Zn and Sn in *ZTO214* as well as to the kinetics.

Oxygen vacancy is the representative point defect in oxide system because the concentration of oxygen can be changed by in and out of O₂ gas molecules according to the pressure and temperature. The role of oxygen vacancy and hydrogen interstitial were performed in *ZTO214* phase which is the most stable phase in ternary system. The exchange ratio of Hartree-Fock of 29 % shows the bandgap of 3.6 eV which is the same bandgap with experimental data. The fitting value of L⁻¹ and L⁻³ after Lany-Zunger (LZ)

correction for the image charge correction using GGA+U was the closest to the converged value. LZ correction was obtained to the hybrid functional result. The defect formation energy result shows the neutral oxygen vacancy is stable when the Fermi level is at n-type region. The transition state $\epsilon(2+/0)$ was about 1 eV below the conduction band minimum. It means the oxygen vacancy cannot perform the role of oxygen generator. However, the location of the oxygen vacancy is about 2 eV below the conduction band minimum. Because it can be ionized by photon energy of green color with the emission of electrons to conduction band and perform as the photocurrent source. The defect formation energy of the hydrogen interstitial at the site between the octahedral and tetrahedral site of zinc showed the lowest value. When the hydrogen is incorporated, it always exists as single charged state. One electron is emitted from the shallow state as the charge of hydrogen changes from neutral state to singly charged state from the electronic structure analysis. It means the incorporated hydrogen can generate the electron.

In last, the amorphous phases at *ZTO214* and *ZTO113* composition ratio were obtained by melt-quenching method based on ab-initio molecular dynamics. The coordination numbers (CN) of Zn-O bonds are six, five and four of *ZTO113*, *ZTO214* and ZnO, respectively. Meanwhile, the CN of Sn-O were conserved about six. The radial distribution function (RDF) result shows the coordination number of Zn-O bonds in amorphous phases decreased close to four that of binary oxide of ZnO. It means the Zn-O bonds

follow the local structure of binary oxide of ZnO. Otherwhile, the coordination numbers of Sn-O bonds in crystalline and amorphous phases are conserved as six. Some oxygens were attached only one kind of cations. However, ionic bonds between the oxygen and zinc or tin are conserved. The local atomic structures of amorphous *ZTO113* and *ZTO214* were the mixture state of *ZTO214* and binary oxides regardless of the compositions.

Appendix A. X-ray diffraction (XRD) simulations from ab-initio calculations

Zinc tin oxides (ZTO) are mainly applied to the advanced devices, they are used as the complex structures like amorphous films and nanostructures. The the material information of bulk properties have not much accumulated. X-ray diffraction (XRD) is a useful analysis method for defining the phases and knowing the structural parameters such as lattice constants. However, the XRD patterns about ZTO are rarely reported. So they are narrowly used for checking whether thin films are crystallized or not.

When the atomic structures are defined, the reciprocal lattice is directly defined by Fourier transforms. In addition, atomic structures can be obtained from ab-initio calculations with the cell relaxations. As mentioned at chapter 2.4, the cell volumes obtained hybrid functional results were close to those of experimental reports. The XRD simulations were performed using opt-HSE06. RIETAN-FP [116], which is implemented at "Visualization for Electronic and STructrual Analysis" (VESTA) [117] was used for extracting XRD patterns from the atomic structures.

Figure A.1. shows XRD patterns for various phases of zinc tin oxides. Although the peaks are difficult to split to various phases, they are

useful information for defining the phases. The structures were optimized using opt-HSE06. [65]

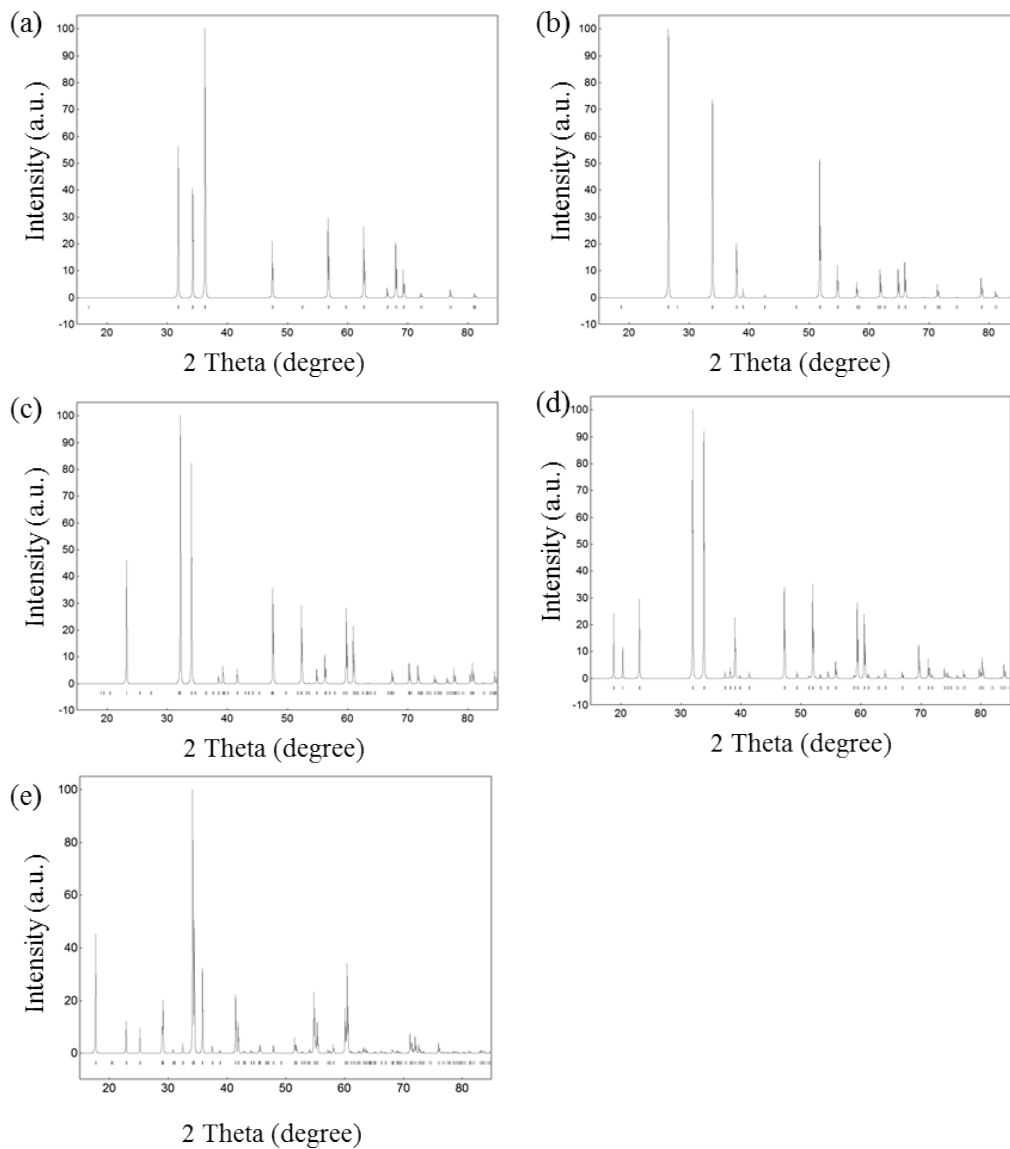


Figure A.1. X-ray diffraction (XRD) simulation of various zinc tin oxides with the optimized structure using opt-HSE06. (a) ZnO. (b) SnO₂. (c) ZTO113 (LN). (d) ZTO113 (IL). (e) ZTO214 (P4,22).

References

- [1] D. S. Ginley, H. Hosono and D. C. Paine, Handbook of Transparent Conductors, (Springer, October 15th, 2010) Vol. **1**, p. 11.
- [2] E. Fortunato, D. Ginley, H. Hosono, D. C. Paine, MRS Bulletin **32** 242 (2007).
- [3] T. Minami, Semicond. Sci. Technol. **20** S35 (2005).
- [4] A. Janotti, C. G. Van de Walle, Rep. Prog. Phys. **72** 126501 (2009).
- [5] K. Nomura, H. Ohta, A. Takagi, T. Kamiya, M. Hirano and H. Hosono, Nature **432** 488 (2004).
- [6] D. S. Ginley, H. Hosono and D. C. "Paine, Handbook of Transparent Conductors", (Springer, October 15th, 2010) Vol. **1**, p. 7.
- [7] K. Nomura, H. Ohta, K. Ueda, T. Kamiya, M. Hirano, H. Hosono, Science **300** 1269 (2003).
- [8] J. F. Wager, Science **300** 1245 (2003).
- [9] P. Görrn, M. Sander, J. Meyer, M. Kröger, E. Becker, H. -H. Johannes, W. Kowalsky, T. Riedl, Adv. Mater. **18** 738 (2006).
- [10] P. Görrn, F. Ghaffari, T. Riedl, W. Kowalsky, Solid. State Electron. **53** 329 (2009).
- [11] J. H. Wu, C. Xu, Y. Zhang, Z. L. Wang, ACS Nano **6** 4355 (2012).
- [12] P. Song, Q. Wang, Z. Yang, Sensors and Actuat. B **156** 983 (2011).
- [13] S. Baruah, J. Dutta, Sci. Technol. Adv. Mater. **12** 013004 (2011).
- [14] M. Lei, F. -L. Kwong, D. H. L. Ng, J. Nanosci. Nanotech. **10** 8432 (2010).
- [15] B. Tan, E. Toman, Y. Li, Y. Wu, J. Am. Chem. Soc. **129** 4162 (2007).

- [16] T. Z. Oo, R. D. Chandra, N. Yantara, R. R. Prabhakar, L. H. Wong, N. Mathews, S. G. Mhaisalkar, *Org. Electron.* **13** 870 (2012).
- [17] B. S. Yang, S. Park, S. Oh, Y. J. Kim, J. K. Jeong, C. S. Hwang, and H. J. Kim, *J. Mater. Chem.* **22** 10994 (2012).
- [18] S. H. Rha, J. Jung, Y. S. Jung, Y. J. Chung, U. K. Kim, E. S. Hwang, B. K. Park, T. J. Park, J.-H. Choi and C. S. Hwang, *Appl. Phys. Lett.* **100** 203510 (2012).
- [19] J. S. Jung, S.-H. Rha, U. K. Kim, Y. J. Chung, Y. S. Jung, J.-H. Choi and C. S. Hwang, *Appl. Phys. Lett.* **100** 183503 (2012).
- [20] "Mineral Commodities Summary 2007 : Indium", United States Geological Survey. Retrieved 2007-12-26.
- [21] H. Q. Chiang, J. F. Wager, R. L. Hoffman, J. Jeong, D. A. Keszler, *Appl. Phys. Lett.* **86** 013503 (2005).
- [22] W. B. Jackson, R. L. Hoffman, G. S. Herman, *Appl. Phys. Lett.* **87** 193503 (2005).
- [23] D. L. Young, H. Moutinho, Y. Yan, T. J. Coutts, *J. Appl. Phys.* **92** 310 (2002).
- [24] D. L. Young, D. L. Williamson, T. J. Coutts, *J. Appl. Phys* **91** 1464 (2002).
- [25] Y. Inaguma, M. Yoshida, T. Katsumata, *J. Am. Chem. Soc.* **130** 6704 (2008).
- [26] D. Kovacheva, K. Petrov, *Solid State Ionics* **109** 327 (1998).
- [27] T. Minami, H. Sonohara, S. Takata, H. Sato, *Jpn. J. Appl. Phys.* **33** 1693 (1994).
- [28] Y. Hayashi, K. Kondo, K. Murai, T. Moriga, I. Nakabayashi, H.

- Fukumoto, K. Tominaga, *Vacuum* **74** 607 (2004).
- [29] A. Janotti, C. G. Van de Walle, *Appl. Phys. Lett.* **87** 122102 (2005).
- [30] P. Ágoston, K. Albe, R. M. Nieminen and M. J. Puska, *Phys. Rev. Lett.* **103** 245501 (2009).
- [31] S. Lany and A. Zunger, *Phys. Rev. B* **81** 113201 (2010).
- [32] H. Omura, H. Kumomi, K. Nomura, T. Kamiya, M. Hirano and H. Hosono, *J. Appl. Phys.* **105** 093712 (2009).
- [33] H. -K. Noh, K. J. Chang, B. Ryu and W. -J. Lee, *Phys. Rev. B* **84** 115205 (2011).
- [34] Ç. Kılıç and A. Zunger, *Phys. Rev. Lett.* **88** 095501 (2002).
- [35] S. Lany and A. Zunger, *Phys. Rev. Lett.* **106** 069601 (2011).
- [36] Morkoç H, Özgür Ü, “Zinc Oxide : Fundamentals, Materials and Device Technology” (Wiley-VCH. February 24, 2009), Vol. **1**, p.1.
- [37] H. -H. Nahm, Y. -S. Kim, D. H. Kim, *Phys. Stat. Sol. B* **6** 1277 (2012).
- [38] B. S. Yang, S. Park, S. Oh, Y. J. Kim, J. K. Jeong, C. S. Hwang, H. J. Kim, *J. Mater. Chem.* **22** 10994 (2012).
- [39] J. H. Kim, U. K. Kim, Y. J. Chung, C. S. Hwang, *Appl. Phys. Lett.* **98** 232102 (2011).
- [40] Y. J. Chung, J. H. Kim, U. K. Kim, M. Ryu, S. Y. Lee, C. S. Hwang, *Electrochem. Solid-State Lett.* **14** H300 (2011).
- [41] P. Görrn, M. Lehnhardt, T. Riedl, W. Kowalsky, *Appl. Phys. Lett.* **91** 193504 (2007).
- [42] H. Oh, S. -M. Yoon, M. K. Ryu, C.-S. Hwang, S. Yang, *Appl. Phys. Lett.* **97** 183502 (2010).

- [43] J. -Y. Kwon, J. S. Jung, K. S. Son, K. -H. Lee, J. S. Park, T. S. Kim, J. -S. Park, R. Choi, J. K. Jeong, B. Koo, S. Y. Lee, *Appl. Phys. Lett.* **97** 183503 (2010).
- [44] W. -T. Chen, H. -W. Hsueh, H. -W. Zan, C. -C. Tsai, *Electrochem. Sol. Stat. Lett.* **14** H297 (2011).
- [45] B. Ryu, H. K. Noh, E. -A. Choi, K. J. Chang, *Appl. Phys. Lett.* **97** 022108 (2010).
- [46] T. Kamiya, K. Nomuran, H. Hosono, *Phys. Stat. Sol. A* **5** 860 (2009).
- [47] T. Kamiya, K. Nomura, H. Hosono, *Phys. Stat. Sol. A* **7** 1698 (2010).
- [48] A. E. Mattson, P. A. Schultz, M. P. Desjarlais, T. R. Mattsson, K. Leung, *Modelling Simul. Mater. Sci. Eng.* **13** R1 (2005).
- [49] J. Hafner, *Acta Mater.* **48** 71 (200).
- [50] D. M. Ceperley and M. H. Kalos, "Monte Carlo Methods in Statistical Physics" (ed. K. Binder, Springer, Berlin, 1986) p. 145.
- [51] R. Dovesi, C. Roetti, C. Freyria-Fava, E. Apra, V. R. Saunders, N. M. Harrison, *Phil. Trans. R. Soc. Lond.* **A341** 203 (1992).
- [52] P. Hohenberg, W. Kohn, *Phys. Rev.* **B136** 864 (1964).
- [53] W. Kohn and L. J. Sham, *Phys. Rev.* **140** A1133 (1964).
- [54] D. M. Ceperley, B. J. Alder, *Phys. Rev. Lett.* **45** 566 (1980).
- [55] S. H. Vosko, L. Wilks, M. Nusair, *Can. J. Phys.* **58** 1200 (1980).
- [56] J. P. Perdew, A. Zunger, *Phys. Rev. B* **23** 5048 (1981).
- [57] J. P. Perdew, K. Burke, M. Ernzerhof, *Phys. Rev. Lett.* **77** 3865 (1996).

- [58] G. Kresse , J. Furthmüller, Phys. Rev. B **54** 11169 (1996).
- [59] G. Kresse, J. Furthmüller, J. Comput. Mater. Sci. **6** 15 (1996).
- [60] M. Marsman, J. Paier, A. Stroppa, G. Kresse, J. Phys. Condens. Matter **20** 064201 (2008).
- [61] S. Park, B. Lee, S. H. Jeon, S. Han, Curr. Appl. Phys. **11** S337 (2011).
- [62] V. I. Anisimov, J. Zaanen, O. K. Andersen, Phys. Rev. B **44** 943 (1991).
- [63] S. L. Dudarev, G. A. Botton, S. Y. Savrasov, C. J. Humphreys, A. P. Sutton, Phys. Rev. B **57** 1505 (1998).
- [64] J. P. Perdew, M. Ernzerhof, K. Burke, J. Chem. Phys. **105** 9982 (1996).
- [65] J. Heyd, G. E. Scuseria, M. Ernzerhof, J. Chem. Phys. **118** 8207 (2003); **124** 219906 (2006).
- [66] P. Sánchez-Friera, R. W. Godby, Phys. Rev. Lett. **85** 5611 (2000).
- [67] F. Oba, M. Choi, A. Togo, A. Seko and I. Tanaka, J. Phys. Condens. Matter **22** 384211 (2010).
- [68] A. K. Singh, A. Janotti, M. Scheffler and C. G. Van de walle, Phys. Rev. Lett. **101** 055502 (2008).
- [69] S. -H. Wei, S. B. Zhang, Phys Rev B **63** 045112 (2001).
- [70] A. Seko, F. Oba, I. Tanaka, Phys Rev B **81** 054114 (2010).
- [71] G. B. Palmer, K. R. Poepfelmeier, Solid State Sci. **4** 317 (2002).
- [72] S. Harvey, K. R. Poepfelmeier, T. O. Mason, J. Am. Ceram. Soc. **91** 3683 (2008).
- [73] L. Gracia, A. Beltrán, J. Andrés, J. Phys. Chem. C **115** 7740 (2011).

- [74] J. B. Goodenough, J. J. Stickler, Phys Rev **164** 768 (1967).
- [75] P. E. Blöchl, Phys Rev B **50** 17953 (1994).
- [76] H. J. Monkhorst, J. D. Pack, Phys. Rev. B **13** 5188 (1976).
- [77] F. Birch, Phys Rev **71** 809 (1947).
- [78] R. P. Stoffel, C. Wessel, M. -W. Lumeey, R. Dronskowski, Angew. Chem. Int. Ed. **49** 5242 (2010).
- [79] H. Karzel, W. Potzel, W. Schiessl, M. Steiner, U. Hiller, G. M. Kalvius, D. W. Mitchell, T. P. Das, P. Blaha, K. Schwarz, M. P. Pasternak, Phys. Rev. B **53** 11425 (1996).
- [80] J. E. Jaffe, J. A. Snyder, Z. Lin, A. C. Hess, Phys. Rev. B **62** 1660 (2000).
- [81] Haines J, Léger JM, Phys. Rev. B **55** 11144 (1999).
- [82] Zhu B, Liu C-M, Lv M-B, Chen X-R, Zhu J, Ji G-F, Physica B **406** 3508 (2011).
- [83] L. Gracia, A. Beltrán, J. Andrés, J. Phys. Chem. B **111** 6479 (2007).
- [84] H. Wang, H. Huang, B. Wang, Solid State Comm. **149** 1849 (2009).
- [85] H. Gou, F. Gao, J. Zhang, Comput. Mat. Sci. **49** 552 (2010).
- [86] N. -N. Ge, C. -M. Liu, Y. Cheng, X. -R. Chen, G. -F. Ji, Physica B **406** 742 (2011).
- [87] R. J. Hill, J. R. Craig, G. V. Gibbs, Phys. Chem. Miner. **4** 317 (1979).
- [88] F. Birch, J. Geophys. Res. **57** 227 (1952).
- [89] M. Nakayama, M. Nogami, M. Yoshida, T. Katsumata, Y. Inaguma, Adv. Mater. **22** 2579 (2010).
- [90] H. Gou, J. Zhang, Z. Li, G. Wang, F. Gao, R. C. Ewing, J. Lian,

- Appl. Phys. Lett. **98** 091914 (2011).
- [91] S. Baroni, P. Giannozzi, A. Testa, Phys. Rev. Lett. **58** 1861 (1987).
- [92] A. Togo, F. Oba, I. Tanaka, Phys. Rev. B **78** 134106 (2008).
- [93] A. Togo, L. Chaput, I. Tanaka, G. Hug, Phys. Rev. B **81** 174301 (2010).
- [94] M. P. Allen, "Introduction to Molecular Dynamics Simulation", (John von Neumann Institute for Computing, Jülich, NIC Series, Vol. **23**, ISBN 3-00-012641-4, 2004) pp. 1-28.
- [95] C. A. Hoel, T. O. Mason, J. -F. Gaillard, K. R. Poepfelmeier, Chem. Mater. **22** 3569 (2010).
- [96] J. G. Lee, "Computational materials science : An Introduction", (Talyor & Francies Group, 2011) Vol. **1**, pp. 9-45.
- [97] Y. -M. Chiang, D. P. Birnie, W. D. Kingery, "Physics Ceramics", (Wiley, May 11th, 1996) Vol. **1**, pp.13-19
- [98] C. G. Van de Walle, J. Neugebauer, J. Appl. Phys. **95** 3851 (2004).
- [99] M. Leslie, M. J. Gillan, J. Phys. C: Solid State Phys. **18** 973 (1985).
- [100] G. Makov, M. C. Payne, Phys. Rev. B **51** 4014 (1995).
- [101] S. Lany, A. Zunger, Phys. Rev. B **78** 235104 (2008).
- [102] S. Lany, A. Zunger, Model. Simul. Mater. Sci. Eng. **17** 084002 (2009).
- [103] A. Zunger, Appl. Phys. Lett. **83** 57 (2003).
- [104] J. Akola, R. O. Jones, Phys. Rev. B **76** 235201 (2007).
- [105] E. Cho, S. Han, D. Kim, H. Horii, H. -S. Nam, J. Appl. Phys. **109** 043705 (2011).
- [106] E. Cho, Y. Young, S. Han, Appl. Phys. Lett. **99** 183501 (2011).

- [107] A. Walsh, J. L. F. Da Silva, S. -H. Wei, Chem. Mater. **21** 5119 (2009).
- [108] S. L. Roux, V. Petkov, J. Appl. Cryst. **43** 181 (2010).
- [109] S. H. Sun, G. W. Meng, M. G. Zhang, X. H. An, G. S. Wu, L. D. Zhang, J. Phys. D: Appl. Phys. **37** 409 (2004).
- [110] Y. Wei, Y. Ding, C. Li, S. Xu, J. -H. Ryo, R. Dupuis, A. K. Sood, D. L. Polla, Z. L. Wang, J. Phys. Chem. C **112** 18935 (2008).
- [111] D. Marx, J. Hutter, "*Ab-initio* molecular dynamics: Theory and Implementation", (John von Neumann Institute for Computing, Jülich, NIC Series, ISBN 3-00-005618-1, 2000), Vol. **1**, pp. 301-449.
- [112] H. -R. Kim, D. -H. Kim, E. Byon, G. -H. Lee, G. - H. Lee, P. -K. Song, Jap. J. Appl. Phys. **49** 121101 (2010).
- [113] W. -K. Kim, S. Lee, Y. C. Cho, H. Koinuma, S. -Y. Jeong, J. M. Shin, C. R. Cho, J. -S. Bae, T. -Y. Kim, S. Park, Appl. Phys. Lett. **98** 122109 (2011).
- [114] C. G. Van de Walle, Phys. Rev. Lett. **85** 1012 (2000).
- [115] C. G. Van dew Walle, J. Neugebauer, Nature **423** 626 (2003).
- [116] F. Izumi, K. Momma, Sol. Stat. Phenom. **130** 15 (2007).
- [117] K. Momma, F. Izumi, J. Appl. Crystallogr. **44** 1272 (2011).
- [118] E. Cho, J. Im, C. Park, W. J. Son, D. H. Kim, H. Horii, J. Ihm, S. Han, J. Phys.: Condens. Matter **22** 205504 (2010).
- [119] C. A. Hoel, S. Xie, C. Benmore, C. D. Malliakas, J. -F. Gaillard, K. R. Poeppelmeier, Z. Anorg. Allg. Chem. **637** 885 (2011).

Curriculum Vitae

Joohwi Lee

Department of Materials Science and Engineering

College of Engineering, Seoul National University

San 56-1 Silim-dong, Gwanak-gu, Seoul, 151-742, Korea

Tel: +82-02-874-6414

E-mail: lee.joohwi@gmail.com

EDUCATION

M.S. & Ph. D. course, Department of Materials Science and Engineering

Seoul National University, Seoul, Korea

2007.03 – 2013.02

B.S., Department of Materials Science and Engineering

Seoul National University, Seoul, Korea

2003.03 – 2007.02

ACADEMIC EXPERIENCES

Researcher, Electronic Materials Research Center

Korea Institute of Science and Technology, Korea

2012.01 – 2013.02

Student Researcher, Computational Science Research Center

Korea Institute of Science and Technology, Korea

2009.05 – 2011.12

Exchange Student Researcher, Department of Materials Engineering

University of Tokyo, Japan

2010.01 – 2010.03

RESEARCH SKILLS

1. *Ab-initio* calculations

- Thermodynamics and defects on various phases of transparent oxide semiconductors
- Strain effects in semiconductors

2. Thinfilm depositions and analysis

- High-k on Ge substrates for MIS capacitors
- MgO discharge films for plasma display panels (PDPs)

TECHNICAL SKILLS

1. *Ab-initio* calculations

- Thermodynamic calculations with phonon vibrations
- Defect calculations using DFT+U / hybrid functionals
- Nudged elastic bands (NEB)
- *Ab-initio* molecular dynamics

2. Depositions and analyses of thin films

- Electron beam (e-beam) evaporator and atomic layer depositions (ALD) for depositions of metal and oxide films
- Powder sintering for e-beam targets
- X-ray diffraction (XRD) and x-ray reflection (XRR)
- Electrical measurements using HP4194A for C-V and HP4145B and HP4155A for I-V measurement of MIS capacitors
- Ellipsometer for film thickness measurement
- Furnace for ambient and vacuum annealing

List of publications

1. Journals (SCI)

1.1 International

13. **Joohwi Lee**, Seung-Cheol Lee, Cheol Seong Hwang, Jung-Hae Choi, "Stability of various phases of zinc tin oxides from *ab-initio* thermodynamics", submitted (2013).
12. Sae-Jin Kim, **Joohwi Lee**, Seung-Cheol Lee, Cheol Seong Hwang, Jung-Hae Choi, "*Ab-initio* Calculations on the Atomic and Electronic Structures of Oxygen-Doped Hexagonal Ge₂Sb₂Te₅", Appl. Phys. Express **5** 071801 (2012).
11. Sae-Jin Kim, **Joohwi Lee**, Seung-Cheol Lee, Chan Park, Cheol Seong Hwang, Jung-Hae Choi, "Migration of nitrogen in hexagonal Ge₂Sb₂Te₅: An *ab-initio* study", Phys. Status Solidi RRL **6** 3 108 (2012).
10. Hyung-Suk Jung, Hyo Kyeom Kim, Il-Hyuk Yu, Sang Young Lee, **Joohwi Lee**, Jinho Park, Jae Hyuck Jang, Sang-Ho Jeon, Yoon Jang Chung, Deok-Yong Cho, Nae-In Lee, Tae Joo Park, Jung-Hae Choi, Cheol Seong Hwang, "Properties of atomic layer deposited HfO₂ films on Ge substrates depending on process temperatures", J. Electrochem. Soc. **159** G33 (2012).
9. **Joohwi Lee**, Kwang Duk Na, Seung-Cheol Lee, Cheol Seong Hwang, Jung-Hae Choi, "Effects of magnitude and direction of the biaxial compressive strain on the formation and migration of a vacancy in Ge by using density functional theory", J. Appl. Phys. **110** 033504 (2011).
8. Tae Joo Park, Jeong Hwan Kim, Jae Hyuck Jang, Un Ki Kim, Sang Young

- Lee, **Joohwi Lee**, Hyung Suk Jung, and Cheol Seong Hwang, "Improved growth and electrical properties of atomic-layer-deposited metal-oxide film by discrete feeding method of metal precursor", Chem. Mater. **23** (7) 1654 (2011).
7. Hyung-Suk Jung, Sang-Ho Rha, Hyo Kyeom Kim, Jeong Hwan Kim, Seok-Jun Won, **Joohwi Lee**, Sang Young Lee, Cheol Seong Hwang, Jung-Min Park, Weon-Hong Kim, Min-Woo Song, Nae-In Lee, " Turn-around effect of V_{th} shift during the positive bias temperature instability of the n-type transistor with HfO_xN_y gate dielectrics", IEEE Electron Device Lett. **31** 12 1479 (2010).
6. Hyung-Suk Jung, Jung-Min Park, Hyo Kyeom Kim, Jeong Hwan Kim, Seok-Jun Won, **Joohwi Lee**, Sang Young Lee, Cheol Seong Hwang, Weon-Hong Kim, Min-Woo Song, Nae-In Lee, Deok-Yong Cho, " The bias temperature instability characteristics of *in-situ* nitrogen incorporated ZrO_xN_y gate dielectrics", Electrochem. Solid-St. Lett. **13** (9) G71 (2010).
5. Hyung-Suk Jung, Jeong Hwan Kim, **Joohwi Lee**, Sang Young Lee, Un Ki Kim, Cheol Seong Hwang, Jung-Min Park, Weon-Hong Kim, Min-Woo Song, Nae-In Lee, "Bias temperature instability characteristics of n- and p-type field effect transistors using HfO₂ gate dielectrics and metal gate", J. Electrochem. Soc. **157** 3 H355 (2010).
4. Tae Joo Park, Jeong Hwan Kim, Jae Hyuck Jang, **Joohwi Lee**, Sang Woon Lee, Sang Young Lee, Hyung Suk Jung, Cheol Seong Hwang, "Effects of annealing environment on interfacial reactions and electrical properties of ultrathin SrTiO₃ on Si", J. Electrochem. Soc. **156** (9) G129 (2009).
3. Myung Soo Huh, Bong Seop Yang, **Joohwi Lee**, Jaeyeong Heo, Sang Jin Han,

- Kapsoo Yoon, Sung-Hoon Yang, Cheol Seong Hwang, Hyeong Joon Kim, "Improved electrical properties of tin-oxide films by using ultralow-pressure sputtering process" *Thin Solid Films* **518** 1170 (2009).
2. Myung Soo Huh, Bong Seop Yang, Seungha Oh, **Joohwi Lee**, Kapsoo Yoon, Jae Kyeong Jeong, Cheol Seong Hwang, and Hyeong Joon Kim, "Improvement in the performance of Tin Oxide thin-film transistors by Alumina doping", *Electrochem. Solid-St. Lett.* **12** (10) H385 (2009).
1. Sung Hwan Moon, Tae Wook Heo, Sun Young Park, Jae Hyuk Kim, Young Chul Choi, Sung Il Ahn, **Joohwi Lee**, Hyeong Joon Kim, "The effects of (Ba,Sr,Ca)CO₃ or LaB₆ addition on the x-ray photoelectron spectroscopy spectra and electrical properties of the MgO thin films in alternating current plasma display panels", *J. Mater. Res.* **23** 2 (2008).

2. Conferences

2.1 International

13. **Joohwi Lee**, Seung-Cheol Lee, Cheol Seong Hwang, Jung-Hae Choi, "Point Defects in Inverse Spinel Zinc Tin Oxide Using DFT+U and Screened Hybrid Functional Approach", IUMRS-ICEM 2012 (oral), 23-28 Sep. 2012, Pacifico Yokohama, Japan.
12. **Joohwi Lee**, Seung-Cheol Lee, Cheol Seong Hwang, Jung-Hae Choi, "Structural, electronic, and thermodynamic properties of inverse spinel phase Zn₂SnO₄", ai-WISE (poster), 23-26 Oct. 2011, Rinberg Castle.
11. Hyung-Suk Jung, **Joohwi Lee**, Hyo Kyeom Kim, Sang Young Lee, Nae-In Lee, and Cheol Seong Hwang, "The impact of ALD grown SiO_xN_y and AlO_xN_y passivation layers on the electrical properties of metal gate/high-k Ge

- MOS capacitors", International Symposium on Integrated Functionalities(ISIF) 2011 (oral), 31 Jul. - 4 Aug. 2011, Cambridge, England.
10. **Joohwi Lee**, Kwand Duk Na, Jung-Hae Choi, Seung-Cheol Lee, Tomofumi Tada, Satoshi Watanabe, Cheol Seong Hwang, "Formation and migration of a vacancy in Ge under biaxial compressive strain by first-principles calculations", Psi-k Conference 2010 (poster), 12-16 Sep. 2010, Berlin, Germany.
 9. Hyung-Suk Jung, Hyo Kyeom Kim, Jeong Hwan Kim, Sang Young Lee, **Joohwi Lee**, Cheol Seong Hwang, Jung-Min Park, Weon-Hong Kim, Min-Woo Song, Nae-In Lee, "The effect on nitrogen in in-situ PEALD grown HfO_xN_y gate dielectrics on electrical and bias temperature instability characteristics", ALD 2010 (poster), 21-23 Jun. 2010, Seoul, Korea.
 8. Tae Joo Park, Jeong Hwan Kim, Jae Hyuck Jang, Un Ki Kim, Sang Young Lee, **Joohwi Lee**, Hyung Suk Jung, Kwang Duk Na, Cheol Seong Hwang, "Improved growth behavior and electrical properties of ALD HfO_2 film using discrete feeding method (DFM) of metal-organic precursor", ALD 2009 (poster), 19-22 Jul. 2009, Monterey, CA.
 7. Jeong Hwan Kim, Tae Joo Park, Jae Hyuck Jang, Un Ki Kim, Hyung Suk Jung, Sang Young Lee, Minha Seo, **Joohwi Lee**, Him Chan Oh, and Cheol Seong Hwang, "Electrical properties and chemical analysis of Hafnium oxide thin films deposited by ALD at very low temperature (≤ 100 °C)", ALD 2009 (poster), 19-22 Jul. 2009, Monterey, CA.
 6. Jeong Hwan Kim, Tae Joo Park, Jae Hyuck Jang, Un Ki Kim, Hyung Suk Jung, Sang Young Lee, Minha Seo, **Joohwi Lee**, Him Chan Oh, and Cheol Seong Hwang, "Electrical properties and chemical analysis of Hafnium oxide

- thin films deposited by ALD at very low temperature ($\leq 100^\circ\text{C}$)", ALD 2009, 19-22 Jul. 2009, Monterey, CA.
5. Tae Joo Park, Jeong Hwan Kim, Jae Hyuck Jang, Un Ki Kim, Sang Young Lee, **Joohwi Lee**, Hyung Suk Jung, Kwang Duk Na, and Cheol Seong Hwang, "Improved growth behavior and electrical properties of ALD HfO₂ film using discrete feeding method (DFM) of metal-organic precursor", ALD 2009, 19-22 Jul. 2009, Monterey, CA.
 4. Hyung-Suk Jung, Tae Joo Park, Jeong Hwan Kim, Sang Young Lee, **Joohwi Lee**, Him Chan Oh, Kwang Duck Na, Jung-Min Park, Weon-Hong Kim, Min-Woo Song, Nae-In Lee, Cheol Seong Hwang, "Systematic Study on Bias Temperature Instability of Various High-k Gate Dielectrics ; HfO₂, HfZr_xO_y and ZrO₂", IRPS, Apr. 2009.
 3. Sun Young Park, **Joohwi Lee**, Sung Hwan Moon, Jae Hyuk Kim, Hyeong Joon Kim, "The effect of the flux angle on the crystallographic texture of MgO films deposited by glancing angle deposition method", IUMRS-ICA 2008 (oral), Nagoya, Japan, December 9-13, (2008).
 2. **Joohwi Lee**, Sun Young Park, Sung Hwan Moon, Jae Hyuk Kim, Hyeong Joon Kim, "Properties and discharge characteristics of Mg_{1-x}Mn_xO thin films deposited by e-beam evaporation for AC-PDPs", IUMRS-ICA 2008 (oral), 9-13 Dec. 2008, Nagoya, Japan.
 1. Sun Young Park, Sung Hwan Moon, Tae Wook Heo, Jae Hyuk Kim, **Joohwi Lee**, Hyeong Joon Kim, "Effects of surface geometry of MgO protective layer for AC-PDPs", 2007 International Meeting on Information Display, 27-31 Aug. 2007, Daegu, Korea, pp. 1395-1398.

2.2 Domestic

13. **Joohwi Lee**, Seung-Cheol Lee, Cheol Seong Hwang, Jung-Hae Choi, "Effects of pressure and temperature on various zinc tin oxide phases using *ab-initio* thermodynamics", 8th KIAS electronic structure calculation workshop (poster), 21-22 Jun. KIAS(고등과학원).
12. **Joohwi Lee**, Seung-Cheol Lee, Cheol Seong Hwang, Jung-Hae Choi, "제일원리 계산을 이용한 산화아연주석의 점결함 형성 및 이동에 관한 연구", 2012년도 대한금속재료학회 춘계학술대회 (oral), 26-27 Apr. 2012, 현대 성우리조트, 횡성.
11. Sae-Jin Kim, **Joohwi Lee**, Seung-Cheol Lee, Cheol Seong Hwang, Jung-Hae Choi, "Behaviors of nitrogen in crystalline $\text{Ge}_2\text{Sb}_2\text{Te}_5$ ", 7th KIAS electronic structure calculation workshop (invited), 23-24 Jun. 2011, KIAS(고등과학원).
10. **Joohwi Lee**, Seung-Cheol Lee, Cheol Seong Hwang, Jung-Hae Choi, "*Ab-initio* phonon calculations on the various ZnSnO phases", 7th KIAS electronic structure calculation workshop, 23-24 Jun. 2011, KIAS(고등과학원).
9. Sae-Jin Kim, **Joohwi Lee**, Seung-Cheol Lee, Cheol Seong Hwang, Chan Park, Jung-Hae Choi, "Ab-initio calculations on the energy barrier of nitrogen diffusion in hexagonal $\text{Ge}_2\text{Sb}_2\text{Te}_5$ ", Korean Ceramic Society Spring meetings, 21-22 Apr. 2011, Gyonggi Univ.
8. **Joohwi Lee**, Seung-Cheol Lee, Cheol Seong Hwang, Jung-Hae Choi, "First-principles phonon calculations on the various zinc tin oxide phases", Korean Ceramic Society Spring meetings, 21-22 Apr. 2011, Gyonggi Univ.
7. **Joohwi Lee**, Jung-Hae Choi, Seung-Cheol Lee, Cheol Seong Hwang, "First-

principles calculations on the formation and migration of the vacancy in strained Ge", 대한금속재료학회 춘계학술대회 (oral), 22-23 Apr. 2010, 현대성우리조트, 횡성.

6. **Joohwi Lee**, Seung-Cheol Lee, Cheol Seong Hwang, Jung-Hae Choi, "First-principles calculations on the formation and migration of the vacancy in strained Ge", 2010 Spring Conference of the Korean Institute of Metals and Materials, 22-23 Apr. 2010. 대구 EXCO.
5. Hyung-Suk Jung, Tae Joo Park, Jeong Hwan Kim, Sang Young Lee, **Joohwi Lee**, Jung-Min Park, Weon-Hong Kim, Min-Woo Song, Nae-In Lee, Cheol Seong Hwang, "NBTI and PBTI characteristics of HfO_2 , HfZr_xO_y and ZrO_2 ", The 16th Korean Conference on Semiconductors, 18-20 Feb. 2009.
4. Sung Hwan Moon, Sun Young Park, Jae Hyuk Kim, **Joohwi Lee**, Hyeong Joon Kim, " The effects of NiO addition on the properties of MgO thin films in alternating current plasma display panels (AC-PDPs)", Korean Crystallographic Association, Spring, 2008.
3. Jae Hyuk Kim, **Joohwi Lee**, Sung Hwan Moon, Sun Young Park, Hyeong Joon Kim, "A research on the SrO based protective layer for AC-PDP", Korean Crystallographic Association, Spring, 2008.
2. Sung Hwan Moon, Tae Wook Heo, Sun Young Park, Jae Hyuk Kim, **Joohwi Lee**, Hyeong Joon Kim, "The effect of NiO doping on the electrical properties of MgO protective layer", Korean Crystallographic Association, Fall, 2007.
1. Sun Young Park, Sung Hwan Moon, **Joohwi Lee**, Jae Hyuk Kim, Tae Wook Heo, Hyeong Joon Kim, " The growth of MgO thin films deposited by glancing angle deposition method", Korean Crystallographic Association,

Fall, 2007.

3. Academic Honors

1. IUMRS 2008 conference - Young Researcher Awards (best presentations)

Joohwi Lee, Sun Young Park, Sung Hwan Moon, Jae Hyuk Kim, Hyeong Joon Kim, "Properties and discharge characteristics of $Mg_{1-x}Mn_xO$ thin films deposited by e-beam evaporation for AC-PDPs", IUMRS-ICA 2008 (oral), 9-13 Dec. 2008, Nagoya, Japan.

Abstract (in Korean)

산화주석아연 (zinc tin oxide)는 우수한 투명도, 높은 전도도, 화학적 선택성 등으로 TFT와 태양전지의 채널층, 가스 센서 등에 이용되는 투명전도산화물이다. 이 물질은 주로 비정질이나 나노클러스터 형태로 응용이 된다. 그러나, 물질 기본 물성에 대해서는 많이 알려지지 않았다. 제일원리 계산법은 원자와 전자 상호 작용을 고려해 기본 물성을 연구하는 유용한 시뮬레이션 방법이다.

산화주석아연은 다른 합성법에 따라 다양한 결정질 상을 이루고 있다. 안정상인 Zn_2SnO_4 은 역스피넬을 이룬다고 알려져 있다. 아연과 주석이 팔면체 격자점에 들어감에 따라 원자 단위에서 구조의 대칭성이 변하게 된다. $ZnSnO_3$ 은 알루미늄 상을 기초로 하고 있는 구조를 갖고 있는데, 주석, 아연, 그리고 공공이 팔면체 격자점에 들어간 배열에 따라 lithium niobate와 ilmenite 상으로 분류할 수 있다.

포논 진동과 배열 엔트로피가 반영된 밀도범함수 이론을 적용한 깁스에너지 비교를 통해 다양한 산화주석아연의 열적 안정성에 대해 연구하였다. 압력-온도 상 평형도를 얻었고, 그 결과 압력과 온도가 0일 때부터 저온일 때까지, ZnO 와 SnO_2 로 있는 경우가 가장 안정했다. Zn_2SnO_4 는 약 1000~1300 K 이상의 고온에서 안정하였다. 압력의 증가는 주석-산소간 결합에 영향을 주며 열적 안정상을 다음과 같이 변화시켰다. 압력이 증가함에 따라 ZnO 과 SnO_2 의 상태에서 Zn_2SnO_4 와 SnO_2 의 상태, 그리고 마지막으로 lithium niobate 상의 $ZnSnO_3$ 상으로 변화하였다. Ilmenite 상의 $ZnSnO_3$ 는 상대적으로 높은 에너지와 음의 부호를 가진 포논 진동수로 인해 열적으로 불안정함을 알 수 있었다. Zn_2SnO_4 의

유닛셀 내의 공간군과 전자상관교환에너지의 효과에 대해서도 연구하였다. 공간군의 변화는 열적 안정성에 영향을 주었다. 제일원리 계산법을 이용하여 얻은 열적 안정성 결과는 Zn_2SnO_4 , ZnO 과 SnO_2 의 혼합 상태의 실험 결과를 잘 반영하였다.

고온안정상인 삼성분계 화합물 Zn_2SnO_4 에서 산소 공공과 침입형 수소의 거동에 대해 연구하였다. 계산은 실험에서 보고된 것과 같은 밴드갭을 얻기 위해 HSE와 같은 하이브리드 밀도범함수를 사용하였다. 산소 공공 형성 에너지 계산 결과는 페르미 준위가 n-type 영역에 있을 때 전하가 없는 상태로 존재함을 보여준다. 전하가 변하는 레벨인 $\epsilon(2+/0)$ 는 전도대 아래 1 eV에 존재하였다. 산소 공공의 빛에 의한 이온화 에너지는 약 2 eV로 광전류 소스로 작용할 수 있음을 알 수 있었다. 침입형 산소는 전자를 만들어내며 H^+ 상태로 존재함을 알 수 있었다.

제일원리 분자동역학을 기반으로 하는 melt-quenching 방법을 통해 비정질 Zn_2SnO_4 와 $ZnSnO_3$ 을 얻었다. RDF 분석 방법을 통해 주석의 배위수가 산화주석의 값인 4에 가까워지는 결과를 얻었다. 그리고 주석-산소의 결합길이는 산화주석의 길이와 비슷하였다. 반면에, 배위수와 주석-산소 결합길이를 고려했을 때 주석-산소 결합 상태는 결정질 산화주석과 산화아연주석에서 모두 비슷하였다.

Keywords : *ab-initio*, zinc tin Oxide (ZTO), transparent conducting oxide (TCO), p-T phase diagram, point defect, amorphous

Student ID : 2007-20739

Joochi Lee